MODELLING AND CHARACTERISATION OF INDUSTRIAL BIFACIAL SOLAR CELLS FOR HIGH EFFICIENCY MODULES

Sng Guan Kian, Ernest

Submitted in fulfilment of the requirements for the
Degree of Doctor of Philosophy

School of Engineering
College of Science and Engineering
University of Glasgow

September 2023

Abstract

Bifacial photovoltaic modules absorb additional sunlight from the module rear, as well as the front, in comparison to the monofacial modules that only generate electricity from its front side. Therefore, bifacial modules result in higher energy conversion efficiency as it could potentially generate twice the energy per unit area when compared to the conventional monofacial modules. While the analysis of optical gains and power transfer of monofacial photovoltaic cells and module are relatively well-established, there are many nuanced effects that contribute to bifacial cells and modules performance. As such, these potentially high-performing bifacial cells do not easily translate to better module performance.

In this thesis, new results in the modelling, simulation and outdoor study of bifacial modules are presented. Firstly, a study on optical ray tracing for bifacial solar modules with reflective coating at the cell gap is presented for three different configurations. The simulation considered absorption losses with current gain from each configuration with varying cell gap designs. These bifacial modules with white reflective coating configurations were fabricated for indoor flash test under standard test conditions (STC) and outdoor monitoring energy yield to verify the simulation results. This is followed by the optimisation of the cell structure and material thickness under varying tilt conditions. Last but not the least, an investigation of ground reflected irradiance on the bifacial gain is conducted. It is demonstrated that the main contribution to bifacial module irradiance gain is from the ground reflected rays that were transmitted through the transparent cell gap of bifacial modules. Similarly, outdoor energy monitoring results are used to verify the simulation results from the fabricated modules.

From the simulations, indoor flash tests and outdoor energy yield monitoring, the proposed optimal module design for STC indoor front illumination flash test is Configuration 1 at 3.4% current gain. For front and rear illumination flash test, Configuration 2 gives the highest gain at 2.2%. For outdoor performance on a tracker, bifacial modules without reflective coating would give the best performance. For fixed installation, the highest performance is from Configuration 1 bifacial modules that are mounted at a 45° tilt. The above identification of the various optimal module design and their mounting condition are critical for efficient performance of bifacial modules in different applications, thereby improving bifacial module performance.

Contents

Publications

The research in this thesis has been published in international peer reviewed conferences. The list of publications is provided below.

1. E. Sng, C. X. Ang, and I. L. H. Lim, “Investigation and Analysis of Bifacial Photovoltaics Modules with Reflective Layer,” In: 35th European Photovoltaic Solar Energy Conference Exhibition (EUPVSEC 2018), Brussels, Belgium, 24-28 Sep 2018, pp. 1260–1264.

2. E. Sng, A. Sahadevan, S. Channabasappa Devihosur, S. Rohini, K. Malar, S. Roy, L.H.I. Lim, “Optimisation of Bifacial Photovoltics Module with Reflective Layer in Outdoor Performance,” In: 36th European PV Solar Energy Conference and Exhibition (EUPVSEC 2019), Marseille, France, 09-13 Sep 2019, pp. 1007-1011, doi: 10.4229/EUPVSEC20192019-4AV.1.12

3. Sng, G. K. E., Chua, S. W., Roy, S. and Lim, L. H. I., "Solar Energy Simulation of Bifacial Panels for Performance Optimisation," 47th IEEE Photovoltaic Specialists Conference (PVSC 47), Aug. 2020, doi: 10.1109/PVSC45281.2020.9300749

List of Tables

List of Figures

Acknowledgements

First, I would like to express my deepest gratitude to my academic supervisors Dr. Idris Lim Li Hong and Prof. Scott Roy for the opportunity to pursue the research works at the University of Glasgow. I would not be able to complete this dissertation without their generous patience and support throughout this program. Their numerous feedback and guidance have challenged me to be a better researcher. Second, I am deeply indebted to my past and current industrial supervisor Dr. Hannes Rostan and Dr. Kenta Nakayashiki for the opportunity to conduct my research together with my industrial work at REC Solar. Third, I am grateful for all my fellow University of Glasgow students in particular to Dr. Lai Meng and Dr. Jing Zhong and my colleagues at REC solar for their helping hand across this journey. Last, to my parents, my wife Ruth, and my daughter Natalie for their care and love in this journey.

Declaration

University of Glasgow

Statement of Originality to Accompany Thesis Submission

Name: Ernest Sng Guan Kian

Registration Number: XXXXXXXX

I certify that the thesis presented here for examination for a PhD degree of the University of Glasgow is solely my own work other than where I have clearly indicated that it is the work of others (in which case the extent of any work carried out jointly by me and anyother person is clearly identified in it) and that the thesis has not been edited by a third party beyond what is permitted by the University's PGR Code of Practice.

I declare that the thesis does not include work forming part of a thesis presented successfully for another degree [unless explicitly identified and as noted below].

I declare that this thesis has been produced in accordance with the University of Glasgow's Code of Good Practice in Research.

I acknowledge that if any issues are raised regarding good research practice based on review of the thesis, the examination may be postponed pending the outcome of any investigation of the issues.

Signature: .....

Date: .....

Acronyms

PV	Photovoltaic
LCOE	Levelised cost of electricity
STC	Standard testing conditions
EVA	Ethylene-vinyl acetate
BSF	Back surface field
Al-BSF	Aluminium back surface field
PERC	Passivated emitter and rear contact
PERT	Passivated emitter and rear totally diffused
AM1.5G	Air mass 1.5 Global
SDE	Saw Damage Etch
$POCl_3$	Phosphorus oxychloride gas
PECVD	Plasma enhanced chemical vapour deposition
MPP	Maximum power point
V_{oc}	Open circuit voltage
I_{sc}	Short circuit current
V_{mpp}	Voltage at maximum power point
I_{mpp}	Current at maximum power point
FF	Fill factor
R	Reflectivity
h	Mounting height
RMSE	Root mean square error
WAR	Weight average reflectance
Sn	normalised reflected radiant intensity
IQE	Internal quantum efficiency
EQE	External quantum efficiency
C1	Configuration 1
C2	Configuration 2
C3	Configuration 3
Wh	Watt hour
Wp	Watt peak

Chapter 1

Introduction

1.1 Background

Energy demand has always increased in tandem with the progression of mankind since the first industrial revolution. From the mechanisation of manufacturing with steam and hydro energy to mass production in assembly lines with automation and the advent of "smart factories" that uses the cyber-physical system, electrical energy is required. Exponential industrialisation of developing countries and global population growth have resulted in a surge in energy demand. While fossil fuels have been the cheapest source of energy, it is non-renewable and finite. Fossil fuels such as coal, oil, and natural gas require the decomposition of organic material under the earth's crust, which takes place over millions of years. This increase in demand for energy not only depletes the finite fuel source. Its combustion emits greenhouse gases, such as carbon dioxide into the atmosphere, which in turn heats up the earth. The increase in the earth's temperature causes climate change that changes precipitation patterns causing floods and droughts, weather abnormality, and the rise in sea level. This dangerous change in the earth's temperature resulted in 195 countries acting together in 2015 to adopt the Paris Agreement. This agreement targets to limit the rise of earth's temperature to below 2°C above pre-industrial levels. It calls for the local authorities to address climate change to reduce greenhouse gas emissions. This agreement results in renewable energy sources being progressively adopted to replace conventional sources, in providing sustainable and clean energy to sustain the development of the world [1].

Renewable energy sources such as solar photovoltaic (PV) and wind or low-carbon sources such as nuclear, hydropower, and geothermal could provide the growing human population with clean energy. Solar energy from the sun is ubiquitous and also a dependable source of energy, which is in abundance. Solar energy sources are not geologically limited like wind, geothermal, or hydro power and could be situated close to the demand, therefore reducing the transmission losses [2]. It could be situated off the main electricity grid where it could supply electricity to remote locations and in space for satellites. Levelised cost of electricity (LCOE) is often used

to evaluate the cost competitiveness of the energy source where the output is compared to the cost of generation across the lifetime of the energy generation system [3]. LCOE of solar is predicted to drop to below coal or gas level in 2030, as shown in Figure 1.1. The reduced solar energy LCOE is now competitive with fossil fuels. This reduction in cost increases the installation capacity, which leads to further reduction through economy of scale. Solar energy is on track to be the most used renewable energy source by 2030 with this downward trend. The field of solar power generation options is commonly categorised into utility PV, commercial PV, and residential PV as shown in Figure 1.1. Utility PV are large-scale installation by energy companies for the sales of electricity generated, thus profit is the main consideration. Sun trackers are commonly used to continuously adjust the modules' tilt-angle to face the sun across the day. Commercial and residential PV are end-users that are looking to augment grid supply electricity with medium to small-scale fixed position installation on their roofs. Efficiency and aesthetic are their main consideration due to their scale.

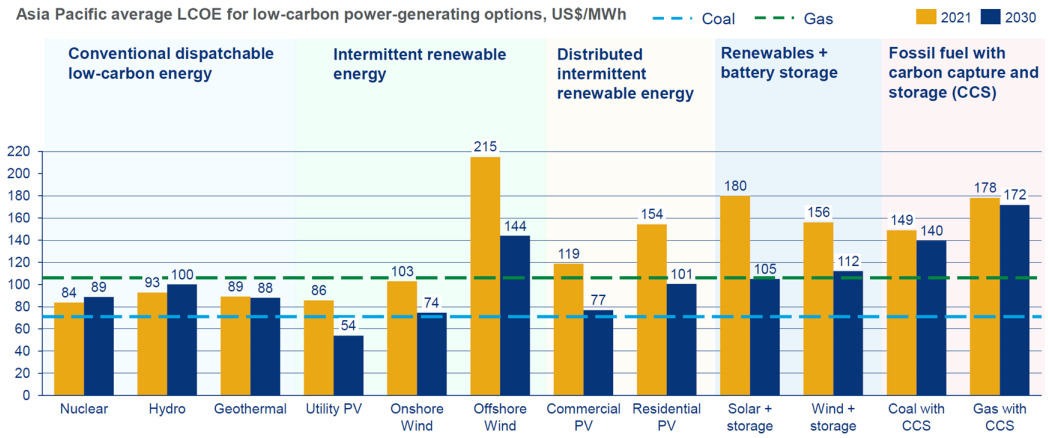

Figure 1.1: LCOE of low carbon energy sources in 2021 with the prediction of utility photovoltaic being the lowest in 2023 [3]

Solar energy generates electricity via the photovoltaic effect, where the solar irradiance from the sun is converted into electricity with the p-n junction in the semiconductor material of the solar cell. For terrestrial applications, the solar module (solar panel) which comprises several solar cells connected in an array, is generally used as it protects the solar cell from weather and mechanical damage. The majority of commercially available solar cells are based on crystalline silicon with cells connected in series and parallel for matching of desired voltage and current. The common solar module, as shown in Figure 1.2, consists of multiple silicon solar cells interconnected in series connection with small gaps between them to reduce breakages when laminated with encapsulant in between glass and backsheet with an aluminium frame giving its mechanical strength. Like the solar irradiance incoming from the sun which is one-directional, solar modules conventionally could only absorb irradiance from one single side of the module. To achieve lower LCOE, researchers have been improving the efficiency and reducing the asso-

ciated cost of manufacturing and installing solar modules [4].

Figure 1.2: Top view of a solar module with the white area between the cells as cell gaps

The research and development in photovoltaic technology has increased tremendously since the invention of the first practical solar cell in Bell Laboratories with an efficiency of 6% in 1954. While the efficiency of gallium arsenide-based solar modules for space applications has reached 46%, the maximum efficiency of commercially available crystalline silicon-based terrestrial solar modules is at 22.2%. This gap in efficiency is due to the difference in cost in space and terrestrial applications as the cost expectation for consumer commodity products is lower. While the benefits of renewable energy sources have historically been intangible, more tangible benefits could now be achieved as energy markets in various parts of the earth are gradually seeing lower LCOE on solar energy, as compared to fossil fuel.

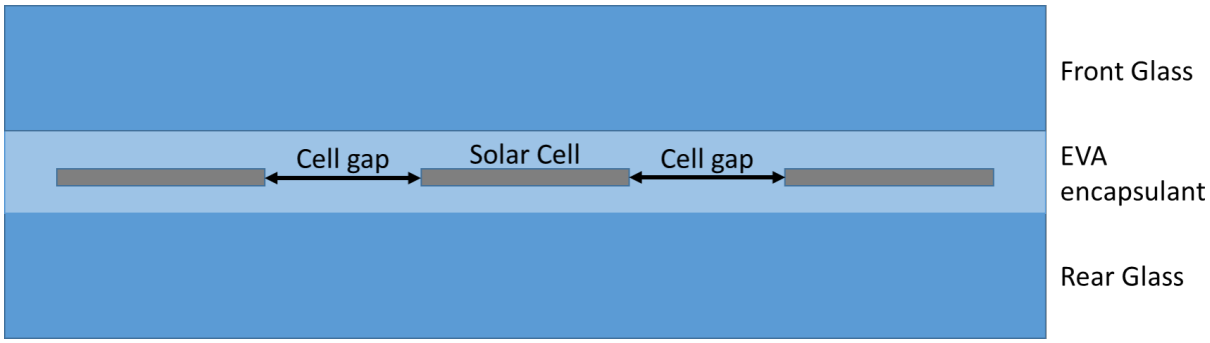

Figure 1.3: Cross-section of a bifacial solar module with cell gaps indicated between the solar cell in the module

Conventionally, solar modules absorb irradiance to generate electricity from a single side that is facing the sun. However, bifacial solar modules could absorb additional irradiance from the rear of the module. Bifacial module results in higher energy conversion efficiency as it could generate twice the energy per unit area, as compared to conventional modules. For irradiance

to be absorbed from the rear, the cell needs to be translucent, which increases the transmission losses from front irradiance. This inherent design resulted in lower cell efficiency of bifacial solar cells, as compared to monofacial cells with aluminium at the rear, under standard testing conditions (STC) that were used in the industry to evaluate single-side illumination efficiency. This is due to incoming illumination that is not being absorbed by the cell, which becomes a transmission loss through the cell gaps, as shown in Figure 1.3 . Nevertheless, advancements in materials with enhanced cell processing in the past few years have led to bifacial cells' front conversion efficiency overtaking that of the monofacial cell. This increased the interest in industrialising bifacial cells, in place of monofacial cells [5].

The bifacial design is progressively adopted due to the increase in cell efficiency outweighing the manufacturing cost from the advanced materials and enhanced processing. The implementation of bifacial design increased cell efficiency via the reduction of the rear surface recombination and aluminium absorption. Additionally, the reduction in rear aluminium paste consumption and the yield increase of module manufacturing from the reduction of cell bowing in turn, reduces the total manufacturing cost for bifacial cells. By generating more power at a lower cost, bifacial design enables solar energy to be more attractive to consumers. However, module efficiency trends show a conflicting picture where potentially high-efficiency bifacial cells do not easily produce high module power nor result in significant additional energy yield [6]. This apparent bonus power gain is not widely capitalized as bifacial module energy yield has its complications with different cell structures requiring a specific optimal module design, in addition to non-existent industrial standards needed for front and rear side illumination testing of bifacial modules.

1.2 Motivation

This thesis presents the modelling, simulation, and outdoor study of high-efficiency bifacial solar modules. The motivation of this thesis is listed as follows.

A. Investigation of current gain in bifacial solar modules with reflective inter-cell gap

With the steadily increased cell conversion efficiency of commercial bifacial solar cells, more awareness was raised for bifacial standard testing conditions to correlate to the actual energy yield of the bifacial module. Although the current standard testing condition correlation between standard test conditions and energy yield for bifacial modules is not as mature as those for monofacial modules, the benefits of bifaciality have increased the research and development in this field. Furthermore, the power gain from the rear irradiance and reflective layer at the inter-cell gap have been proposed to improve module internal reflectance for both monofacial and bifacial modules [7]. To the best of our knowledge, an accurate model for bifacial modules has yet to be established.

Recent developments of bifacial modules with a reflective layer inserted between the cell increase the module front side current without totally removing the bifacial capability of the module [7] [8]. In this structure, various configurations of varying locations of the reflective surface were proposed. Although the influence of the cell gap on monofacial cells in monofacial modules was widely reported, strategic placement of the reflective surface affects the bifacial cell module performance during STC and outdoor monitoring. Hence, it is critical to develop a numerical model for different configurations of the bifacial cell for a parametric study on the varying inter-cell gap with a reflective layer. In order to reflect the performance of the bifacial module under outdoor conditions, three different illumination conditions should be considered namely the front illumination, rear illumination, and illumination from both sides.

B. Simulation and material optimisation analysis for bifacial modules with variable tilt

In Singapore, there are only approximately 670MWp of photovoltaic installation today, with the target to reach 2GWp of photovoltaic installation by the year 2030 [9]. In land-scarce Singapore bifacial photovoltaic modules could be the economical solution to hasten the installation volume. While the monofacial modules in Singapore are commonly mounted at 10 degrees South facing, bifacial modules could be mounted in a similar setup or 90-degree East-West facing [10]. The additional factor of ground reflected rays and elevation complicates the energy yield optimisation, as compared to conventional monofacial modules. A performance gain of 10% was reported for bifacial modules installed in Singapore on a roof with less than 20% reflectivity [11]. A simulation of bifacial modules in Singapore illustrates additional bifacial energy gain with higher ground albedo [12] as the increase of module elevation height reduces self-shading and improves rear illumination inhomogeneity [13].

With the recent developments of modules with a reflective layer, different approaches in mounting optimisation for different configurations have emerged, as compared to the Type 0 normal glass/glass bifacial module. The varying location of the reflective layer results in the differing ray path from the reflected irradiance in the module internally. A Type 1 module was reported previously with the highest current gain for STC front side flash at 3.4%. With 1 sun on both the front and rear illumination, the current gain for Type 1 was reduced to 1.7% [14]. In an outdoor setting, the illumination for both front and rear would unlikely be 1 sun simultaneously for both front and rear. Hence, a ray tracing model would be required to incorporate the reflected ground and global irradiance in an outdoor performance test with different tilt angles to study the optimal module configuration and mounting arrangement.

C. Investigation of the effect of ground irradiance on varying bifacial module configurations

Modelling and simulation can be used to analyze the performance of the module before indoor and outdoor testing. The front surface of the bifacial module is commonly simulated in the same way as the front surface of monofacial module. Reported works from other researchers on the front irradiance of bifacial modules using Ray Tracing has proven to be accurate with different inter-cell gaps. It is shown to be capable of computing the additional contribution of rays that are being reflected back to the cell by a reflective layer at different positions of the module [8]. These works presented accurate models for simulating different designs of the bifacial modules but without any tilt and ground effects.

Other methods for modelling and simulation include the ray tracing method and the view factor method. Ray Tracing is a technique that can trace the path of light and accurately simulate the way light bounces off an object. The View Factor method is used to create a 2D model to simulate the front and rear irradiance of the bifacial module while taking into consideration the reflections from its surroundings in [15]. The presented model has been verified to produce a similar trend to the measured data and predict accurate results only at specific times. This experiment only tested the modules in 0° and 30° at a fixed height, which does not provide the relationship between different configurations and the gain produced. Compared to View Factor, Ray Tracing is much harder to use and implement due to the amount of effort required but can simulate results that View Factor cannot. It is mostly used when geometry is irregular and can produce accurate results whereas View Factor becomes complex to use when dealing with irregular geometry. Although Ray Tracing is more accurate when compared to View Factor, it is very resource-demanding and would require a lot of time and effort to produce results for large-scale simulation. In addition, Ray Tracing can also be used to find the efficiency of the design of the module [16].

Similar works have also been done by other researchers to predict the gain at both sides of the module at different rows by using View Factor and Ray Tracing. A 3x3 PV system was tested at different tilt angles and heights separately. The different configurations were then simulated by three different models. The work showed that increasing the height of the module would yield a higher gain until a saturation point where the gain will no longer increase despite increasing the height of the module. An accurate prediction of rear gains up to 45° was also obtainable through the model [15]. Other related work has been performed by a group of researchers to calculate the rear irradiance of bifacial modules [17]. The rear irradiance was modelled using cell level View Factor and Ray Tracing at a fixed tilt angle. The results generated from the models were proven to follow the trend of the measured short-circuit current very well. It is concluded that Ray Tracing is more suitable for detailed areas, like module design and optimization, while View Factor is more suitable for simulating array performance. In [18], only cell level View Factor is used to model the rear irradiance of the module at the same configuration as the simulation results obtained by the model are shown to differ by roughly ±10% when compared to the measured irradiance. So far, there is relatively little work done with Ray Tracing on the rear side of the bifacial module, with respect to different tilt angles and heights for performance optimization [19]. Hence, a bifacial module ray tracing model not only needs to take into account the internal ray path but also incorporate the interaction between the different module designs and mounting configurations to the resulting ground-reflected rays and those rays that are reflected back into the module.

1.3 Aims and Objectives

The objectives of this thesis are to contribute to the modelling and characterisation of high-efficiency bifacial modules for industrial bifacial solar cells in the following aspects:

1. To develop a ray tracing model for the bifacial solar module with a white reflective coating at the cell gaps for investigation of current gain, the design merits, and contributions from the reflective coating.

2. To conduct a parametric study on the varying inter-cell gap with a reflective layer and propose the optimal design for STC and bifacial illumination indoor flash test performance.

3. To optimise the proposed ray tracing model for outdoor performance, taking into account the module mounting configuration and the optimal module material for a proposed design.

4. To conduct outdoor energy yield verification for the proposed module design to validate the ray tracing model for the bifacial solar module with a white reflective coating at the cell gaps.

5. To improve bifacial module simulation models for outdoor energy yield scenarios taking into account the different interactions between module design and mounting configuration, due to the ground-reflected rays.

6. To determine the optimal module design for a bifacial solar module with a white reflective coating at the cell gaps for indoor flash test and outdoor energy yield performance.

1.4 Contributions

In this thesis, new results in the modelling, simulation, and outdoor study of bifacial modules are presented. A study on optical ray tracing for three different configurations of bifacial solar cells is presented. The current gain for bifacial solar panels is determined in simulation and verified through indoor flash tests under standard test conditions. This is followed by the optimisation of the cell structure and material thickness under varying tilt conditions. The results are verified similarly through indoor flash tests. Last but not least, an investigation of ground-related irradiance on the bifacial gain is conducted. Outdoor energy monitoring results are used to verify the simulation results. Detailed contributions in each of these areas are given as follows.

- Three new bifacial module configurations with reflective layer coated at different positions are proposed and studied in detail; namely, Configuration 1: Glass / EVA / Bifacial Solar Cell / EVA / Glass / Reflective Layer, Configuration 2: Glass / EVA / Bifacial Solar Cell

/ EVA / Reflective Layer / Glass, and Configuration 3: Glass / EVA / Reflective Layer / Bifacial Solar Cell / EVA / Glass designs. To the best of our knowledge, these additional designs for bifacial modules with white reflective coating have not been reported in any existing literature.

- An optical ray trace model for each of the three configurations was created with inputs from test measurements. The simulation of the three configurations considered the absorption loss in the simulation of the current gain from each configuration with varying inter-cell gap distances. The corresponding performance gain was evaluated for models with and without absorption loss. The simulations demonstrated that illumination conditions would change the optimal reflective coating design. Configuration 1 has the highest current gain of 3.4% with front-side illumination. But with rear illumination, Configuration 1 has no additional gain as the reflective layer reflects the rays out of the module. Hence, the highest current gain changes from Configuration 1 of 1.7% gain to Configuration 2 of 2.2% gain with Configuration 3 at 1.8% current gain. These findings reported in Chapter 3 together with the published results from other researchers pushed the industrial bifacial modules to incorporate white reflective coating for STC performance gain.

- Material optimisation analysis with the identification of an optimal tilt for Type 1 bifacial module configuration. A range of varying tilt angles was simulated to identify the optimal material thickness and tilt for maximum current gain bifacial modules with a white reflective coating at the cell gap. A tilt angle of 45° was proposed and validated to be beneficial for modules with white coating due to the additional rays being captured and reduced self-shading.

- Monofacial and bifacial modules with different white reflective coating configurations were fabricated for indoor flash tests and outdoor monitoring energy yield. Reported gains of 2% to 3% current gain were measured for bifacial modules with the different white reflective coating configurations to further validate the findings from the simulation model for STC performance. Performance gain during the indoor STC flash test from reflective layer coating in the cell gap of bifacial did not result in better outdoor performance during our outdoor energy yield monitoring. These conflicting results reported in Chapter 4 substantiated the conflicting acceptance of bifacial module designs between the utilities and residential PV markets due to their differing needs.

- The effect of ground-reflected irradiance on three different types of bifacial module configurations: (i) Monofacial, (ii) Bifacial, and (iii) Bifacial with white reflective coating were modelled with ray tracing. The main contribution to bifacial module irradiance gain is from the ground reflected rays that were transmitted through the transparent inter-cell gap of bifacial modules, which is absent in bifacial modules with a white reflective coat-

ing. These reflected ray's contribution also decreased with the increase of module tilt-angle due to the decrease in the active area that is directly facing the ground. These results reported in Chapter 5 contribute to the study of optimal mounting conditions for bifacial modules.

- The optimal modules design proposed for STC indoor front illumination flash test is Configuration 1: Glass / EVA / Bifacial Solar Cell / EVA / Glass / Reflective Layer giving a 3.4% gain. For indoor front and rear illumination flash test, Configuration 2: Glass / EVA / Bifacial Solar Cell / EVA / Reflective Layer / Glass gives a 2.2% gain. For outdoor performance on a tracker that keeps the module at 0° to the sun at all times, a bifacial module without a white reflective layer would give the highest gain for utility PV application. For a fixed installation in commercial and residential PV, the optimal module would be Configuration 1: Glass / EVA / Bifacial Solar Cell / EVA / Glass / Reflective Layer at a 45° tilt. The above identification of the optimal modules and their mounting conditions for various applications contributes towards a further reduction of LCOE for solar energy.

1.5 Organisation of Thesis

This thesis is organised as follows. Chapter 1 gives a brief introduction to our proposed methods for the modelling, simulation, and test of bifacial modules. This is followed by an overview of the solar photovoltaic device structure, bifacial cells, indoor measurement tests, module performance, and outdoor energy yield calculations in Chapter 2. Chapter 3 presents an investigation and analysis of current gain in bifacial solar modules with reflective inter-cell gaps. This is followed by the simulation and material optimisation analysis for bifacial modules with variable tilt in Chapter 4. In Chapter 5, an investigation of the effect of ground irradiance on bifacial modules of varying configurations is presented. Lastly, Chapter 6 provides a brief summary and discussion to conclude the thesis, and to discuss the future directions of our research.

Chapter 2

Literature Review

In this chapter, the solar cell structure of monofacial and bifacial cells is briefly introduced. This is followed by a review of the indoor measurement test for cells and modules. Subsequently, the optical ray tracing simulation for calculating the module performance is discussed. Lastly, the outdoor energy yield calculation of bifacial modules is presented.

2.1 Solar Photovoltaic Device Structure

Following the first practical photovoltaic cell that was invented in 1954, the first bifacial cell with an efficiency of 7% was introduced at the 1977 European Photovoltaic Solar Energy Conference and Exhibition. The bifacial cell structures were divided between the double junction and the single junction with a back surface field (BSF). Double junction bifacial solar cell with p+ n p+ or n+ p n+ structure was first proposed in a more transistor-like structure [20]. In this structure, the front and rear junctions would absorb the short and long-wavelength photons respectively. In 1970, a single junction with a back-surface field of p+ n n+ was proposed [21]. Solar cells from then on are mainly single-junction with a back-surface field (BSF) as the back surface field reduces surface recombination, which results in the increase of open circuit voltage. The common industrial solar cell is of an aluminium back surface field (Al-BSF) structure, where the silicon is p-type based with an n-doped emitter and a p+ back surface from with a layer of aluminium that is opaque to light. The n-type based with a p+ emitter is used in niche areas where high efficiency is required.

The main difference between a bifacial cell and monofacial cell is the ability to absorb solar irradiance from the rear of the cell. As illustrated in Figure 2.1, this bifacial ability is a result of changing the rear layer from aluminium metal to a translucent film, such as aluminium oxide or silicon nitride with grid metal, to allow photons to be absorbed from the rear irradiance. On the cell level due to the translucent film, there is a reduction of internal reflectance as photons

are transmitted out of bifacial cells, resulting in a reduction of cell current as compared to a monofacial cell. Similarly, the transmitted photons are lost on bifacial modules during indoor standard test condition (STC) flash tests. However, for outdoor performance, the bifacial module could absorb the ground reflectance from transmitted photons and surrounding irradiance. As a result, the performance evaluation from the standard test conditions of bifacial modules could not be correlated to its outdoor energy yield performance using conventional solar energy yield models.

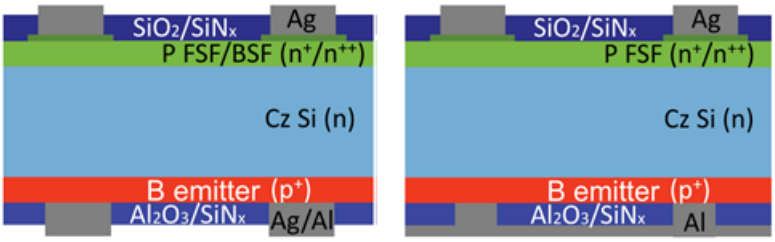

Figure 2.1: Cross-section of bifacial (left) monofacial (right) solar cell with exposed rear side that are not covered by aluminium (Al) which allows absorption of light [22]

2.2 Bifacial Cells and Modules

For the production of a bifacial module, bifacial cells are employed to enable the absorption of sunlight from both sides. In this section, the fabrication of two bifacial silicon photovoltaic cell structures of p-type Passivated Emitter and Rear Contact(PERC) and n-type Passivated Emitter and Rear Totally Diffused(PERT) and their module fabrication will be discussed.

2.2.1 Absorption of Sunlight And Photovoltaic Effect

Conventionally, solar cells absorb sunlight to generate electricity from the side that is facing the sun. For solar energy to be a competitive energy source, generation costs must be lowered either via means of low-cost manufacturing or improvements in energy conversion efficiency. One of the means to improve sunlight conversion efficiency is the use of a bifacial cell, where conversion efficiency is improved through absorbing more sunlight per unit area.

The simplified sequence of generating electricity in the solar cells first starts with photons from the sunlight that are not reflected from the front surface. These photons are absorbed in the silicon bulk and generate electron-hole pairs. Next, the generated electron holes pairs photocurrent is then collected at the p-n junction, which is commonly formed via doping of phosphorous or boron dopant for either excess electrons or holes of missing electrons in the silicon. Figure 2.2 shows the absorption coefficient of sunlight in silicon plotted, together with the AM1.5G solar spectrum [23]. Most of the high photon energy short-wavelength light is

absorbed in the front surface. With increasing wavelength, the photon energy reduces. When the photon energy is less than the silicon band gap, the absorption coefficient reaches zero.

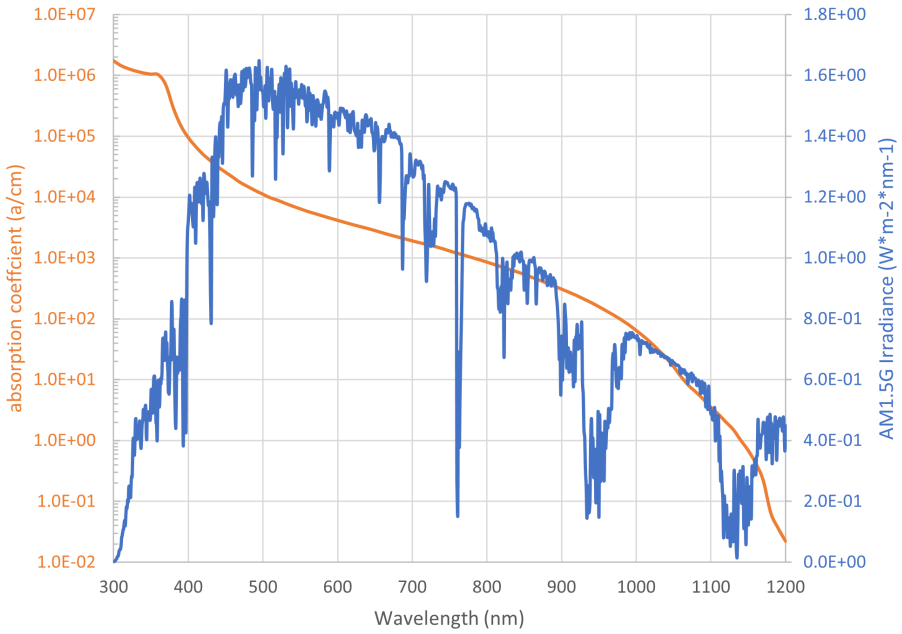

Figure 2.2: Absorption coefficient of silicon (orange) with AM1.5G solar spectrum (blue) [23]

For the generated photocurrent to contribute to the light-generated current of the cell, it would have to travel to the p-n junction to be collected. The probability of contribution to the cell current reduces with the increase in surface recombination or short diffusion length, which is influenced by the silicon bulk quality. Surface passivation has the most impact as most of the photocurrent is generated on the front surface of the cell. From the simulation of the optimal thickness of solar cells that were previously reported, the optimal thickness of a solar cell is around 35um to 75um with the p-n junction near the surface for the highest collection probability [24]. In order to improve the collection probability via reducing recombination, a gradient back surface electric field is formed via increasing the doping concentration at the rear surface [25].

In a solar cell, the majority of the sunlight is absorbed in the front few micrometers in the silicon, which generates photocurrent that is collected in the front emitter causing a voltage difference over the cell. Two critical properties are needed for a cell to be bifacial. First, the rear surface of the solar cell needs to allow absorption of sunlight. Second, the photocurrent generated in the rear must travel across the silicon base to the front emitter for collection and not recombined in the rear surface or in the silicon bulk. As discussed, the spectrum response of the solar cell at different wavelengths could show the quality of the cross-section via its remaining collection probability by the percentage of current extracted by the cell. Figure 2.3 shows the reported measurement of the internal quantum efficiency (IQE) spectrum of a bifacial solar cell

where the blue plot shows the highest collection at the p-n junction with recombination losses at the front and rear surface from front illumination. For the rear illumination, which is plotted in orange, the collection probability increases with longer wavelengths.

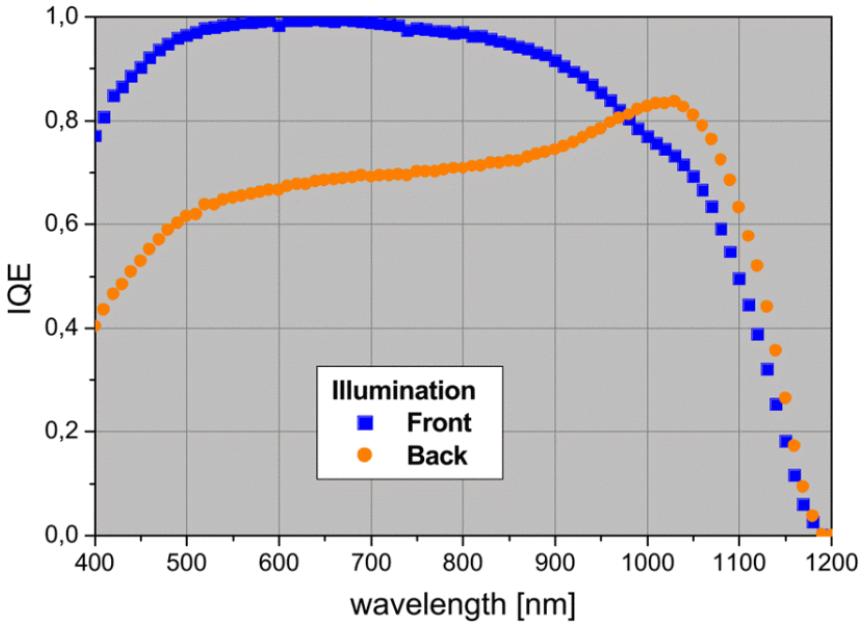

Figure 2.3: Measured spectral response of bifacial cell with front (blue) and rear (orange) illumination [26]

2.2.2 Solar Cells And Modules Design Process

Conventional industrial photovoltaic cells are commonly manufactured with five processing steps, starting with Saw Damage Removal (SDE) and chemical-based surface texturing [27] The former removes the physical surface and sub-surface damages introduced to the wafer during the wafer sawing process [28], and the latter modify the planer surface for reduction in reflectance and light trapping [29]. This is followed by the n-type emitter formation through high-temperature diffusion with phosphorus oxychloride (POCl3) gas [30].

For a high-quality p-n junction, the emitter has to be isolated from the bulk via chemical etching. The emitter is then passivated with amorphous silicon nitrite deposited via Plasma Enhanced Chemical Vapour Deposition (PECVD) [31]. Current collection and BSF formation are processed with screen printing of silver grid lines on the emitter surface and the full area aluminium thick paste deposition. The final steps are the activation of hydrogen radicals in the silicon nitride layers for the emitter and bulk passivation, the sintering of silver grid to contact the emitter, and the alloying aluminium and silicon for BSF formation [32] [33]. Figure 2.4 illustrates the cross-section schematic of the completed BSF cell. The diffused n-type emitter is highlighted in red with the full area Al-BSF in green.

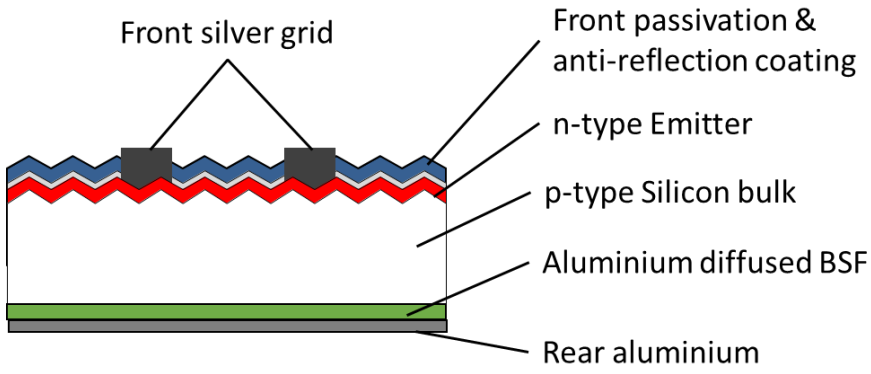

Figure 2.4: Aluminium back surface field cell with the various processed layers with full rear aluminium resulting in it being not bifacial

As reported in the simulation done by Chen et.al., a highly optimised Al-BSF photovoltaic cell from mass production manufacturing could only achieve a maximum of 19% conversion efficiency due to the limitation of recombination at the silicon-aluminium interface [34]. An enhancement in the rear surface recombination at the silicon-aluminium interface and the internal reflectance of the rear side of the cell will require two additional processing sequences on the BSF, passivated emitter, and rear contact of the photovoltaic cell [35] [36].

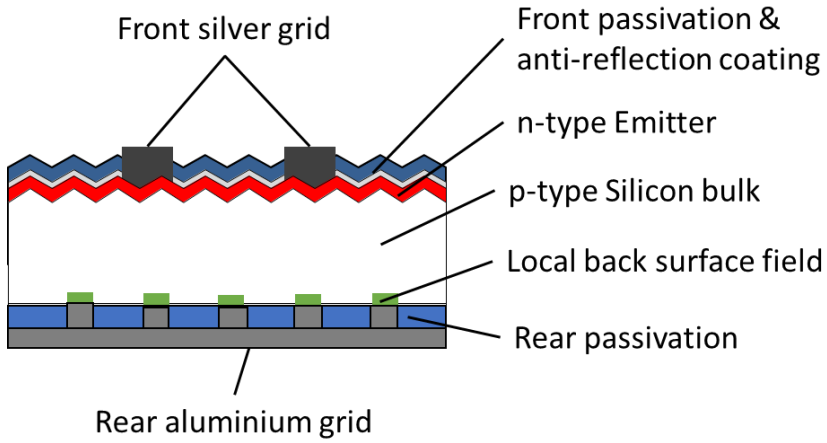

Figure 2.5: p-PERC monofacial cell with the various processed layers with full rear aluminium resulting in it being not bifacial

Figure 2.5 shows the PERC photovoltaic cell while Figure 2.6 shows the PERT photovoltaic cell where screen-printed aluminium at the rear that are directly in contact with the silicon surface are replaced with PECVD deposited passivation layers [37] [38] [39]. Localised contact opening of the rear passivation via laser ablation creates the pathway for localised BSF formation and electrical contacts for current collection [40] [41]. This upgrade improves the conver-

sion efficiency of the cells from around 18% for BSF cells to 21% of PERC cells. The PERC's full coverage of aluminium on the rear is an integral part of the metallisation design in reducing resistivity losses. Rear metallisation is compromised to convert conventional PERC to bifacial PERC in Figure 2.7. The conversion to bifacial comes with an increase in series resistance losses due to the compromise made between rear metallisation and the creation of bifacial PERC. To further increase bifacial PERC bifaciality towards 100%, the aluminium shaded area would have to be like its front silver grid. This forms a paradoxical situation for PERC where the improvement to bifaciality causes an increase in series resistance, which reduces the STC measured efficiency. This compromise results in a lower bifaciality of PERC cells in the market, as compared to PERT.

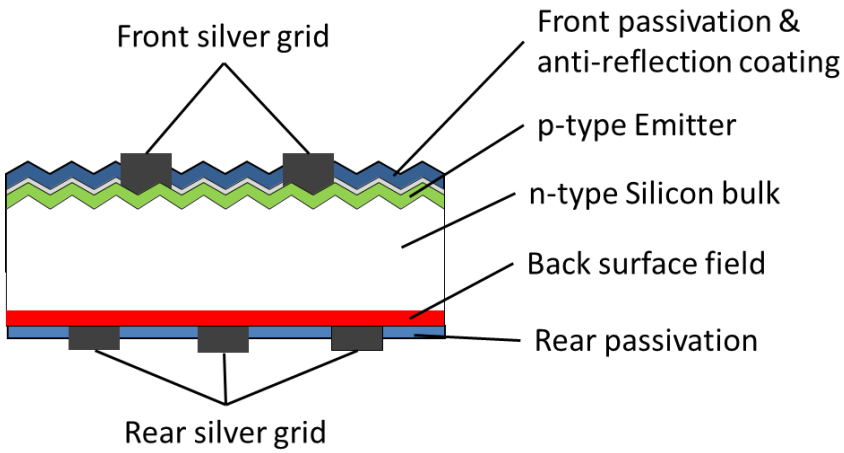

Figure 2.6: n-PERT cell structure with the various processed layers with rear sliver grid resulting it being bifacial

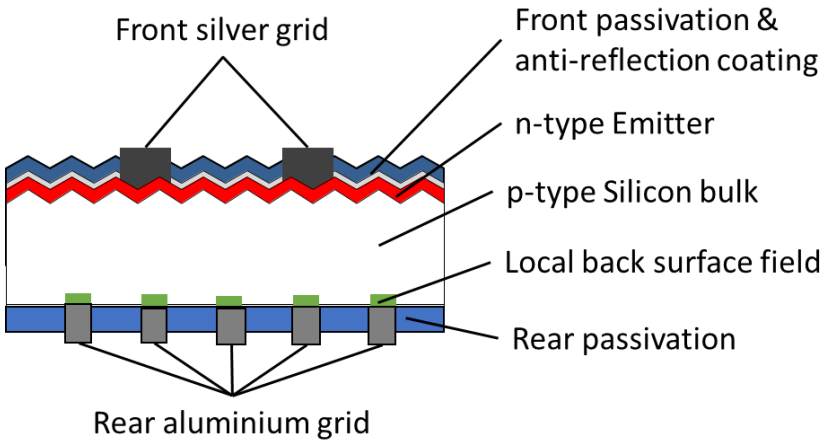

Figure 2.7: p-PERC bifacial cell structure with the various processed layers with rear aluminium grid resulting it being bifacial

Due to the limitation of both p-type multi-crystalline and p-type monocrystalline silicon

wafer quality and sensitivity to metal contamination during processing, high conversion efficiency solar cells are typically made of n-type bulk material in the following sequence [42]. Firstly, the wafer surface is treated to remove saw damage and alkaline textured to form random pyramids for light trapping [43]. Secondly, the p-type emitter is formed with high-temperature boron diffusion, and subsequent homogeneous phosphorus doping was done to form the totally diffused back surface field [44] [45] [46]. Thirdly, an anti-reflective coating consisting of silicon nitride is deposited on both sides before laser edge isolation. Lastly, cell processing of screen printing of precursors and contact formation of metal grid and is completed. While the Al-BSF and p-PERC cell structure in Figures 2.4 and 2.5 are monofacial, the n-PERT and p-PERC bifacial cells in Figure 2.6 and 2.7 are inherently bifacial due to the non-metallised rear surface. The design of solar cells contributes to the difference in performance of the solar modules, which is the next step of the process.

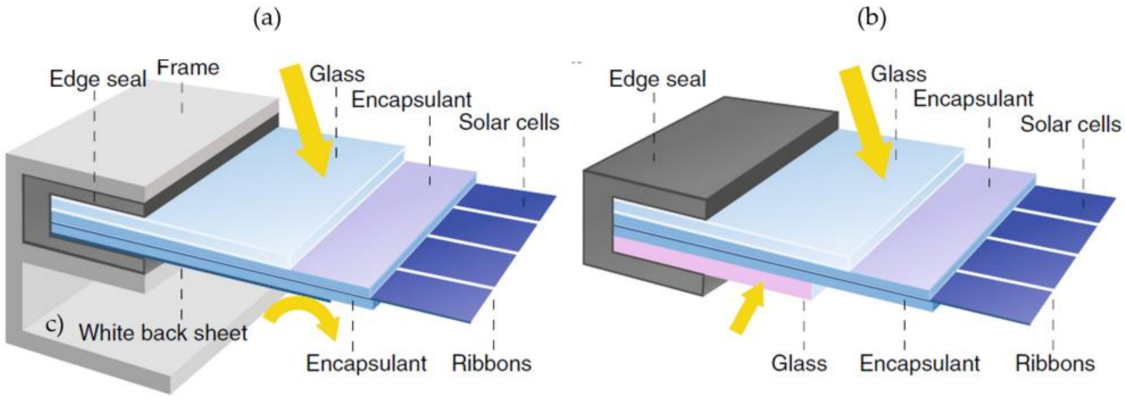

Figure 2.8: Cross-Section of solar module edge most cell (a) monofacial with a solar cell in between the front glass and rear white backsheet, (b) bifacial with a solar cell in between front and rear glass [5]

A bifacial module consists of typically around 60 to 72 pieces of bifacial solar cells, which are interconnected together in series or parallel to the desired module voltage before being sandwiched between encapsulates and laminated between two glass with their cross-section, as shown in Figure 2.8. The bifacial solar module is mostly identical to a monofacial solar module as the only difference is in the replacement of the white backsheet with glass to allow the transmission of light from the rear of the module to reach the solar cell. The bifacial module design resulted in an increase of the module current thus, resulting in the additional cell-to-cell interconnection needed to reduce the restive load of the module, so as to fully harvest the additional irradiance [5]. However, unlike the monofacial module in which the optical design had been optimised by researchers for years, the bifacial module requires additional work on the module design to improve its performance in the reduction of optical transmittance losses through the cell gap, front, and rear glass thickness optimisation, so as to improve the module's internal optical coupling and the cell-to-cell gap distance when a reflective coating is applied, as

shown in Figure 2.9 [47].

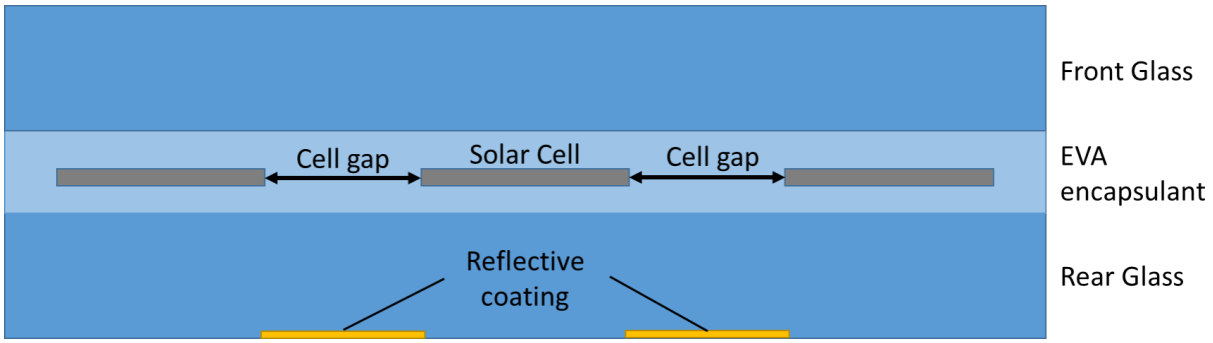

Figure 2.9: Cross-Section of bifacial solar module with solar cell in between front and rear glass and with reflective coating being coated at the rear of rear glass between the cell gaps

2.3 Indoor Measurements Tests For Bifacial Cell And Module

In this section, an introduction to the indoor measurement tests for the bifacial cell and the bifacial module is provided.

2.3.1 Bifacial Cell Measurement Test

The performance evaluation of terrestrial solar cells and modules is typically defined by its current-voltage characteristics under standard test conditions, where the illumination of AM1.5G spectrum with 1000 W/m^2 is used and the device under test is kept at 25°C, as shown in Figure 2.10.

During illumination, the current generated for the corresponding forward-biased voltage sweep is measured. This forms the current-voltage ($I-V$) curve that define the maximum power point (MPP), open circuit voltage (V_{oc}), short circuit current (I_{sc}), voltage at maximum power point (V_{MPP}), current at maximum power point ($_{IMPP}$) and fill factor (FF). For comparison across different shapes and sizes, the maximum power point is normalized with the input power from the incident light, which is the cell or module efficiency (n). The current-voltage curve is described by Shockley's diode equation with deformation to the curve by shunt resistance and series resistance. The fill factor is the ratio that describes the shift of the maximum power point from the product of its open circuit voltage and short circuit current because of the two resistances.

To keep the solar cell at the prescribed constant 25°C, it is placed on a conductive temperature-controlled gold-plated stage, which reflects photons that were transmitted out of the cell back

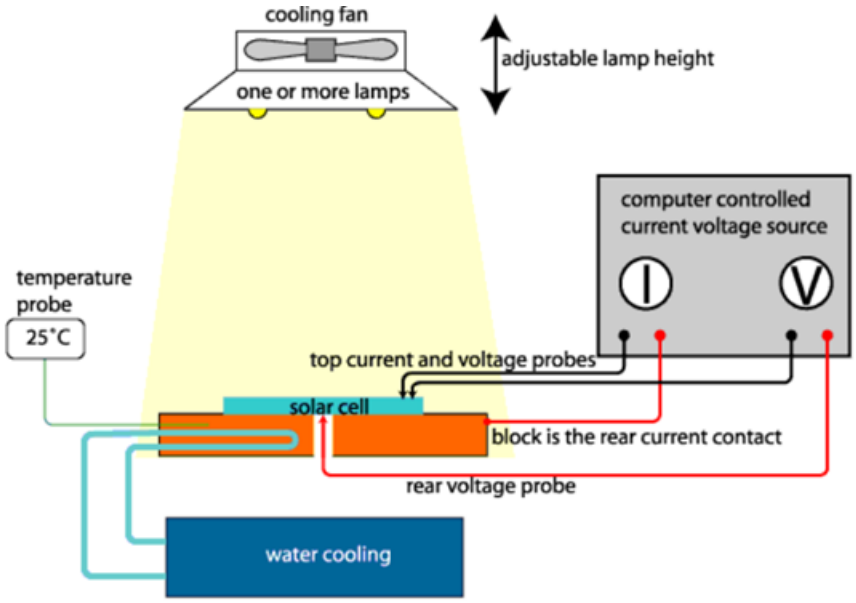

Figure 2.10: Basic structure of a simple IV tester with the solar cell under a single side illumination with voltage source applying a biased voltage and measuring the corresponding current [48]

into the cell. Duran et al. reported that there could be an additional 1% current gain from the reflective stage [49]. The reported gains were obtained using reflective material with 70% to 85% reflectivity. Hohl-Ebinger and Warta broke down the measurement uncertainty as a function of photons transmitted through the cell and reflectivity from photons of 900 nm to 1200 nm wavelength by the reflective stage [50]. These cell-to-module power transfer models would overestimate the current gain as the conductive measurement stage used and the normal backsheet have different reflectances.

2.3.2 Measurement Tests For Bifacial Module

In comparison to the bifacial cell test, the current gained from these additional photons is not present in bifacial module measurement, resulting in high cell-to-module current losses for bifacial modules. At the time of writing, there is no defined standard in the power measurements for the bifacial module. In addition to the error from front-side power measurements, the additional rear-side power has no defined measurement standard at the cell and module level. Under outdoor conditions, bifacial modules are illuminated from both sides. However, most setups for indoor flash tests are single-side illumination with cell or module front and rear efficiency being measured sequentially. As a result, the bifaciality factor is commonly reported as the rear side short circuit current divided by the front side short circuit current [51].

In 2012, Singh et al. first reported a new method of reporting the equivalent bifacial efficiency to consider the additional power gain from bifaciality. This method first measures the front and rear characteristics independently before the equivalent bifacial efficiency is calcu-

lated [52]. As the solar cell has only one p-n junction, the illuminations from both rear and front contribute collectively to the current generated. The published work from Razongles et al. reported that the equivalent bifacial efficiency could be evaluated linearly by extrapolating the front side efficiency with the increase of injected illumination from the front [53]. This linear approach resulted in an increasing error up to 7% above 120% of total illumination. An exponential difference in fill factor and series resistance was observed from changing the bifacial illumination to its equivalent single-side illumination.

An updated one-diode model proposed by Singh et al. in 2014 takes into account the increase in series resistance with single-side illumination, which reduces the error to 1% [54]. An enhanced series resistance correction model method was proposed by Zhang et al. to correlate single-side to bifacial illumination to be within 0.3% [55]. This model builds upon the one-diode parameterisation extraction using a penalty-based differential evolution method with series resistance correction to reduce the equivalent efficiency measurement error. However, it is also noted by Zhang et al. that the equivalent efficiency error reduces for cells with higher bifaciality. Considering the above, the need for a new bifacial module test standard is required.

2.4 Existing Method to Compute Bifacial Module Performance

2.4.1 Bifacial Module Irradiance gain

The solar module generates electricity via the photovoltaic effect thus, the main factor that affects its performance is the solar cell's ability to convert the irradiance received into electricity. As discussed in Section 2.2.2, multiple factors such the doping and cell structure affect the solar cell conversion efficiency. As a solar module mainly consists of glass, encapsulant and interconnection, the main contribution to the solar module's performance is the additional irradiance, which these materials could either reflect or transmit to the solar cell. This additional irradiance contributes to the module generated current and its performance [56]. Thus, the researchers in this field report the performance improvement, in terms of irradiance gain, which is the percentage of additional irradiance that the solar cells received in watt per meter square (W/m^2), as compared to the 1000 W/m^2 at STC.

2.4.2 Ray Tracing

Optical ray tracing simulation has been used to analyse the effect of module material on the module current gain. Figure 2.11 shows a cross-section of the bifacial cell in a monofacial module. In this figure, the optical pathway of incoming rays are illustrated. The incoming rays hit the

backsheet and disperse into a uniform diffused and reflected set of rays, which are then reflected at the top side onto the cell. McIntosh et al. first proposed a simple ray tracer to calculate the additional rays that are reflected onto the cell active area from the inter-cell gap [57]. Additionally, McIntosh et al. described the five optical losses in the module: 1) Reflection from the front glass; 2) Absorption in glass; 3) Absorption in the encapsulant; 4) Absorption in the backsheet; and 5) Front surface escape losses. It was reported that there was an increase in losses from the additional passes of light when the inter-cell gap distance increased [58]. Guo et al. investigated the current increase from using halved cells using the optical ray tracing model. In this work, it was reported that a gain of 2.88% could be achieved due to the increase of inter-cell gap area to the active cell area from halved cells [10].

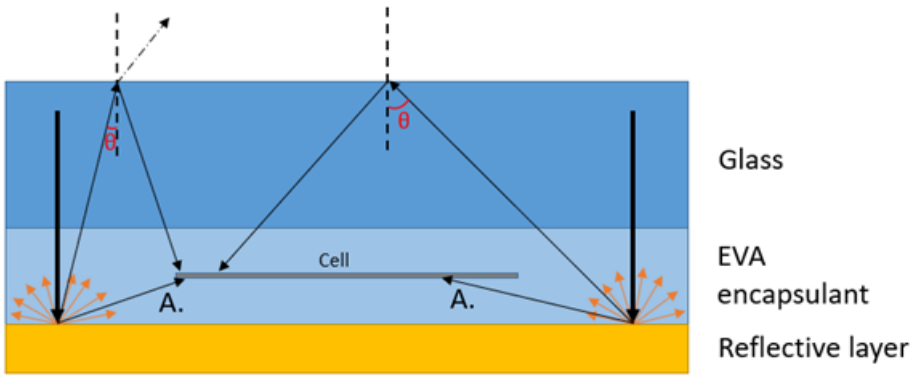

Figure 2.11: Bifacial cells in monofacial module with internally scattered rays path labeled A to the rear of the cell and towards the front of the cell via reflecting back from the front glass / air interface

The optical ray tracing model used by both McIntosh and Guo considers the translational movement of the light rays that are being reflected in the module. Furthermore, Snell's law and Fresnel equations were used to determine the remaining power of the reflected light, with respect to its original power of the incident light. Subsequently, Su et al. presented that by changing the reflectivity of the backsheet from 70% to 90%, the module performance improved by 10%. In addition, Su et al. reported that the maximum gain of 0.25% is achieved with a 6 mm inter-cell gap distance [59]. Similarly, Jai et al. reported an exponential decrease in performance gain from the increase of inter-cell gap distance [8]. The increase of absorption losses with light passes reported by McIntosh et al., describes the reported decrease in performance gain reported by both Su et al. and Jai et al. The optical ray tracing simulation was used to optimise monofacial module power, with respect to its inter-cell gap distance. However, bifacial modules have various module configurations that require additional design factors to be considered, in addition to the inter-cell gap distance like the location of the reflective layers and the impact of this layer on the module performance during rear illumination.

Further work on a simplified ray tracing approach from Jung et al.on bifacial cells in bifacial modules with a white reflective coating at the cell gaps, shows the same linear gains with increasing cell gap, like its monofacial cousins [60]. With the additional collection of light at the rear side of the cell, the magnitude of the gain reported is higher at 2%. for bifacial cells, as compared to Su et al reported values of 0.25% for monofacial cells. Additionally, Jung et al. reported that while these reflective layers greatly improve the module performance from front illumination, there is a drop in the module gain of -2.5% under rear illumination. Thus, under the front and rear side illuminated condition, an optimisation of module mounting is needed for bifacial modules with white reflective layers, to harvest the front illumination gains and reduce the rear illumination losses.

Outdoor energy yield monitoring on bifacial modules with a white reflective layer was conducted by Yin et. al. in Yangzhou, China, and Witteck et. al. in Hamelin, Germany with both reporting a current gain from the reflective layer in bifacial modules. These bifacial modules were measured through indoor front illumination flash tests, producing current gains of 3.1% for the former and 1.6% gains for the latter [61] [62]. However, the outdoor energy yield for Yin et. al. shows a gain of 6.9% for bifacial modules and 10.2% for bifacial modules with a white reflective coating. As solar modules are sold in dollar per watt, based on its indoor front illumination flash test, the bifacial modules with white reflective coating only give an additional 0.5% gain, as compared to those bifacial modules without the white reflective coating when normalised with its indoor front illumination flash test. This drop in outdoor performance gain, as compared to its indoor front illumination flash test gain for bifacial modules with a white reflective coating, was also reported by Witteck et. al. which sees the gain reducing from 1.6% to 1.3%. To quantify the drop in performance gain, Witteck et.al broke down the module outdoor performance to the incoming measured point of array irradiance, as shown in Figure 2.12, during its outdoor energy yield monitoring. From the graph, the current gain of bifacial modules with white reflective coating is more prominent with higher incoming irradiance, which is similar to what Yin et. al. reported. This correlates with the better performance of those modules with white reflective layers during indoor illumination flash tests, which are done at 1000 W/m^2.

While a better indoor front-illumination flash test performance for bifacial modules with white reflective coating was reported by most researchers, their outdoor performance varies due to the non-standardised outdoor operating conditions. In Yin et. al. and Witteck et. al., the modules were mounted south facing at a fixed 25° and 35° respectively. These tilt angles are optimal for front irradiance collection and not at 90° for bifacial modules shared by Guerrero-Lemus et. al., which is more beneficial for bifacial modules [51]. As the location of the white reflective coating differ from the method in which the researchers manufactured their modules, the bifacial module design, white reflective coating location, and mounting conditions would require further optimisation, which is presented in Chapters 3 and 4.

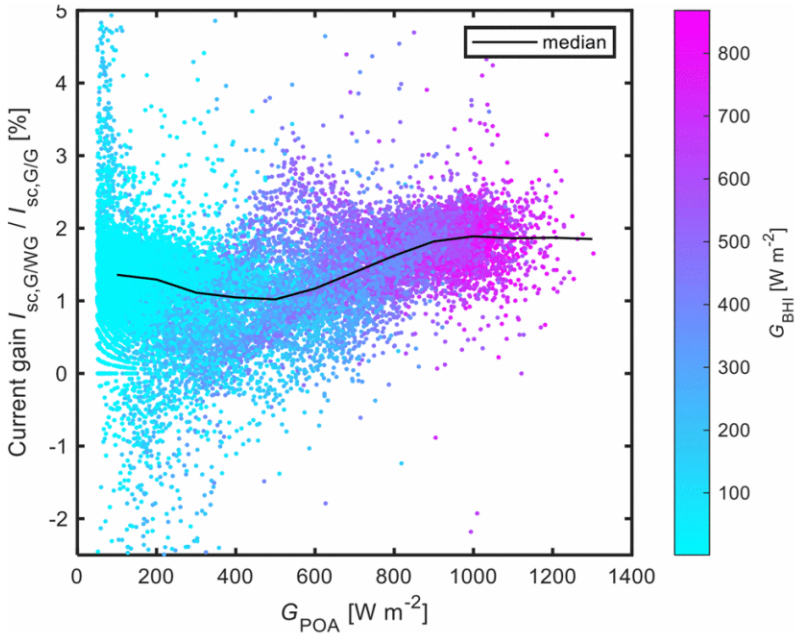

Figure 2.12: lsc gain for the Glass/Glass bifacial modules with reflective coating relative to the Glass/Glass bifacial module as a function of the plane of array irradiance. Color scale indicates the irradiance intensity [62]

2.5 Calculation of Outdoor Energy Yield for Bifacial Module

For the calculation of the energy yield of a module, the module efficiency and the solar irradiance of the site location and mounting angle have to be considered, as shown in Figure 2.13. It is unfortunate that the results from the equivalent bifacial efficiency cannot be correlated to the outdoor energy yield performance as back irradiance is not considered in current outdoor prediction models.

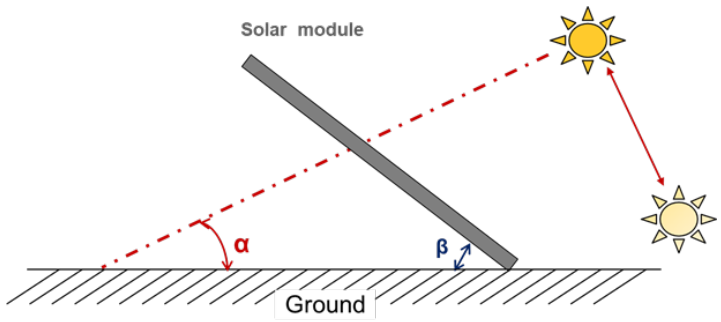

Figure 2.13: Monofacial energy yield schematics with direct irradiance from the sun to module only

A bifacial energy yield model proposed by Wang et al., as shown in Figure 2.14, included

the effect of ground reflectivity (R) and mounting height (h) to the conventional model [12]. It was reported that ground reflectivity, mounting height, and location latitude determine the amount of direct irradiance that is incident onto the ground under the module. For solar module arrays, the mounting distance from module to module affects the self-shading for this direct irradiance. Deline et al. proposed an improved model on the outdoor energy yield modelling, which builds upon the calculated equivalent bifacial efficiency from a single front-side illumination with ground reflectance [63]. A ray tracing model was used to find the corresponding back irradiance incident from the ground reflectance. From the analysis, it was reported that a single mounted module with 1000 W/m^2 front-side illumination would result in approximately, 130 to 140 W/m^2 of equivalent rear illumination, with a ground reflectance of 21%.

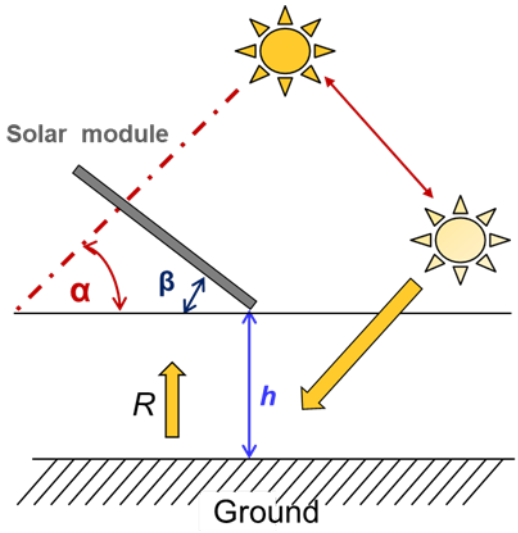

Figure 2.14: Bifacial energy yield schematics with inclusion of mounting height and ground reflectance

With the conventional rooftop and field application, 14% additional energy gained from the ground reflectance was observed on bifacial modules [64]. The performance ratio of photovoltaic systems considers the actual output divided by the nominal calculated output. A typical monofacial photovoltaic system has a performance ratio of 80% to 90% due to resistive and thermal losses. However, the performance ratio calculated output only considers the front-side power under standard test conditions. Hence, bifacial systems have a direct increase in performance ratio due to the additional power gain compensating for the resistive and thermal losses, as illustrated in Figure 2.15. This additional gain is currently quantified with module bifaciality ratio and ground reflectance [65].

Bifacial solar modules could be also mounted vertically as sound barriers or fences, as compared to the conventionally mounted monofacial modules that are tilted towards the equator. Such vertically-mounted bifacial modules have a different energy generation curve, as shown

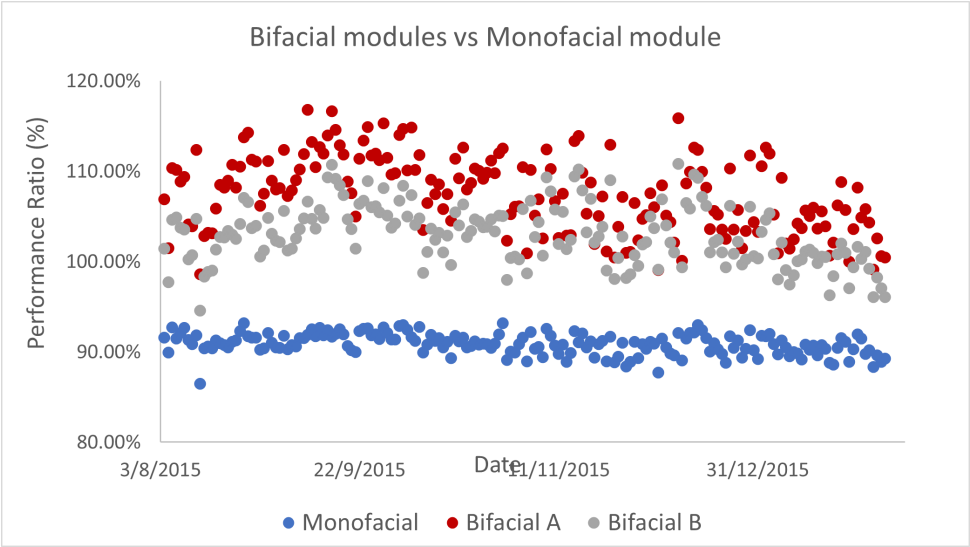

Figure 2.15: Performance ratio of photovoltaic systems with monofacial modules performing lower than both bifacial modules

in Figure 2.16. Both mountings address the varying electricity demands from the grid across the day. Guo et al. reported that the factors that influence the energy yield for bifacial module mounting orientation are latitude, local diffused irradiance, and ground reflectance [66].

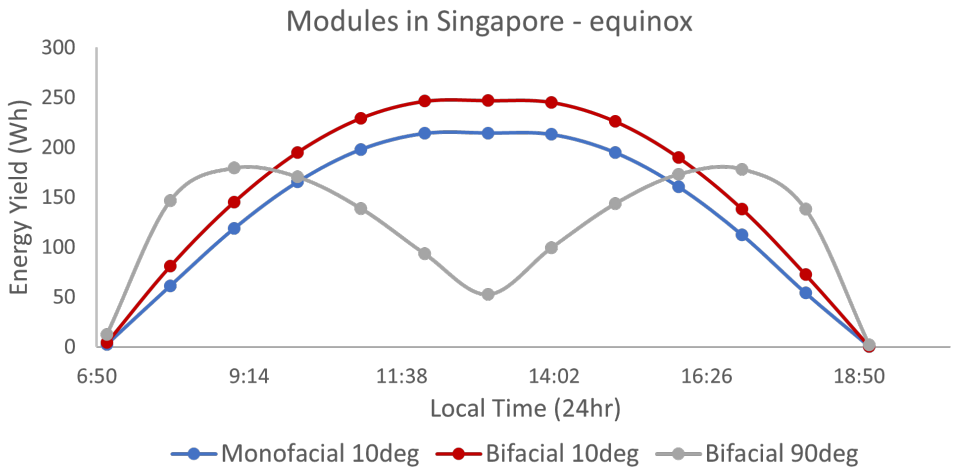

Figure 2.16: Simulated energy yield on equinox in Singapore with bifacial module outperforming monofacial module in the same mounting angle

While the simple ray trace models are able to generate the reflected irradiance from the ground that could be simply added to the module energy yield, a more detailed breakdown of the interaction between the incoming irradiance and the ground reflected rays to the module and into the cell is needed [67]. Reported works from Liang et. al. identified that the spectra response of the bifacial module rear should be measured and the reflected irradiance spectrum should be defined to give a more accurate model [68]. Reported works investigating the spectra

response of the cell and reflected spectrum by Pal et. al. show that the model with 1.1% to 8.5% accuracy could be achieved on clear sky days [69]. Furthermore. Pal et. al. demonstrated that the angular dependence of the ground-reflected rays must be taken into account, to reduce the uncertainty of the model to below 15%, which was done via in-house ray tracing from the ground-perspective [70]. Extensive comprehensive studies were done on different ground material reflected rays and the generated energy yield by Ganesan et. al. and Muthu et. al for bifacial modules, showing an increase in energy yield, which linearly correlates with the increase in ground reflectance [71] [72]. To improve the accuracy of the ray tracing model, most researchers would increase the resolution of the rays. However, as emphasised by Durusoy et. al., such models require high computational power and thus would not be easy to implement in real-life scenarios. A simple and accurate model would enable more researchers to work on this field [73].

The reported work from Pal et. al., Ganesan et. al. and Muthu et. al. on bifacial modules shows the impact of ground-reflected irradiance affecting the accuracy of these models in the prediction of bifacial module performances. However, all three works assume a uniform reflected irradiance from the ground. It is reported by Gu et. al. and Eduardo that the non-uniform rear-side irradiance for bifacial modules is one of the main contributors to the differing outdoor performances between bifacial modules. Thus, the deviation from simulated results [74] [75]. Gu et.al. re-emphasised the current lack of bifacial module models, which could simulate the non-uniformity irradiance from the ground reflected rays. Outdoor monitoring results reported by Riana and Sinha show that the non-uniformity of rear-side irradiance reduces with the increase in mounting height from the reduction in self-shading [67]. This self-shading phenomenon happens when the bifacial module shades the ground below the module from the sun, hence inducing a non-uniform ground-reflected irradiance from its own shadow. As this self-shading is a function of the sun's position, Riana and Sinha further reported an increase of non-uniformity when the sun is directly above the module, as the module shadow is cast nearer to the module. This period of high non-uniformity directly coincides with the period of highest irradiance, thus hugely affecting the bifacial module performance from the mismatch losses [76].

In the same mounting condition, a bifacial module would give additional energy yield from the absorption of light from the rear, as compared to a monofacial module. However, the front-side efficiency for bifacial modules under standard testing conditions would also be lesser due to its inherent transmission property. This leads to the increase of bifacial modules with white reflective coating being manufactured, which would reduce such losses. Most reported works illustrated the importance of the mounting condition due to differing ground reflectance, which affects the additional rear irradiance for standard bifacial modules. To the best of our knowledge, few reported works on the simulation or outdoor energy yield studies were done on bifacial

modules, which relates to the optimisation of the location of the white reflective coating in the module design and its mounting conditions for energy yield optimization. This will be further studied in Chapter 5.

2.6 Calculation of Current Gain For Bifacial Module Performance

The fundamental benefit of the bifacial module over the monofacial module is its ability to absorb additional irradiance from the rear. This additional irradiance could be from the module's internal reflectance from the reflective coating in the module, as discussed in Chapter 2.2.2 or from ground reflected irradiance which was discussed in Chapter 2.5. The additional absorbed irradiance increases the module performance by generating additional current above what the module is already generating in a monofacial setting.

As module design impacts the current generated in a monofacial setting, the performance analysis of the bifacial module is conducted by dividing the additional current from the bifacial module by the amount of current generated by the monofacial module [77]. While the module current gain indicates a gross comparison of the bifacial module performance, an in-depth modeling that considers the ground-reflected irradiance and tilt, would provide a more accurate performance analysis of the bifacial module [78]. A comparison of current gain from their simulation model to the actual outdoor performance for a tilted bifacial module was previously reported as 6.1% by Sun et. al. [79]. Upon breaking down the current gain contributed only by the rear irradiance, their simulation model shows an error of 12.5%.

$$RMSE = \sqrt{\frac{\sum_{i=1}^{N}(e-m)^2}{N}} \tag{2.1}$$

As monofacial modules are common and extensively studied, existing monofacial current models are more accurate, as compared to those that include ground-reflected irradiance. A mean error value could indicate any over or under-estimation of current gain for the monofacial model but a mean error from the front and rear irradiance separately affects the sensitivity of the simulation model for forecasting bifacial modules current gain. The Root Mean Square Error (RMSE) shown in Equation 2.1 which was reported by Alam et. al. [80], can be used as an indicator of the magnitude of the error where the difference between simulated values e and measured value m are squared and sum across all observed data point N to report the over or under-estimation of their model. For more accurate results, they have also included a clearness index, which is the ratio of ground-reflected irradiance to the irradiance incident by the sun [80]. To report the simulated results correlation to the actual experimental values, RMSE was also

used by Betti et. al. to compare commercial bifacial module models to their outdoor experiment data [81] and by Aly et. al. for their thermal module for bifacial modules [82].

2.7 Summary

In this chapter, the merits of the bifacial cells and modules with their generation of additional current from the absorption of solar irradiance at the rear of the module were discussed. Next, the solar cells and module design processes, fabrication method, and material used were laid out. The difference in module design for bifacial glass/glass and monofacial glass/ backsheet modules was studied. The existing indoor test and measurement for cell and module were discussed and the lack of a bifacial measurement standard that correlates to its actual outdoor performance was identified. The proposal of having a reflective coating in bifacial modules to reduce the transmittance losses was shown and reported to improve the bifacial module's performance. However, to the best of our knowledge, there isn't any published work on the optimal integration of the reflective coating into the bifacial module and its impact on the module performance.

Ray tracing models were discussed, which have been used extensively for the performance evaluation of monofacial module performance. Their use in the bifacial module to include the additional current contribution from internal-reflected irradiance on those white reflective layers is only starting to gain popularity. Its use to simulate module performance of these white reflective layers in bifacial modules under varying outdoor mounting conditions of tilt, mounting height, and location was discussed. This is followed by a review of the contributions of ground-reflected irradiance to the bifacial module's current. The non-uniformity of these ground-reflected rays was reported by fellow researchers to be the main cause of performance deviation for their models. An optimisation of the module mounting condition by reducing self-shading was proposed as a mitigation method for the non-uniformity of ground-reflected rays. To the best of our knowledge, there is very little work to investigate the effect of the non-uniform ground-reflected irradiance on the bifacial module with white reflective layers. By closing this research gap in the optimisation of bifacial module design and mounting conditions for bifacial modules with reflective layers, superior performance can be realised, which would enable the reduction of LCOE of solar energy for wider adoption of this low-carbon energy source. In the last section of this chapter, the use of the RMSE was discussed to provide a more accurate indication of the magnitude of the error.

In the next chapter, an investigation of various bifacial module configurations will be discussed. The inter-cell gap regions and configuration of the reflective layer will be modelled using optical ray tracing.

Chapter 3

Investigation and Analysis of Current Gain in Bifacial Modules with Reflective Inter-cell Gap

As discussed in Chapter 2, the monofacial and bifacial module configurations could be modelled by optical ray tracing in MATLAB to analyse the module configuration contribution to the current gain. In this chapter, different configurations of bifacial modules are discussed in Section 3.1. This is followed by the optical ray tracing model in Section 3.2. The necessary assumptions and experimental inputs are presented in Section 3.2.1. Optical ray trace equations are explained in Section 3.2.3 with consideration of absorption losses in Section 3.2.4. The simulation results, validation and analysis are presented in Section 3.3.

3.1 Different Configurations of Bifacial Modules

Bifacial PV cells can be encapsulated into the typical monofacial solar module structure, which has cells sandwiched between the encapsulant with glass on the front side and white backsheet on the rear, as shown in Figure 3.1. While bifacial modules come in a few different structures, the standard bifacial module in Figure 3.2 of Glass / EVA / Bifacial Solar Cell / EVA / Glass or Transparent backsheet could capture additional sunlight to the rear from ground reflectance [12] [13] [66] . Without the full reflective layer of monofacial modules that contributes to the module internal reflectance [10], there is power loss in bifacial modules, as compared to the monofacial modules due to the outward transmission of light rays during indoor flash test [8].

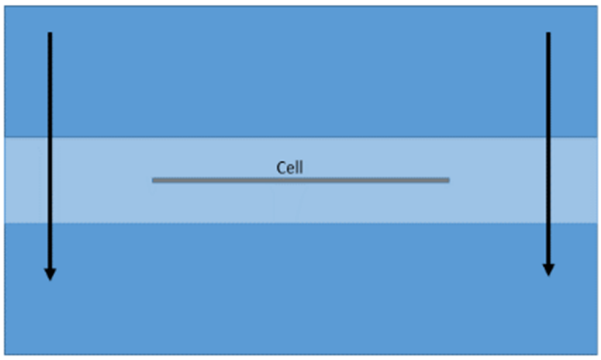

Figure 3.1: Standard bifacial module with transmission losses when light rays pass through the module and are not absorbed by the cells

Recent developments of bifacial modules, with a reflective layer inserted between the cell, increase the module front side current without totally removing the bifacial capability of the module [8] [7]. In this structure, various configurations with varying locations of the reflective surface were proposed. The three main configurations differs where the reflective surface was inserted: Configuration 1 (C1) behind the rear glass or transparent backsheet in Figure 3.2, Configuration 2 (C2) in between the glass and encapsulant in Figure 3.3, and Configuration 3(C3) in between the encapsulant in Figure 3.4. Acronyms of C1, C2, and C3 are used in graphs representing the three different bifacial modules with white reflective coating.

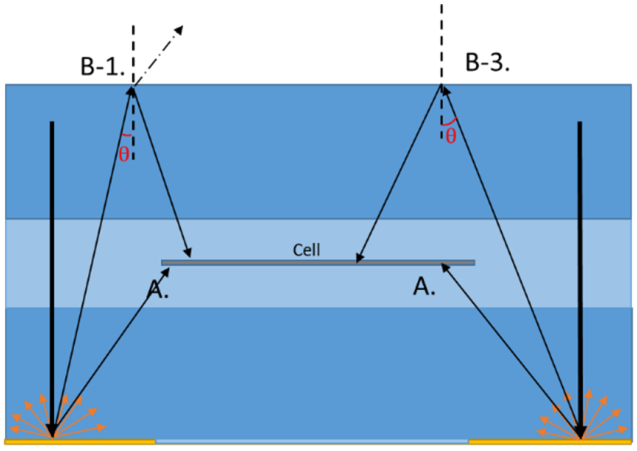

Figure 3.2: Bifacial module reflective layer on the rear of rear glass in Configuration 1 reflecting the incoming rays to A) rear of cell, B) front of cell

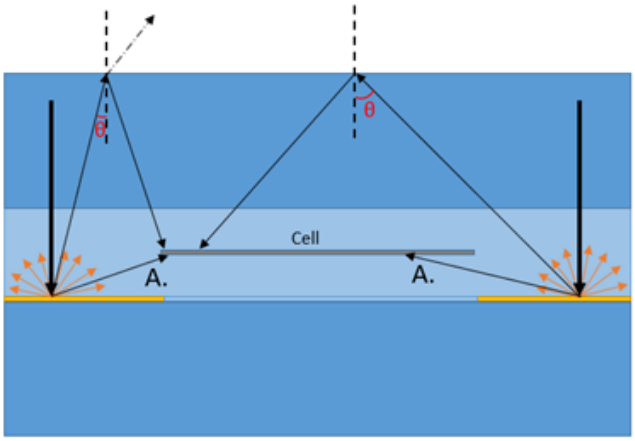

Figure 3.3: Bifacial module reflective layer on the rear glass in Configuration 2 reflecting the incoming rays to A) rear of cell and other rays to front of cell

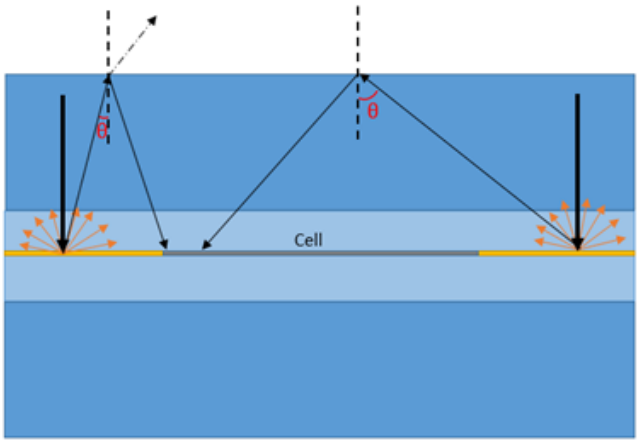

Figure 3.4: Bifacial module reflective layer on the same level as the cell in Configuration 3 reflecting the incoming rays to front of cell only

In the monofacial module structure and bifacial module structure with reflective layer of Configuration 1 and 2, the incoming light from the front of the module is reflected onto both the front and rear of the cell. The light ray traces are shown in Figure 2.11, Figure 3.2, and Figure 3.3 with arrows marked “A”. The standard bifacial module structure and all three bifacial module structures with reflective layer allow the ground reflectance to be captured by the rear of the active cell, as shown in Figures 3.1 to 3.4. The location and distance of the reflective layer determines the amount of ground reflectance reaching the cell.

The influence of the cell gap to monofacial cells in monofacial modules were widely reported. With a wider cell gap, the reflectivity area increases, and in turn the cell current [10] [59] [83]. For bifacial modules, strategic placement of the reflective surface affects the module performance during STC and outdoor monitoring has to be discussed.

3.2 Numerical Model

In this section, the front and rear current of the bifacial module structures highlighted above will first be analysed. The equations on light scattering and probability of collection by the active cell area are first modelled with optical ray trace and then coded. Secondly, physical measurements performed on the materials are provided as inputs into the numerical model. Lastly, the output results from the model are validated with indoor flash tests. The simplified flow of the numerical model is shown in Figure 3.5.

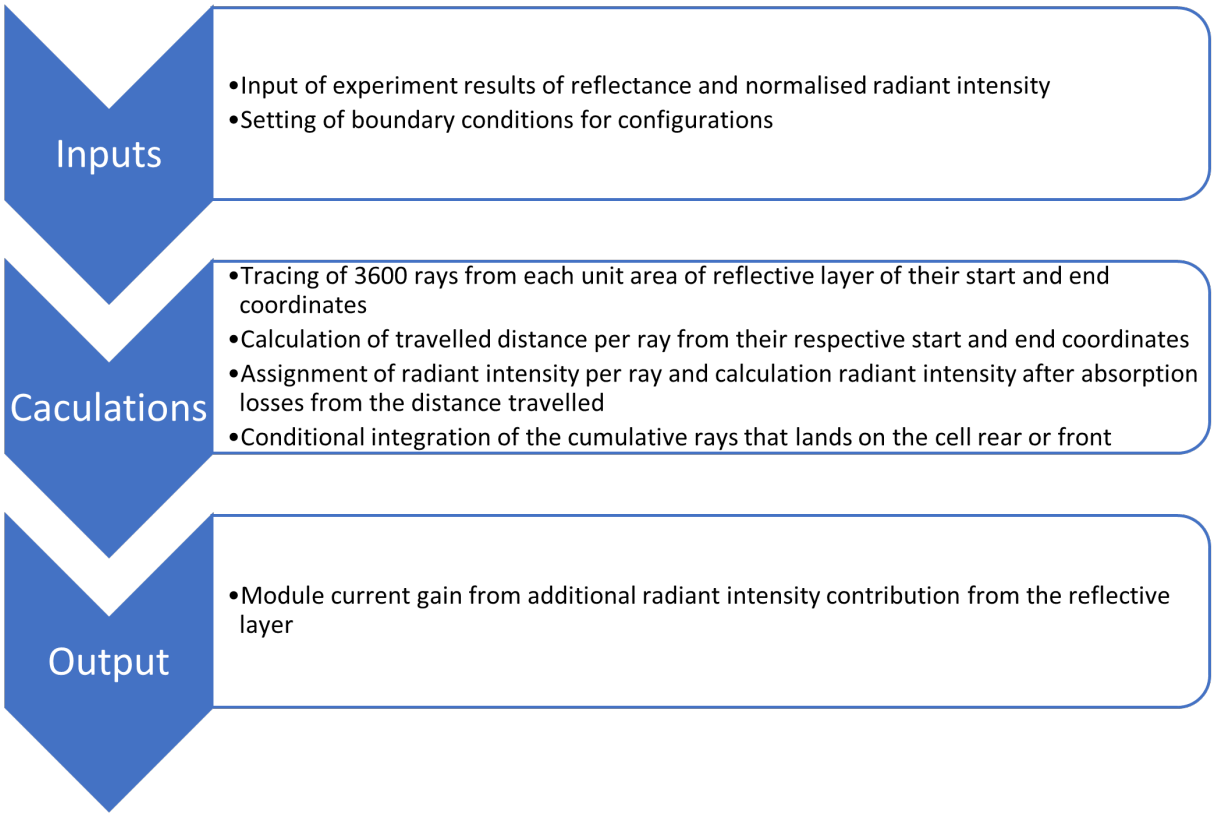

Figure 3.5: Simplified flow diagram of numerical model with the inputs, calculations assumptions and outputs

3.2.1 Assumptions and Inputs

Firstly, assumptions on the refractive index of the materials were made prior to the start of all simulations. The glass and encapsulant refractive index are assumed to be the same, as the optical loss through reflection at this particular junction is very small and can be negligible [84]. The refractive index of glass and encapsulant is set at 1.5 and the refractive index of air is set at 1 [10] [84].

Secondly, it is considered that the reflective layer will scatter the light that falls on it into different directions. To cover all possible directions of the scattered light, the directions are

divided into two segments which is the azimuth and polar directions. The assumption of the direction of light was made the same such that it is scattered uniformly at interval of 3° in the polar coordinates and at intervals of 6° in the azimuth coordinates, resulting in a total of 3600 rays. The reflected rays were also assumed to be unpolarised, thus consisting of parallel and perpendicular light. The radiant intensity of rays is assumed to be negligible after two bounces. Lastly, the white area is divided into unit areas of $1mm^2$ which reflects an individual ray into each unit area of the module.

Two experiment inputs for the numerical model were measured by spectrometer, namely the normalized reflected radiant intensity shown in Figure 3.6a and the reflectance of the reflective layer plotted in Figure 3.6b. The wavelength of 632nm was chosen to represent the angular scattering of the spectrum AM1.5G on the reflective layer. Its weighted average reflectance is also calculated, with respect the AM1.5G spectrum.

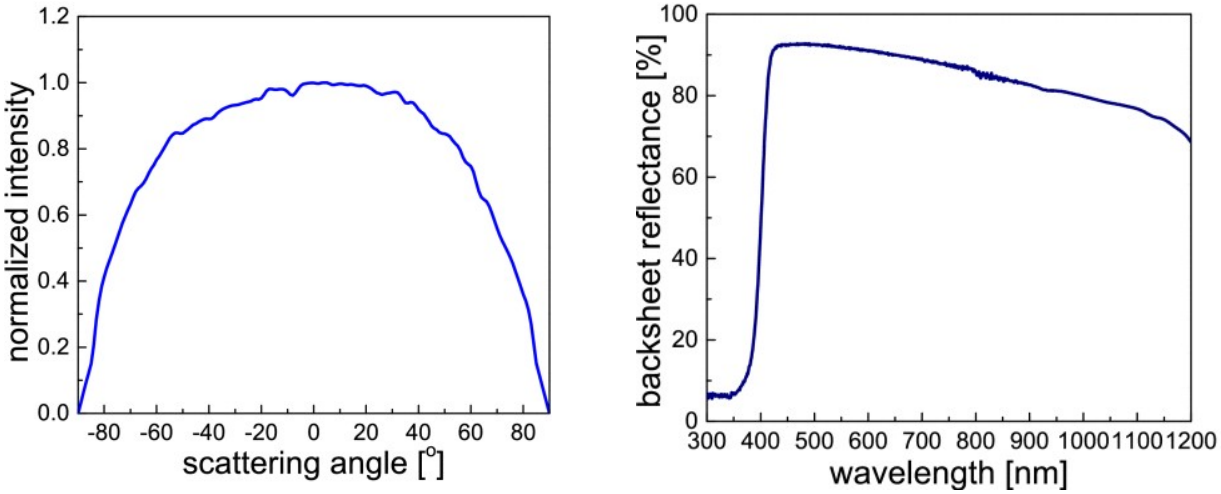

(a) Normalized radiant intensity

(b) Reflectance of backsheet

Figure 3.6: Input parameters from reported works which was referenced for reflective coating [84]

3.2.2 Current Measurement on Modules

For quantification of the reflection of light rays on different module configurations, a monochromatic localised light source was used to measure the quantum efficiency of the mini modules. Measurements was done on the middle of the cell in Figure 3.7a and on the edge where only half of the light is incident on the cell in Figure 3.7b. Different module material was chosen to best match the three configurations discussed due to the limitations of materials. Firstly, the standard bifacial module, as shown in Figure 3.1 is represented by the module with black backsheet, which does not reflect any light. For Configuration 1 and 2, which are illustrated in Figure 3.2 and Figure 3.3, the module with white backsheet was used to demonstrate the additional rays

reflected to the rear of the cell. For Configuration 3, which is shown in Figure 3.4, the reflective layer is along the same plane as the cell was represented by the module with white encapsulant.

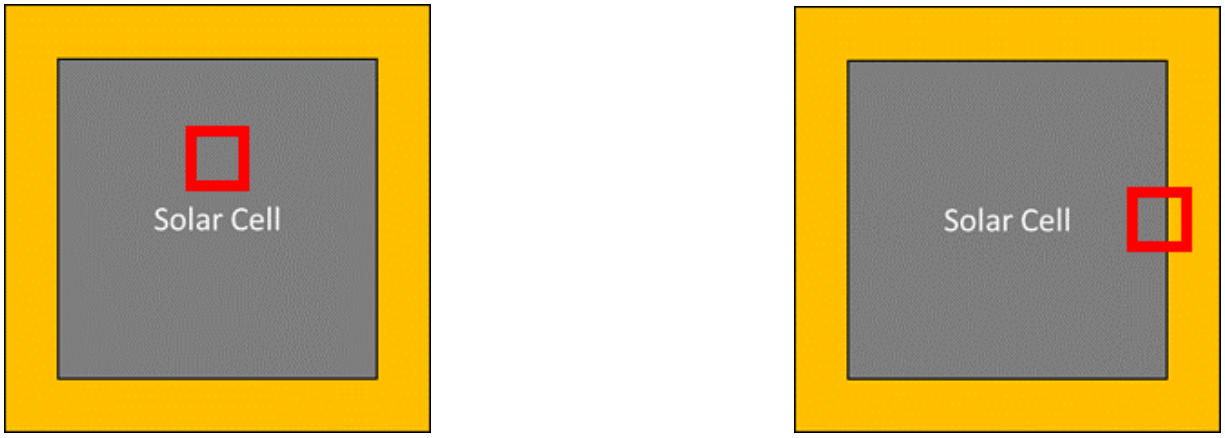

(a) Top view of Spot 1

(b) Top view of Spot 2

Figure 3.7: Top view of Spot 1 measurement of cell and underlying module material through cell. With additional module material directly exposed for spot 2

The changes of module materials were on the rear side, which result in the deviations of the External Quantum Efficiency at wavelength 800nm to 1200nm. In Figure 3.8, the difference between the reflective layers (in white encapsulant and white backsheet) compared to the black backsheet, shows the slight influence of transmitted light on the current gain of the module. As discussed in Section 2.2.1, the absorption coefficient of solar spectrum in silicon solar cell peaks at the wavelength of 300nm and reduces gradually till 800nm before a significant drop after 800nm. With the reduction of absorption of solar spectrum beyond the wavelength of 800nm, more light is transmitted through the bifacial cell and on to the module material on the rear side. These transmitted light through the bifacial cells are totally absorbed by the black backsheet while in the modules with reflective layers, these transmitted light are reflected back into the module, hence contributing to additional current being generated.

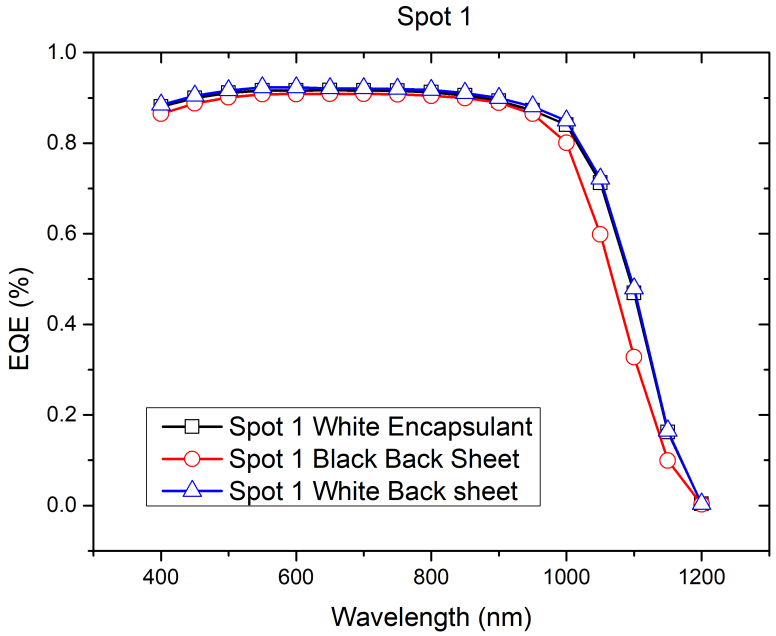

Figure 3.8: EQE Spot 1 measurement results with different underlying material on rear of solar cell with black backsheet having lower EQE(%), as compared to the white encapsulant and white backsheet due to the absence of long wavelength light being reflected back to the cell.

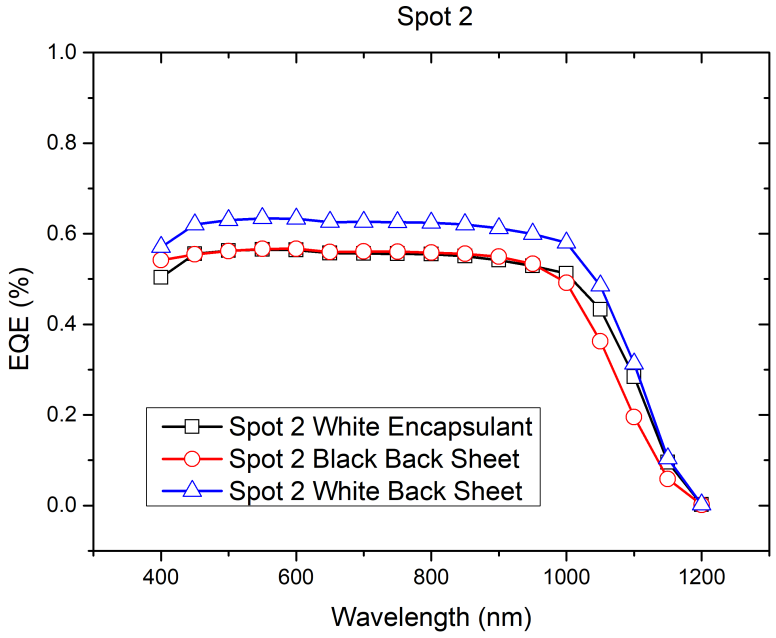

Figure 3.9: EQE Spot 2 measurement results with different underlying material on rear of solar cell. The EQE of the black backsheet is the lowest due to the lack of internal reflectance and that of the white backsheet is the highest due to the additional light rays being reflected to the rear of the cell, as compared to the white encapsulant.

In Figure 3.9, the difference in the module material has a more significant effect on the result due to localised light that is shined on the edge. The different regions bounded by the curves are due to the increase of current from the different module configuration. The area bounded by the white backsheet and white encapsulant curve indicates the additional gain from the light rays that are reflected by the backsheet and incident on the rear of the cell. The light that is reflected to the front of the cell consists of the area between the white encapsulant and black backsheet curves. This experiment illustrated the ratio of current gain contributed to the front and rear of the cell by the different configurations.

3.2.3 Optical Ray Trace Equations

When light falls on the white area, it will be scattered into different directions. However, the intensity of the scattered light will vary according to the reflectivity of the white inter-cell gap. The calculation of the irradiance at certain direction (θ), after reflection from the backsheet is performed using Equation 3.1 [8, 10]

$$S(\theta) = aue \times \phi_p \times WAR_{bs} \times \frac{Sn(\theta)}{\int_0^{\pi}\int_0^{\alpha} Sn(\theta) \times \sin\theta d\varphi d\theta}, \tag{3.1}$$

where *aue* is the unit area of the backsheet, ϕ_p is the power of incident light per unit area of backsheet, WAR_{bs} is the backsheet weighted average reflectance, $Sn(\theta)$ is the measured normalized reflected radiant intensity of the backsheet, θ is the angle between the scattered ray direction and the surface normal (polar angle), and φ is the azimuth angle in the spherical coordinate system.

The white inter-cell gap will reflect off the ray that is incident on it into different directions. Rays will either transmit out of the module or be reflected internally inside. A matrix consisting of the coordinated of the module had been simulated to determine the possible locations of the reflected rays. Some assumptions made are the uniform separation of scatted rays across the polar and azimuth angle, and the non-contribution of cells irradiance after two bounces. The contribution of reflected light that hits the rear side of the cell the position vector of the ray are computed by the Equations 3.2 and 3.3 with x_1 and y_1 being the initial coordinates and x_2 and y_2 being its final coordinates on the rear of the cell, and t_1 is the thickness of rear encapsulant.

$$x_2 = x_1 + t_1 \times \tan(\theta) \times \cos(\varphi) \tag{3.2}$$

$$y_2 = y_1 + t_1 \times \tan(\theta) \times \sin(\varphi) \tag{3.3}$$

For those rays that were not scattered to the rear of the cell and were reflected by the front glass back to the cell, Equations 3.4 and 3.5 were applied, with x_1 and y_1 being the initial

coordinates and x_3 and y_3 being its final coordinates on the front of the cell, and t_2 and g are the thickness of front encapsulant and glass respectively.

$$x_3 = x_1 + (2g + t_1 + 2t_2) \times \tan(\theta) \times \cos(\varphi) \tag{3.4}$$

$$y_3 = y_1 + (2g + t_1 + 2t_2) \times \tan(\theta) \times \sin(\varphi) \tag{3.5}$$

For the ray with an incident angle more than the critical angle of 41.8°, total internal reflection is considered. If the angle of incident is less than the critical angle of air/glass (41.8°) the reflectance and transmittance radiant intensity are calculated with the Fresnel equation. Through our discussion, the irradiance reflected by the backsheet and incident on the rear of the cell could be calculated, if x_2 and y_2 or x_3 and y_3 is situated on the cell. The cumulative light intensity from the rear and front of the cell are computed by Equations 3.6 and 3.7 respectively, where x is bounded by p_1 and p_2 and y is bounded by q_1 and q_2. The difference, $p_2 - p_1$ is the length of the cell and $q_2 - q_1$ is the width of the cell.

$$P_r = \int_{q_1}^{q2} \int_{p_1}^{p_2} \int_0^{\pi} \int_{\alpha}^{\frac{\pi}{2}} S(\theta) \times T1(x_2, y_2) \times R_g d\theta d\varphi dx dy \tag{3.6}$$

$$P_f = \int_{q_1}^{q2} \int_{p_1}^{p_2} \int_0^{\pi} \int_0^{\alpha} S(\theta) \times T1(x_3, y_3) \times R_g d\theta d\varphi dx dy \tag{3.7}$$

The test function $T1(x_2, y_2)$ is set as 1 if (x_2, y_2) is located in the cell area. Similarly, $T1(x_3, y_3)$ is set as 1 if (x_3, y_3) is located in the cell area. Otherwise, the test functions will be set to a zero value. Thus, only reflected light rays that fall into the front and rear of the cell will be summed up. Here, α is the critical angle for the glass/air interface, which is 41.8° [8, 10, 57].

3.2.4 Absorption Losses

The absorption losses of light, $\alpha_{medium}(\lambda)$, traversing in the glass and EVA could be calculated dependently as encapsulant and glass have the same refractive index to reduce losses. The absorption coefficient of the medium is described in Equation 3.8,

$$Absorption_{medium}(\lambda) = \phi_p(\lambda) \times e^{-\alpha_{medium}(\lambda) \times t}, \tag{3.8}$$

where t is the layer thickness, λ is the wavelength of light and $\phi_p(\lambda)$ is the power of the incident light. This equation could be applied to account for the absorption losses through both glass and encapsulant collectively.

The input light is the sum of the light that are either reflected, absorbed or transmitted [85]. If we are to quantify the absorption losses $\alpha_{medium}(\lambda)$ through the cells' reflectance, absorption, and transmittance, these losses are first measured, which are represented as R_{medium}, A_{medium}

and T_{medium}. This proposed method simplifies the measurement of module material absorption where

$$R_{medium} + A_{medium} + T_{medium} = 100\% \tag{3.9}$$

and

$$Absorption_{cell}(\lambda) = \frac{EQE_{cell}(\lambda)}{IQE_{cell}(\lambda)}. \tag{3.10}$$

As such, Equations 3.9 and 3.10 could be re-written to form Equation 3.11 with the consideration of internal (IQE) and external (EQE) quantum efficiencies across the certain wavelength as per Equation 3.10. The IQE is the percentage of carriers collected per photon incident on the cell less those that were reflected. It was reported by Jai et al. that post module encapsulation, there are little transmission to the external medium [8, 50, 85]. This transfers the losses from the reflectance and transmittance of the cell to the parasitic absorption and reflectance by the module materials, as shown in Equation 3.12.

$$IQE_{cell}(\lambda) = \frac{EQE_{cell}(\lambda)}{1 - R_{cell} - T_{cell}(\lambda)} \tag{3.11}$$

$$IQE_{module}(\lambda) = \frac{EQE_{module}(\lambda)}{1 - R_{module} - A_{module}(\lambda)} \tag{3.12}$$

From experimental values shown in Figure 3.10, it could be assumed that the cell IQE remains unchanged therefore Equation 3.12 equals to Equation 3.11, which could be written as Equation 3.13.

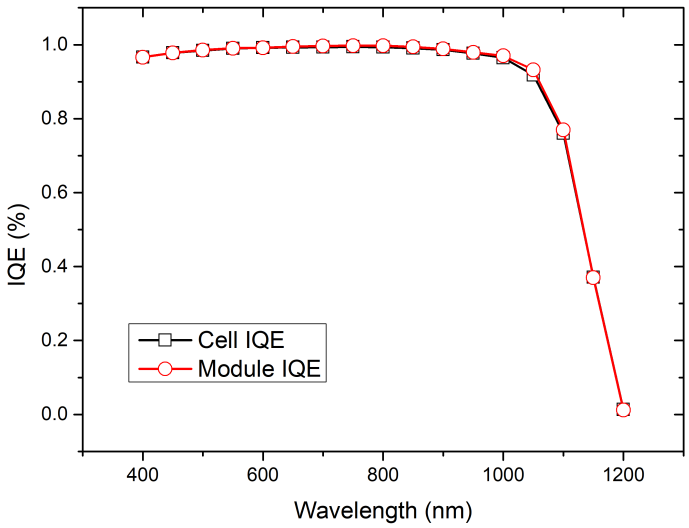

Figure 3.10: Cell IQE remains unchanged when processed into module proving the assumption taken in Section 3.2.4

Equation 3.13 could be rearranged to quantify the absorption of module material, as shown in Equation 3.14.

$$\frac{EQE_{cell}(\lambda)}{1-R_{cell}-T_{cell}(\lambda)} = \frac{EQE_{module}(\lambda)}{1-R_{module}-A_{module}(\lambda)} \tag{3.13}$$

$$A_{module}(\lambda) = 1-R_{module}(\lambda)-[1-R_{cell}(\lambda)-T_{cell}(\lambda)\times\frac{EQE_{encapsulated}(\lambda)}{EQE_{cell}(\lambda)}] \tag{3.14}$$

To calculate the distance travelled by the ray in Equation 3.14, the following are added into the model. The distance travelled by rays incident on the rear of the cell, as shown in Figure 3.11 could be calculated with its known start and end position with Equation 3.15 and 3.16. The resultant distance travelled is calculated by Equation 3.17 to give the layer thickness t, which is travelled by each ray. With x_1 and y_1 as its start position and x_2 and y_2 as its end position.

Figure 3.11: Rear distance travelled from the origin to rear of cell

$$x_2 = x_1 + T_{EVA}\times\tan(\theta)\times\cos(\varphi) \tag{3.15}$$

$$y_2 = y_1 + T_{EVA}\times\tan(\theta)\times\sin(\varphi) \tag{3.16}$$

$$t_{rear} = [(x_2-x_1)^2\times(y_2-y_1)^2\times(T_{EVA}-0)^2]^{\frac{1}{2}} \tag{3.17}$$

For the rays that are incident on the front glass and reflected to the cell, as illustrated in Figure 3.12, they can be broken down into two parts, $t_{front-\alpha}$ and $t_{front-\beta}$. The front travelled distance, A, could be described with Equation 3.20 using $x_{3-\alpha}$ and $y_{3-\alpha}$ where the z-height of $2\times T_{EVA}+T_{Glass}$ could be calculated from Equations 3.18 and 3.19.

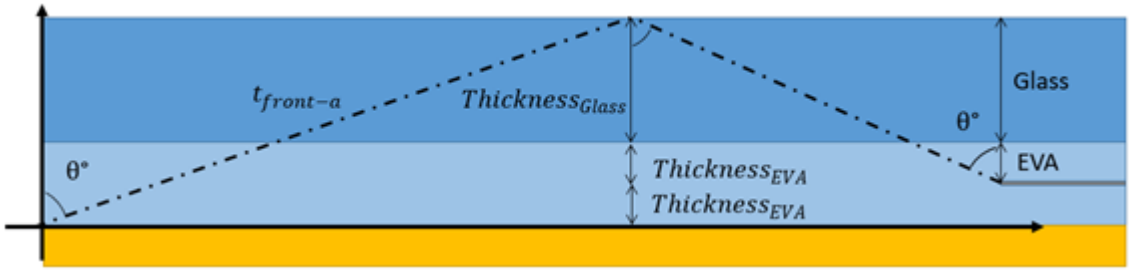

Figure 3.12: Front distance travelled from the origin to rear of cell to the front glass and towards front of cell

$$x_{3-\alpha} = x_1 + (2 \times T_{EVA} + T_{Glass}) \times \tan(\theta) \times \cos(\varphi) \tag{3.18}$$

$$y_{3-\alpha} = y_1 + (2 \times T_{EVA} + T_{Glass}) \times \tan(\theta) \times \sin(\varphi) \tag{3.19}$$

The corresponding front travelled distance, β, is calculated with Equations 3.23 with Equation 3.21 and 3.22 calculating the Cartesian coordinates of the start and end position of the ray.

$$t_{front-\alpha} = [(x_{3-\alpha} - x_1)^2 \times (y_{3-\alpha} - y_1)^2 \times (2 \times T_{EVA} + T_{Glass} - 0)^2]^{\frac{1}{2}} \tag{3.20}$$

$$x_{3-\beta} = x_{3-1} + (T_{EVA} + T_{Glass}) \times \tan(\theta) \times \cos(\varphi) \tag{3.21}$$

$$y_{3-\beta} = y_{3-1} + (T_{EVA} + T_{Glass}) \times \tan(\theta) \times \sin(\varphi) \tag{3.22}$$

$$t_{front-\beta} = [(x_{3-\beta} - x_{3-\alpha})^2 \times (y_{3-\beta} - y_{3-\alpha})^2 \times (2 \times T_{EVA} + T_{Glass} - 0)^2]^{\frac{1}{2}} \tag{3.23}$$

$$t_{front} = t_{front-\alpha} + t_{front-\beta} \tag{3.24}$$

The total front distance travelled by the ray is the sum of part A and B, which is shown in Equation 3.24. Absorption by glass and EVA for each individual ray using Equation 3.24 could then be calculated with the known distance travelled from Equation 3.20 and 3.23. This absorption is a function of distance travelled and radiant intensity of each ray. The effective radiant intensity of each ray could be calculated using Equation 3.25 with the exclusion of the radiant intensity that are absorbed by the glass or EVA.

$$S(\lambda) = S(\lambda) - Absorption_{medium}(\lambda) \tag{3.25}$$

3.2.5 Current Gains

Equation 3.26 calculates the current gain due to the reflected light from the reflective area to the rear of the bifacial cell. This applies to Configurations 1 and 2. Equation 3.27 calculates the current gain due to the reflected light from the reflective area to the front of the cell.

$$Current_{gain\,rear} = \frac{(\frac{Isc_r}{Isc_f}) \times P_r}{\phi_p \times cell\,area} \tag{3.26}$$

and

$$Current_{gain\,front} = \frac{P_f}{\phi_p \times cell\,area}, \tag{3.27}$$

where Isc_r and Isc_f are measured values for short-circuit current from the rear and front of the cell, $\frac{Isc_r}{Isc_f}$ is the bifacility ratio and ϕ_p is the power of the incident light.

Equation 3.28 calculates the total current gain to the cell from the reflective area as

$$Current_{gain} = \frac{P_f + (\frac{Isc_r}{Isc_f}) \times P_r}{\phi_p \times cell\,area}. \tag{3.28}$$

3.3 Results and Analysis

In the previous section, three bifacial module configurations models were discussed and modelled using the optical ray trace. In this section, the simulation model is first verified with a sanity check on the integration of the cumulative light ray in the model. Next, the numerical model is validated with indoor flash test results. Following which, the study of the three different bifacial and monofacial modules configurations is conducted with simulated illumination from the front, rear, and both sides. This will provide the actual performance of the modules in outdoor conditions.

3.3.1 Numerical Model Sanity Check

As discussed in the previous sections, the contribution of current from the inter-cell gap is a function of its distance and the radiant intensity of the rays is assumed to be negligible after two bounces. This numerical model was verified mathematically to ascertain if the simulation model performs correctly for the simulated current gains. Hence, the current saturation point occurs when the increase of cell gap does not contribute to the current gain. Current gain from the cell gap distance is dependent on the thickness of EVA and glass, as described in Equation 3.29 and 3.30 where the maximum cell gap distance from the ray's point of origin that are still contributing to the cell rear or front current, as illustrated in Figure 3.13 and Figure 3.14 .

$$Rear\,Max\,Distance = \frac{EVA_{thickness}}{\tan(\theta_{min})} \tag{3.29}$$

$$Front\,Max\,Distance = \frac{2 \times EVA + Glass_{thickness}}{\tan(\theta_{min})} + \frac{EVA + Glass_{thickness}}{\tan(\theta_{min})} \tag{3.30}$$

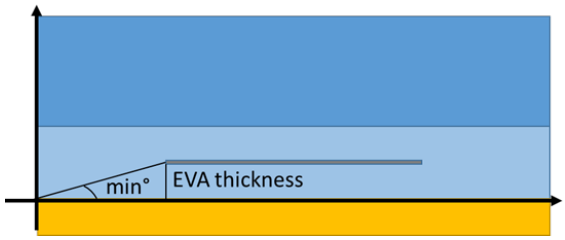

Figure 3.13: Illustration of max rear distance

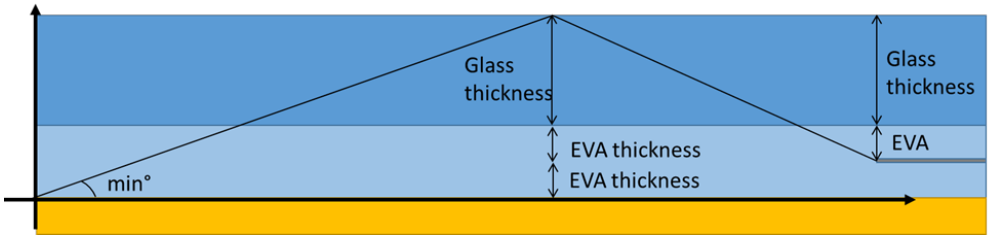

Figure 3.14: Illustration of max front distance

The maximum cell gap distance as calculated were input into the numerical model to verify the saturation point of current gain. Figures 3.15a and 3.15b show the contribution of cell gap to rear and front current gain.

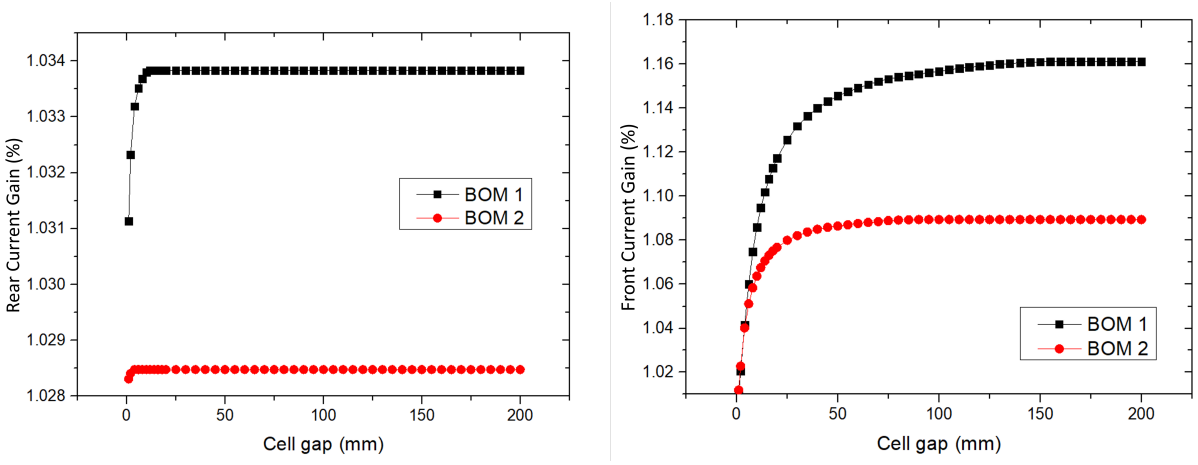

(a) Gain from rear side

(b) Gain from front side

Figure 3.15: Current gain contributions to the front and rear of cell in BOM 1 and 2 with increasing cell gap

The increasing cell gap benefits the front side current, as compared to the rear side current, as more rays are reflected onto the front as the cell gap distance increase. In Figure 3.16, the calculated max cell gaps stated in Table 3.1 were verified for the two different material thickness.

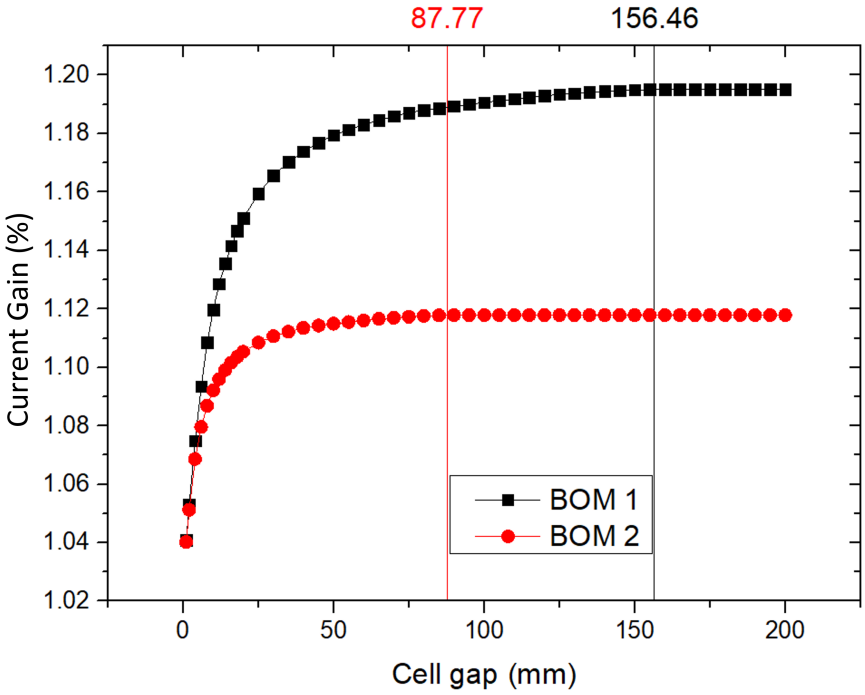

Figure 3.16: Total current gain with varying BOM from front and rear side with labeled cell gap distant for the two BOMs when current gain saturates

Table 3.1: Current gain saturation point of different thickness

Bill of Materials (BOM)	EVA Thickness	Glass Thickness	Rear Saturation Point	Front Saturation Point
1	0.6mm	3.2mm	11.45mm	156.46mm
2	0.2mm	2mm	3.82mm	87.77mm

The current gain from 0mm to 200mm of inter-cell gap was plotted on Figure 3.16. The results from the simulation agrees with the calculated inter-cell gap distance for the saturation point as reported in Table 3.1.

3.3.2 Validation of Numerical Model With Experiment

Prior to the simulation experiment on the three configurations of bifacial and monofacial modules, the simulation result was validated with experiment results for Configuration 3 (C3). This is plotted on Figure 3.17 where the RMSE reduces from 0.018 to 0.012 for C3 WA (C3 with

consideration of absorption losses), as compared to C3 WoA (C3 without consideration of absorption losses) Thus, additional transmission and reflection losses should be considered in the numerical model for better accuracy.

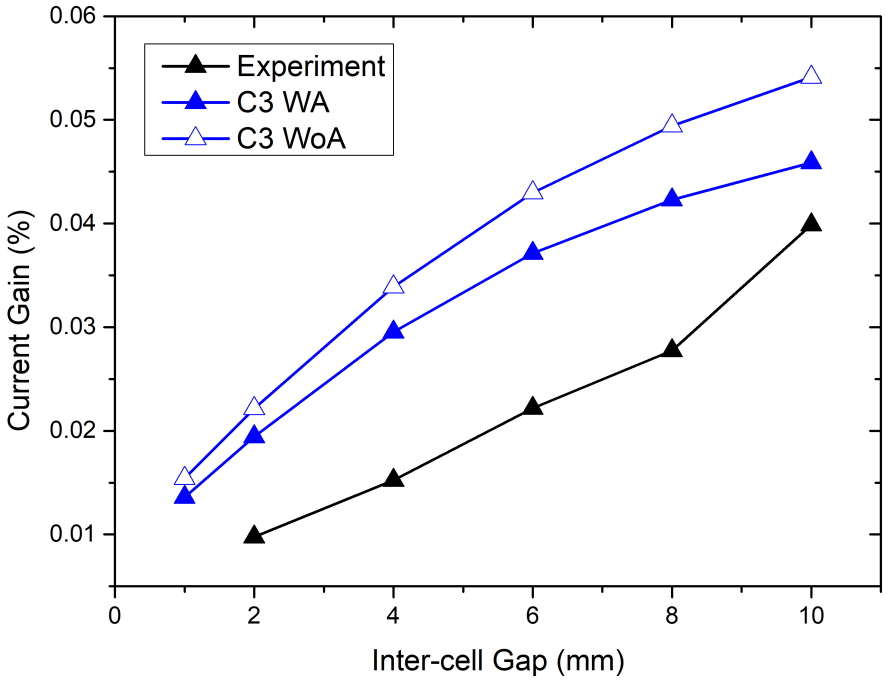

Figure 3.17: Comparison of current gain of experiment and simulation showing the same trend with the increase of inter-cell gap

3.3.3 Front Illumination Current Gain Comparison

After the verification of the model, simulation results of the three different bifacial module models done were plotted in Figures 3.18 and 3.19. Figure 3.18 illustrates the simulated current gains with and without consideration of absorption with varying inter-cell gap of the three different bifacial module structure with reflective layer configuration, as illustrated in Figures 3.2, 3.3, and 3.4. The increase of current gain with increasing inter-cell gap distance with reflective layer are consistent with reported studies from Jai et al. [8], Su et al. [59] and Juang et.al [60]. From Figure 3.18, the current gain reduces from Configuration 1 to Configuration 3. The difference between the three configurations is due to the distance between the reflective layer to the cell.

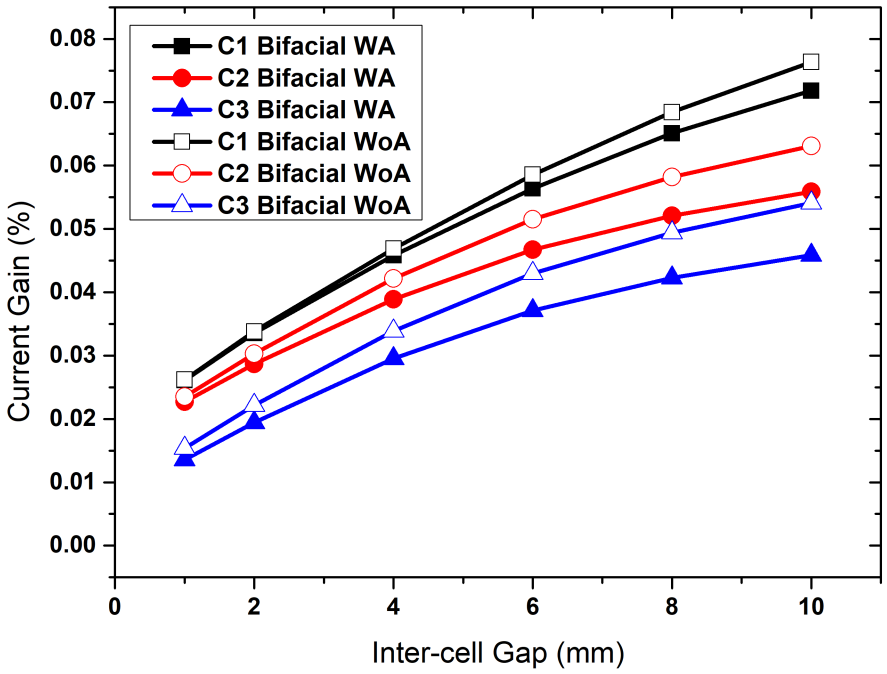

Figure 3.18: Current gain of bifacial modules for three configurations (C1, C2, C3) with (WA) and without (WoA) absorption

The additional distance between the reflective layer and the cell increases the number of rays being reflected onto the cell. In the illustration of all the bifacial modules configuration cross section, the distance travelled by the rays absorbed on the front side is twice as compared to those absorbed by the rear. As discussed in the previous section, McIntosh et al. reported that the increase in the light rays travelled distance increases its absorption losses [58]. In Figure 3.18, the difference between the current gain with and without consideration of absorption loss could be used to explain the contributions of front and rear to the current gain. Similarly, this is seen in Figure 3.19 where the current gain is breakdown into front and rear.

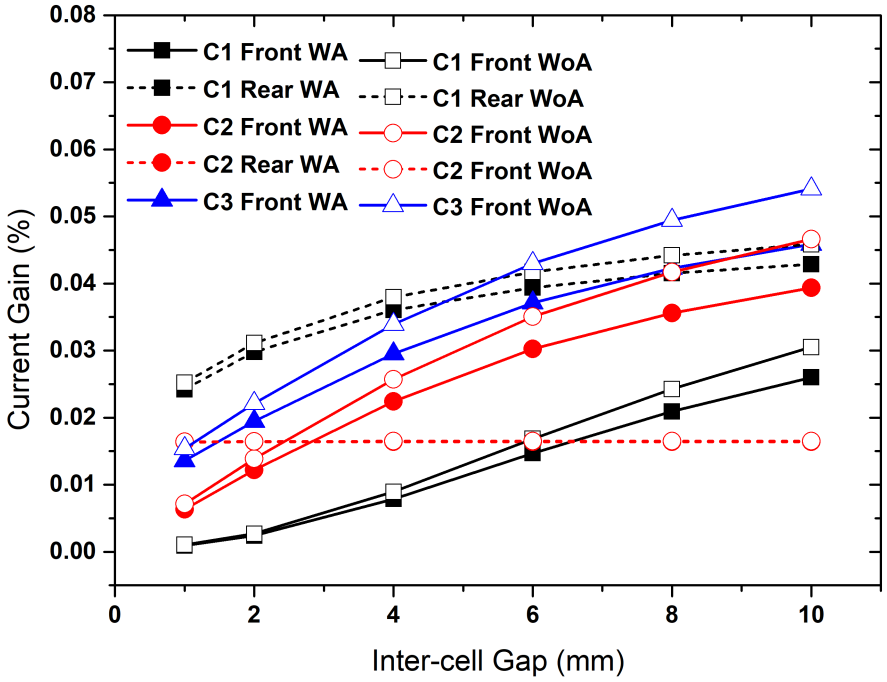

Figure 3.19: Rear and front current gain of bifacial modules for three configurations (C1, C2, C3) with (WA) and without (WoA) absorption

Configuration 3 has no contribution from the rear as the reflective layer is on the same plane as the cell, whereas Configuration 2 has minimum rear contribution with increasing cell gap as most light rays are reflected towards the front glass as compared to Configuration 1. For the inter-cell gap of 1mm to 10mm, Configuration 1 has the highest current gain of the three configurations. Configuration 1 has the highest rear current gain from the rear surpassing Configuration 2 rear current across 1mm to 10mm. Configuration 1 rear current gain exceeds Configuration 2 and 3's front current gain. A higher current gain could be achieved for Configuration 1, if the bifaciality factor of the cell is improved. Currently, a bifaciality factor of 0.8 was used for this model.

3.3.4 Rear Illumination Current Gain Comparison

While Configuration 1 has the highest current gain for front side illumination, there would be little or no current gain from rear illumination, as all the light rays that are incident on the inter-cell gap are reflected out of the module. With Configuration 2 and 3, there would be light rays reflected to the rear of the cell, as illustrated in Figures 3.20a and 3.20b respectively.

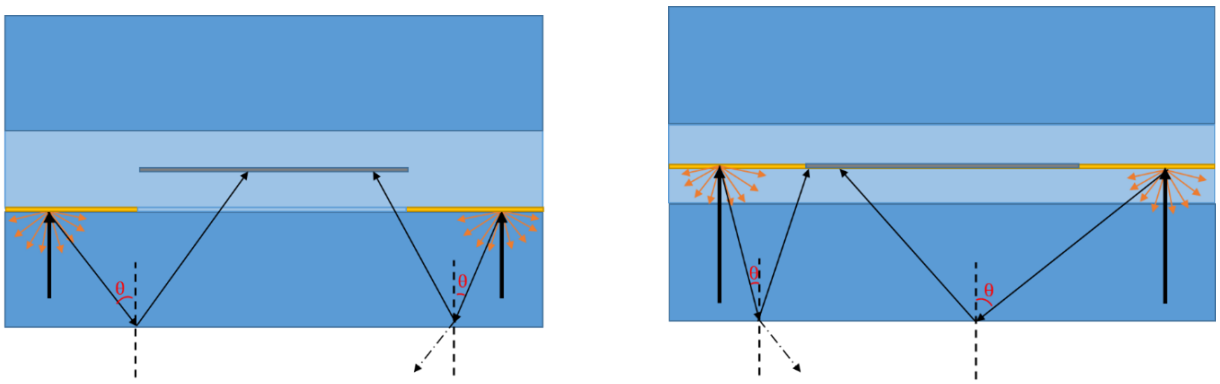

(a) Configuration 2 rear illumination

(b) Configuration 3 rear illumination

Figure 3.20: Rear illumination rays paths illustration for Configuration 2 and 3

Plotted on Figure 3.21 are the simulated current gain with rear illumination with Configurations 2 and 3. As the reflective layer distance from the cell between the two configurations is not significantly different as illustrated in 3.20, the resultant current gain is comparatively close.

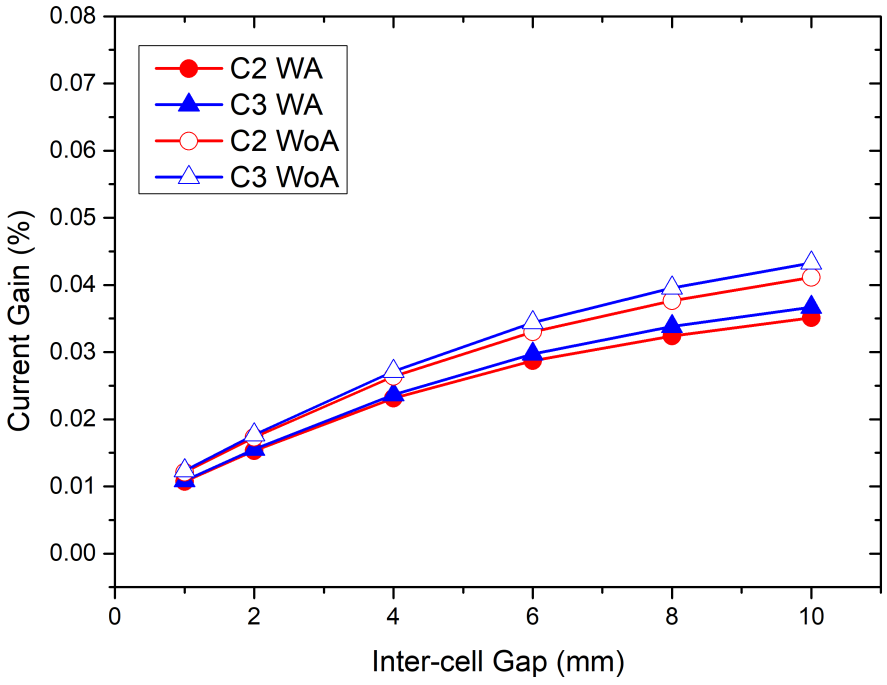

Figure 3.21: Current gain from rear illumination for bifacial modules of Configuration 2 (C2) and 3 (C3) with (WA) and without (WoA) absorption

From the results discussed previously, Configuration 1 has the highest current gain during indoor flash tests with front-side illumination at standard testing conditions. A bifacial module is illuminated on both sides during outdoor energy yield. Therefore, the three bifacial module

configurations are simulated for both-sided illuminations. Adding on the results of the front side and rear side illumination current gain, Configurations 2 and 3 surpass Configuration 1 in current gain. The front and rear current gain for Configuration 2 results in the highest current gain across a 1 mm to 10 mm inter-cell gap distance. This illustrates the disparity between indoor and outdoor performance for the different module configurations.

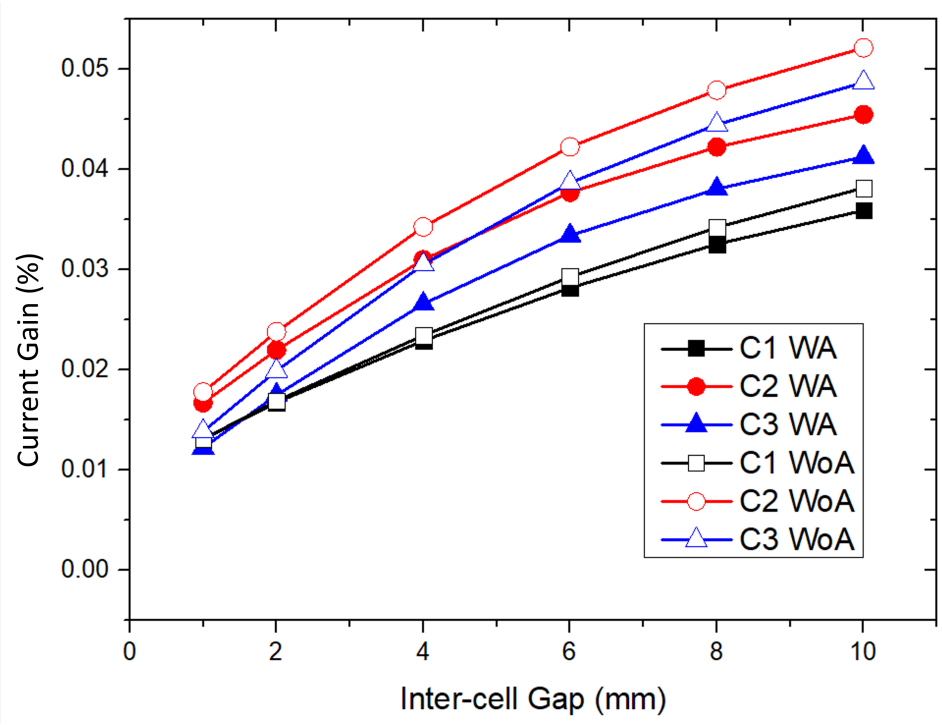

Figure 3.22: Current gain from both-sided illumination for bifacial modules for three configurations (C1, C2, C3) with (WA) and without (WoA) absorption

3.3.5 Double Sided Illumination Comparison

In monofacial modules, reflective rear encapsulants are on the same plane as the cells, to reduce absorption losses as the light rays are reflected on the same plane as the cell. Additionally, this removes the possibility of rays being reflected onto the inactive rear of a monofacial cell. In Figure 3.23, the three configurations were compared. From Figure 3.23, Configuration 3 has the highest gain for monofacial cells unlike bifacial cells, monofacial solar cells are unable to absorb irradiance on the rear. As a result, only rays that reach the front of the cell would contribute to the current gain. In Configurations 2 and 3, the majority of the reflected rays reach the rear of the cell. In Configuration 1, all rays are reflected to the front of the cells, thus the difference in performance between bifacial and monofacial cells.

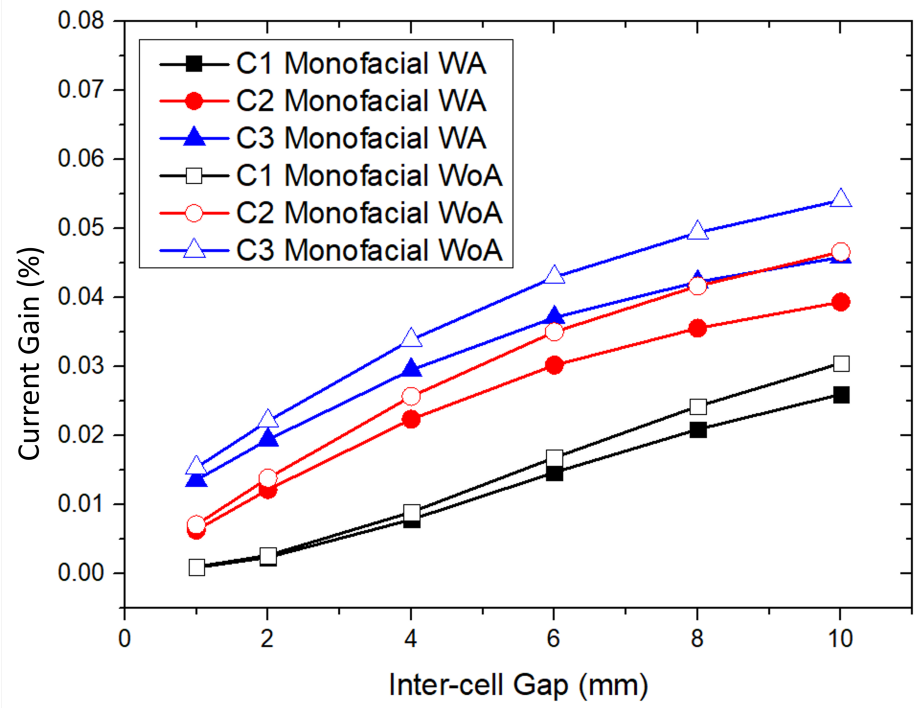

Figure 3.23: Current gain of monofacial modules for three configurations (C1, C2, C3) with (WA) and without (WoA) absorption

To compare the reflective layers' effect on both monofacial and bifacial modules during pseudo-outdoor conditions, a two-sided illumination was used to simulate the current gain for monofacial modules plotted in 3.24. As reported in the previous sections, bifacial modules perform better as compared to the monofacial modules. While Configuration 2 has the highest current gain across a 1 mm to 10 mm inter-cell gap, Configuration 1 and 3 has little different at a typical 2 mm inter-cell gap. The outdoor energy yield of the bifacial module would exceed monofacial modules as shown in 3.24 where all the bifacial modules (solid lines) have almost twice the monofacial modules (dash lines). However, the outdoor performance is not as distant within the bifacial modules with the three configurations.

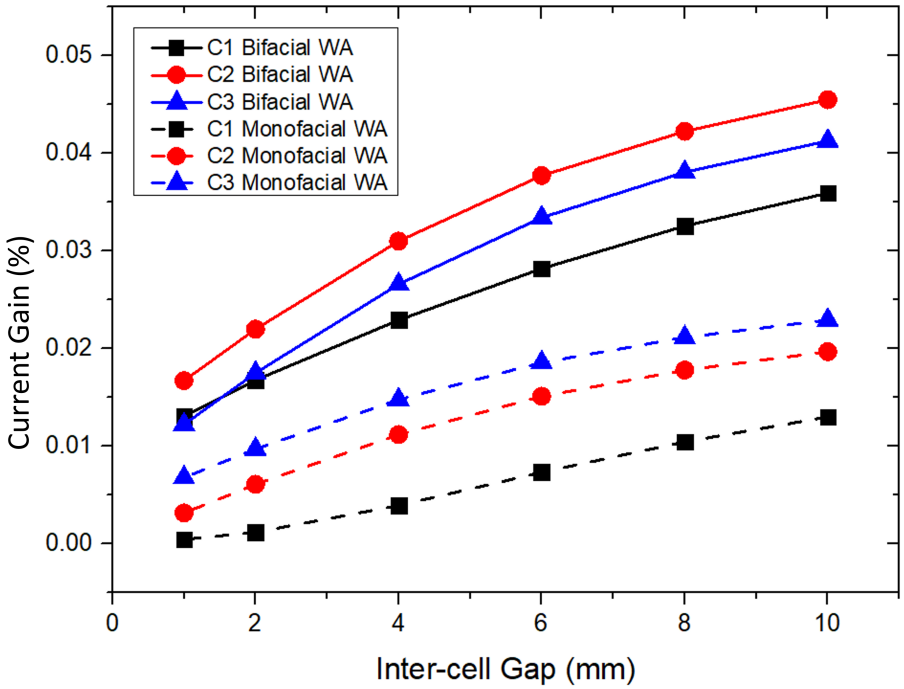

Figure 3.24: Current gain for monofacial and bifacial modules with both-sided illumination for three configurations (C1, C2, C3) with (WA) absorption

3.4 Summary

Traditionally, the implementation of new technology has always been associated with an increase in cost. For PV manufacturers to achieve the grid parity goal, new technology implemented had to be cost-effective and reliable. By inserting the reflective layer in the inter-cell gap of bifacial modules additional power gain can be achieved. This chapter discussed the three different configurations of bifacial modules with reflective areas between the inter-cell spacing to enhance the power and current of current bifacial modules. The three configurations differ in the relative location of the reflective layer to the cell. In addition to the optical ray trace model, a numerical model considering absorption losses was developed for three different module configurations.

The optical ray trace model for the three configurations was created with inputs from test measurements. The simulation of the three numerical models created takes into consideration absorption loss to simulate the current gain from each configuration with varying inter-cell spacing. The corresponding performance gain was evaluated for models with and without absorption loss. The simulation result was validated with experiment results for Configuration 3 where the RMSE reduces from 0.018 to 0.012 with the consideration of absorption losses. To further reduce the RMSE, additional transmission and reflection losses could be considered in the numerical model for better accuracy.

As the bifacial module will be exposed to both front and rear side illumination, three different illumination conditions were considered in the simulation namely, the front illumination, rear illumination, and illumination from both sides. In addition, the performance between the bifacial and monofacial configurations has been investigated to evaluate the performance in terms of the total current obtained. For front-side illumination, it has been shown that Configuration 1 has the highest current gain of 3.4%. In comparison, for the monofacial module group, Configuration 3 has the highest current gain at 1.9% with front-side illumination, which is half of the bifacial modules. For the rear illumination, Configuration 2 and 3 have comparable gain while Configuration 1 has no additional gain as the reflective layer reflects the rays out of the module. In the outdoor energy yield setting, the modules are illuminated on both sides, resulting in the change in current gain for bifacial module Configuration 1 to 1.7%, Configuration 2 to 2.2%, and Configuration 3 to 1.8%. In addition, the simulation results show that most of the current gain for bifacial modules with a 2 mm inter-cell gap comes from the rear of the cell from a front side illumination. The simulation results demonstrated that the bifacial module has a higher current gain from the reflective layer in the inter-cell gap across three illumination conditions, as compared to monofacial modules.

Chapter 4

Simulation and material optimisation analysis for bifacial modules with variable tilt

In Chapter 3, the optical ray trace model for three different module configurations is developed with consideration of absorption losses. In this chapter, Section 4.1 considers varying tilt angles in the ray tracing numerical model in MATLAB where different mounting set-ups for Type 0 and Type 1 bifacial module configurations are modelled to evaluate the module configuration current gain from the reflected ground irradiance across the day. Section 4.2 discusses the simulation results on the current gain with varying glass thickness and different tilt angles.

The indoor flash test results of the Type 0 and Type 1 bifacial modules illustrating their differences are shown in Section 4.3. The simulation results are verified through experimental data that was obtained using Type 0 and Type 1 bifacial modules in USA and a Type 1 module in Singapore, which are described in Section 4.4. This is followed by the experimental results from the outdoor sites in Section 4.5. A summary is presented in Section 4.6.

4.1 Methodology of Simulation

The main parameter that dominates the losses of bifacial, as compared to monofacial module under standard testing conditions, is the module output current. Therefore, ray tracing was used to model the bifacial module materials and configurations that contribute to the module current gain in MATLAB. The base model for simulation of the current gain from the inter-cell gap reflective layer and mounting configuration that was reported in the previous chapter, was presented at the European Photovoltaic Solar Energy Conference and Exhibition in September 2018 [86].

4.1.1 Mounting Configurations

Unlike indoor STC where the modules are placed perpendicular to the illumination source, outdoor conditions modules are mounted at an angle that is approximate to the location latitude. Other than the mounting angle, the module mounting height and ground reflectance also impact its outdoor performance [87]. In this chapter, the numerical model in Chapter 3 considering absorption losses, is built upon to simulate the current gain from each configuration with varying inter-cell spacing [86], to study the effects from varying mounting tilt angles.

Firstly, assumptions of the material properties of air, glass, and encapsulants were made for the simulation. The glass and encapsulants were assumed to be the same and the optical losses between them were minimal. The glass and encapsulant refractive index is assumed to be 1.5 while air to be 1 [19] [84]. Secondly, the ground coating results in a totally diffused reflected irradiance from the incoming irradiance. The reflected unpolarised rays are scattered uniformly into 3600 rays in both the azimuth and polar direction at 3° and 6° respectively. Lastly, all rays were assumed to consist of parallel and perpendicular components.

Additional assumptions made for this new proposed model are as follows. Firstly, the modules only tilt on a single axis centered on the middle of the middle cell in the polar direction. Secondary, irradiance that was transmitted out from the rear glass would not be reflected onto the cell. Lastly, a tilt angle of full vertical 90° could not be simulated with this model as there is zero direct irradiance on the cell. In addition, the Type 0 bifacial module has no current gain due to the absence of a reflective layer in the inter-cell gap, resulting in no additional influence of tilt angle on the current gain.

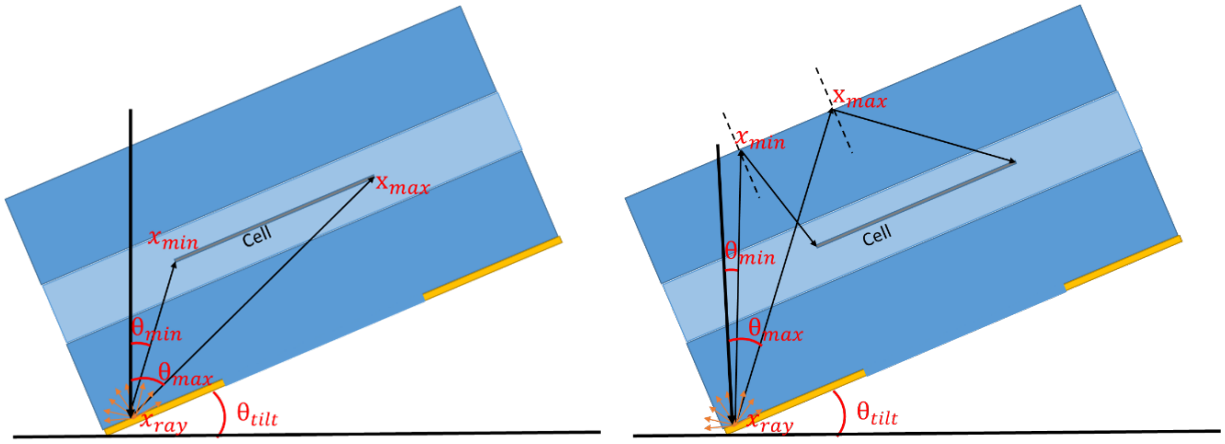

(a) Rays' path to the rear of cell with the maximum and minimum angles for the rays

(b) Rays' path to the front of cell via reflecting back from the front glass / air interface

Figure 4.1: Internally reflected rays path of Type 1 bifacial module from origin to rear or front of cell

An illustration of the rear and front rays' paths of a Type 1 bifacial module with tilt is shown in Figures 4.1a and 4.1b respectively. The calculation of minimum and maximum polar angles that could be reflected onto the rear and front of the cell were calculated using Equations 4.1 and 4.2, where x_{ray} is the coordinate of the incoming ray, x_{min} and x_{max} are the coordinates of the boundaries where the light rays can be reflected onto the cell and θ_{tilt} is the mounting tilt angle.

$$\theta_{min} = cos^{-1}[\frac{x_{ray} \times x_{min}}{|x_{ray}| \times |x_{min}|}] \times \cos(\theta_{tilt}) \tag{4.1}$$

$$\theta_{max} = cos^{-1}[\frac{x_{ray} \times x_{max}}{|x_{ray}| \times |x_{max}|}] \times \cos(\theta_{tilt}), \tag{4.2}$$

To compute θ_{min} and θ_{max} range for rays that were reflected to the rear of the cell in Figure 4.1a, x_{min} and x_{max} are the reflected ray coordinates to the nearest and furthest point of the cell, with respect to the ray initial position. For the front side of the cell in Figure 4.1b, x_{min} and x_{max} are the nearest and furthest position on the front glass where the reflected rays are able to reach the front side of the cell.

For computing the total additional radiant power, $S(\theta)$ that is reflected onto the cell, additional checks for the minimum and maximum polar angles were updated to those binary output functions of T1 in Equations 3.6 and 3.7. The resulting binary output functions, with an additional function of polar angle, $T1(x_2, y_2, \theta_1)$ and $T1(x_3, y_3, \theta_2)$ are checked if the light rays final positions are on the cell and within the minimum and maximum angles. These are applied in Equations 4.3 and 4.4 for the summation of rays that contribute to the rear and front power respectively.

$$P_r = \int_{q_1}^{q2} \int_{p_1}^{p_2} \int_0^{\pi} \int_{\alpha}^{\frac{\pi}{2}} S(\theta) \times T1(x_2, y_2, \theta_1) \times R_g d\theta d\varphi dx, dy \tag{4.3}$$

$$P_f = \int_{q_1}^{q2} \int_{p_1}^{p_2} \int_0^{\pi} \int_0^{\alpha} S(\theta) \times T1(x_3, y_3, \theta_2) \times R_g d\theta d\varphi dx dy \tag{4.4}$$

4.2 Results And Discussion For Modelling And Simulation

In this section, a parametric study on the module front glass thickness was conducted via MATLAB to investigate the effect on the overall performance of the Type 1 bifacial module configurations at zero-degree tilt angle. Following this, the effect of tilt angles from 0° to 67.5° on Type 1 bifacial module configurations current gains would be discussed and the optimal tilt angle for this configuration would be recommended. The assumptions and input parameters into the MATLAB model are a continuation of Section 3.2 with the additional tilt and material optimisation function.

4.2.1 Simulation Results On Module Material optimisation

In this section, the front glass thickness optimisation was chosen as it takes up most of the module cross-sectional thickness, as compared to the encapsulants. Figure 4.2 presents the results when front glass thickness was varied from 2 mm to 10 mm with varying inter-cell gap from 2 mm to 20 mm.

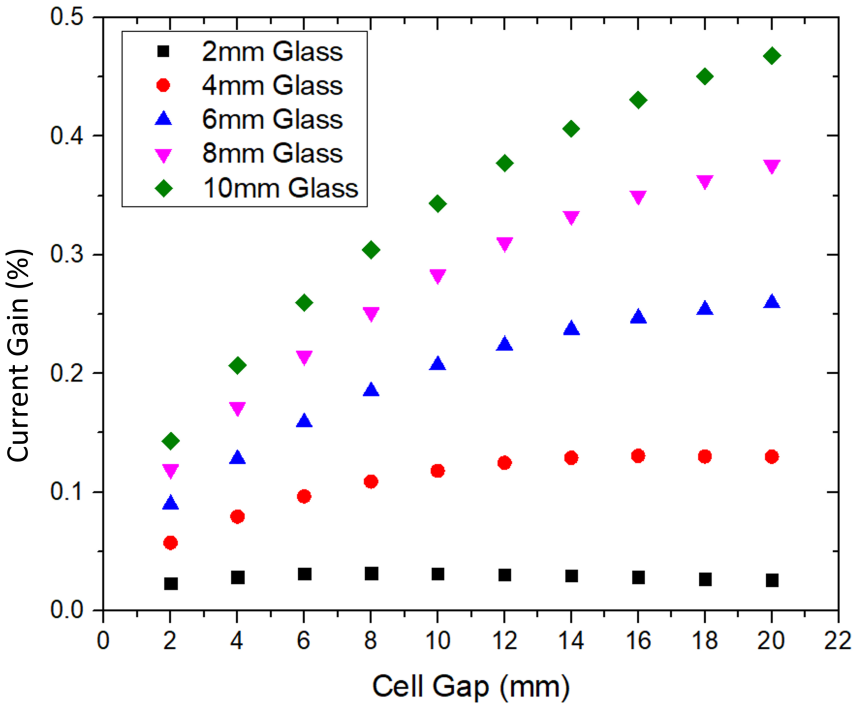

Figure 4.2: Current gain from cell gap and glass thickness from 2mm to 10mm illustrating the increase of current gain from the additional rays that were reflected back to the cell with increasing thickness

From Figure 4.2, it is shown that the current gain of the Type 1 bifacial module increases as the front glass thickness increases across all inter-cell gaps. This effect from the increase in glass thickness was compounded with the increase in inter-cell gap. As discussed previously, the Type 1 module with various glass thicknesses has a reduction in the number of rays reflected onto the cell front and rear as the inter-cell gap increases. From this simulation, the compounding effect in current gain was from the larger number of rays being reflected to the front of the cell due to the increase in glass thickness. As illustrated in Figure 4.3, the increase in glass thickness has little effect on the reflected rays that are close to the cell, as shown on the right of the figure. There is only a small range of angles where reflected rays can fall into the cell. To the reflected rays shown on the left in Figure 4.3, which are further away from the cell, this increase in glass thickness resulted in a larger range of angles where reflected rays fall into the cell, which in turn increased the current.

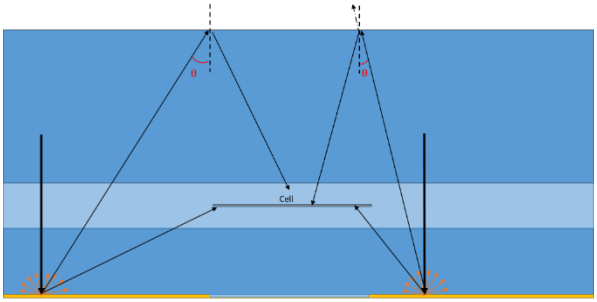

Figure 4.3: Type 1 module with thicker front glass and larger cell gap illustrating the increase of current gain from more rays being reflected back to the cell front or rear

Figure 4.4 illustrates the results on the current gain of a Type 1 bifacial module of 2 mm inter-cell gap with four tilt angles, 0°, 22.5°, 45°, and 67.5°, across varying front glass thickness. From the simulation, the current gain increases as the module tilts towards 45° and reduces as it crosses over towards 90°. It has been shown previously, that a significant amount of current gain at a 2 mm cell gap is from rays reflected to the rear of the cell. This increase in current gain agrees with the former that the increase in tilt angle from 0° to 45° increases the number of rays that were reflected toward the rear of the cell, as shown in Figure 4.3. As the angle increases from 45° towards 90°, the inter-cell gap would be shaded by the cell. This results when the reflective inter-cell gap is less than the thickness of the rear glass and encapsulant on the lower side, as illustrated in Figure 4.5.

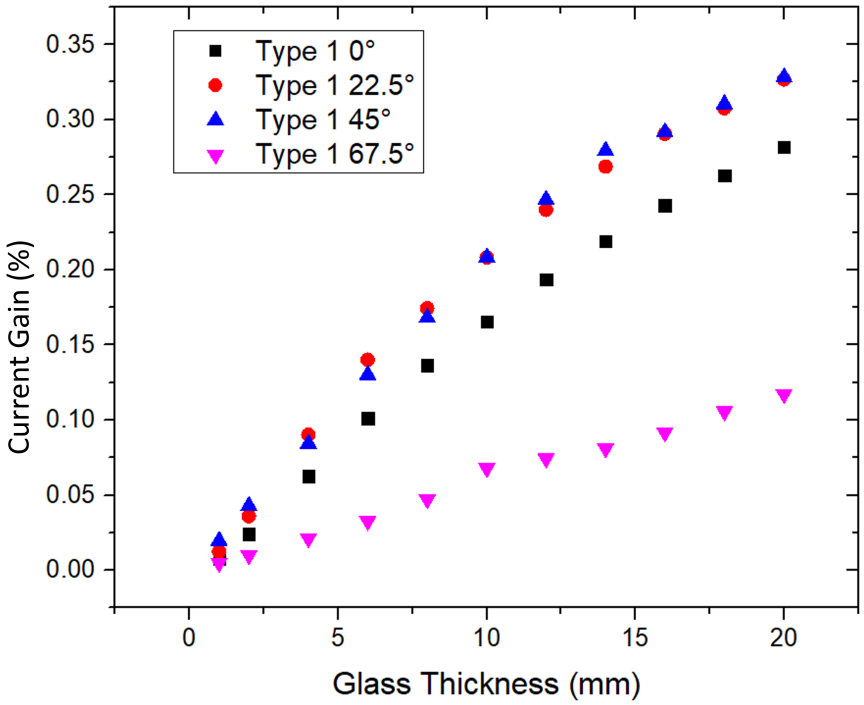

Figure 4.4: Type 1 current gain with varying front glass thickness illustrating the increase before self-shading occurs which reduces the current gain

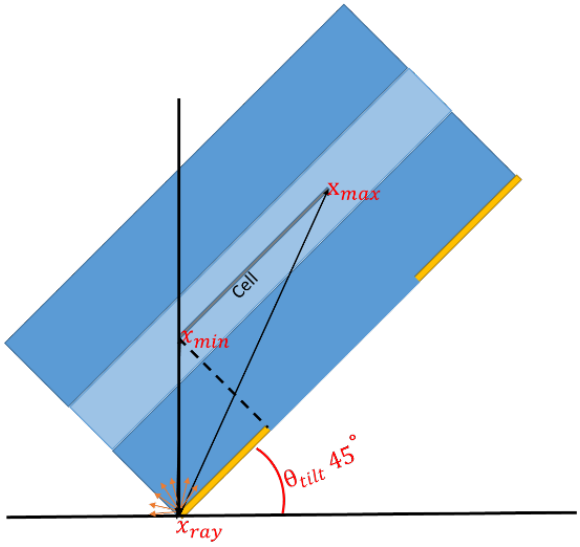

Figure 4.5: Type 1 tilt more than 45° visualising the self-shading of reflective coating area at the cell gap by the cell itself

4.2.2 Simulation Results On Module Tilt

As discussed in Section 4.2.1, the increase of front glass thickness allows a larger range of angles and the number of rays that could be reflected onto the cell. This phenomenon was also seen with an increase in tilt angle from 0° to 45° where the current gain from both tilt angle and glass thickness increases the number of rays hitting the cell.

Using the ray tracing model presented above, the tilt angle of 0°, 22.5°, 45°, and 67.5° were chosen to study the influence of tilt angle on Type 1 bifacial module. From the simulation, Type 1 bifacial module current gain increases to 4.3% at a tilt angle of 45°, as compared to 2.4% in 0° mounting, as plotted in Figure 4.6. As the module tilts towards 45°, this provides a maximum increase of 79% in current gain, as compared to 0°. This increase in current gain reduces as the tilt angle goes beyond 45° towards 67.5°, as shown in Figure 4.6. A full vertical module of 90° could not be simulated in the model. Thus, the postulation of reducing current gain in Type 1 bifacial module beyond 45° towards 67.5° could be extrapolated to 90°, which has 0% current gain from the assumption discussed earlier.

It has been discussed in Chapter 3 that a significant amount of current gain is contributed by rays reflected to the rear of the cell from the reflective layers next to the cell at the inter-cell gaps. It was also reported that the current gain reduces exponentially with the increase in inter-cell gap [86]. As illustrated in Figure 4.1a, the increase in tilt angle from 0° to 45° increases the number of rays that could be reflected toward the rear of the cell rather than towards the front glass, which could be lost as front transmission losses, Hence, the increase in current gain comes with the increase of tilt angle is the result of the increase of rays reflected onto the rear of

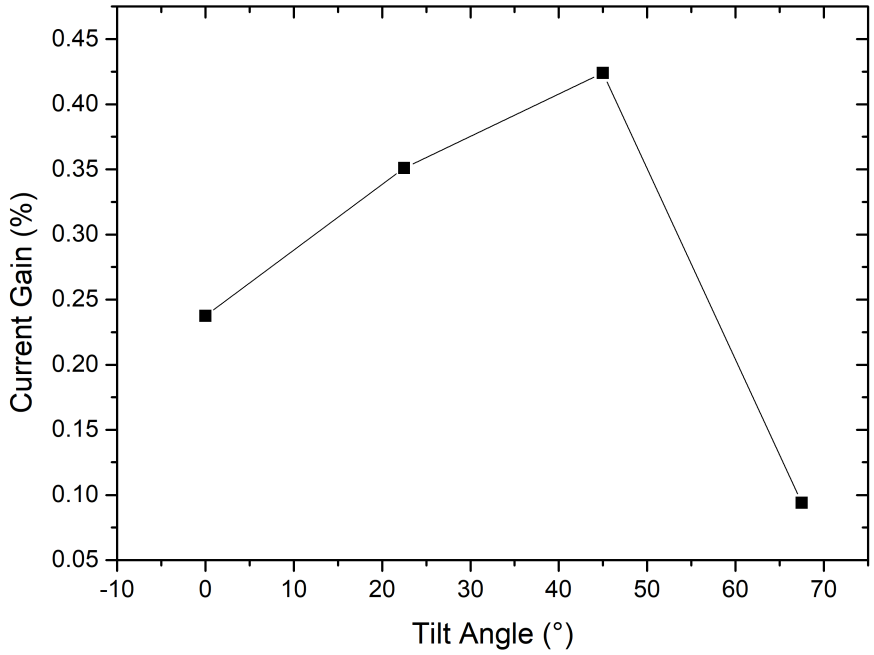

Figure 4.6: Type 1 fabricated module of 2mm cell gap current gain to tilt angle

the bifacial cell.

The decrease in current gain beyond 45° shows a self-shading effect where the cell shades the incoming irradiance from reaching the reflective layer at the inter-cell gap. Thus, even with the increase in rays being reflected to the rear of the cells, the shaded inactive reflective layer at the inter-cell gap reduces the net current gain of the Type 1 bifacial module. With the increase of tilt angle beyond 45°, the distance of the active reflective layer from the cell increases. The magnitude of the self-shading effect is the function of the encapsulant material thickness, which changed the distance of the reflective layer position to the rear of the cell, as illustrated in Figure 4.5 dotted line, with the vertical line that illustrates incoming rays that is perpendicular to the ground.

The investigation of front glass thickness and the effect of tilt angle for optimal current gain of Type 1 bifacial modules points towards thicker front glass and a tilt around 45°. While manufacturers are moving towards cost competitiveness by reducing material thickness, this gain could be realised by building integrated photovoltaics where the cells are enclosed in glass roofs or windows.

4.3 Indoor Flash Test Results

STC tests and measurements procedural for the photovoltaics modules discussed were conducted on the fabricated modules for outdoor monitoring. These modules were tested under Standard Test Condition (STC) of AM1.5G spectrum in PASAN Solar Modules Sun Simulator for the front and rear side power.

Table 4.1: Comparison of indoor flash test results for Type 0 and Type 1 bifacial modules and monofacial modules fabricated

Module Type	Bifacial Ratio	Side	P_{mpp} (W)	I_{sc} (A)	V_{oc} (V)	V_{mpp} (V)	I_{mpp} (A)	FF (%)
p-PERC Type 0	68%	Front	328.6	9.25	46.5	37.9	8.66	76.37
p-PERC Type 0	68%	Rear	223.3	6.23	45.7	38.4	5.82	78.36
n-PERT Type 0	84%	Front	355.3	9.69	46.6	38.9	9.07	78.18
n-PERT Type 0	84%	Rear	299.5	8.26	46.3	39.1	7.67	78.29
p-PERC Type 1	56%	Front	335.8	9.52	46.5	37.4	8.98	75.92
p-PERC Type 1	56%	Rear	188.4	5.42	45.4	39.3	4.79	76.51
n-PERT Type 1	72%	Front	360.7	9.91	46.7	38.7	9.32	77.97
n-PERT Type 1	72%	Rear	260.0	7.18	46.1	40.6	6.40	78.51
p-PERC Mono-facial		Front	340.0	9.52	46.3	38.5	8.84	77.21

Due to the high open circuit voltage (Voc) of the modules, the capacitance effect affects the voltage-current sweep measurement, resulting in lower module-rated conversion efficiency from

the underestimation of Fill Factor (FF) of the module during measurements [88]. To overcome this capacitance effect, either a longer measurement time or discharging algorithm is commonly used [89]. The measurement results from monofacial and bifacial Type 0 and Type 1 are presented in Table 4.1, which are measured with discharging algorithms [90].

Table 4.1 presents the impact of material and cell structure on the bifacial ratio from the indoor flash test results. The multi-crystalline p-PERC Type 0 bifacial module has a bifacial ratio of 67%, as compared to the mono-crystalline n-PERC Type 0 bifacial module of 85%, which is a reduction of 79% in bifacial ratio. This is due to an inherent bulk material limitation of multi-crystalline, which results in a lower cell quality and a lower open circuit voltage and current collection from both the front and rear. While multi-crystalline wafers are generally of a low bulk quality, the lower cost of producing such wafers makes them attractive. This is further compounded by the structural differences in the Back-Surface Field of the p-PERC and n-PERC cell technology, which resulted in a drop in the bifacial ratio. Similar results were observed for p-PERC and n-PERC Type 1 module configurations.

In Chapter 3, there is a 3.4% current gain for Type 1 bifacial modules with a 2 mm cell gap, as compared to a Type 0 bifacial module [14]. From the indoor flash test results in Table 4.1, the current gain measured for Type 1, as compared to Type 0, in p-PERC and n-PERT cell structures are 2.9% and 2.2% respectively, which is close to our simulation result in Chapter 3. Comparing p-PERC Type 0 bifacial and monofacial modules, Type 0 bifacial modules have 3% lower current due to rear transmission losses. With a reflective inter-cell gap in Type 1 bifacial modules, transmission loss was reduced, and the current is comparable between monofacial and bifacial modules in indoor flash tests. The rear side current has a similar 14% drop for both cell structures between Type 1 to Type 0. This could be attributed to the encroachment of reflective coating in the inter-cell gap during the fabrication of glass.

4.4 Outdoor Energy Yield Test Setups

In this section, the outdoor energy yield setups are described and the outdoor monitoring results between bifacial modules with (Type 1) and without reflective inter-cell gap (Type 0), and monofacial energy yield comparison are presented. The modules were fabricated, shipped, and tested in two different outdoor test sites for energy yield comparison. The first site was situated in Singapore and the second site is in a REC America collaboration site in California, USA. The interplay of mounting orientation, height, and tilt angle shown in Figure 4.7 are the main factors studied for their impact on the module energy yield [12].

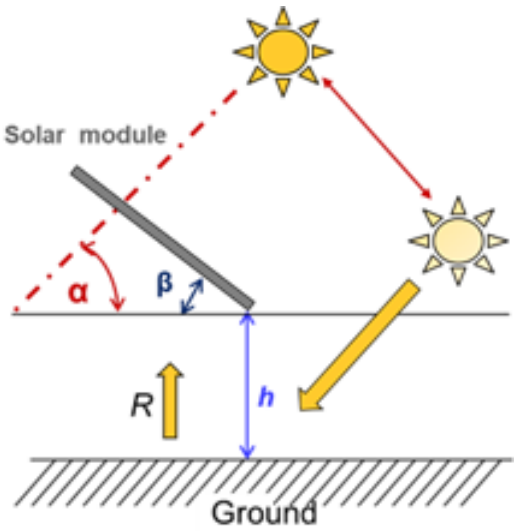

Figure 4.7: Schematics of mounting configuration with ground reflectance (R), height of module (h), tilt angle (β)

For the test site in California, America, Type 1, Type 0, and monofacial modules were mounted 1m above sand gravel. The maximum power point tracker and temperature sensors were shared with other set-ups at this test site. To achieve a zero-degree tilt angle, the modules must be perpendicular to the incoming irradiance of the sun at all times. The modules in this test site were mounted on a single-axis sun tracker from NexTracker, which tilts the rack as the sun moves across the sky. This test site mainly compares the long-term energy yield at zero-degree tilt from the different cell and module configurations and in comparison, to the monofacial baseline modules. This site compares the whole array of PV modules mounted on a sun tracker without individual irradiance being logged per module and the energy yield calculation used was the generated energy (Wh) normalized by the rated peak wattage that the module was rated for (Wp).

For the second test site in Singapore, a Type 1 n-type 60-cells bifacial module with a 90% bifacial ratio of Type 0 glass/glass configuration was mounted on a movable and tilt-able rack at 1m above the ground in an East-West facing. Gravel and sand surrounding the modules have a measured ground reflectance of approximately 20% via irradiance sensors mounted parallel to the ground at 0.6m, as shown in Figure 4.8. The set-up was positioned in an existing solar test bed with other solar module arrays with minimal shading from neighbouring buildings after 1500 hours in the fourth quarter of the year. The test module was connected to a Tristar Maximum Power Point Tracker (MPPT) solar charge controller with energy storage in a lead acid battery with a discharge load. Two silicon-cell pyranometers were used to log the real-time solar irradiance and reflected ground irradiance separately. The modules have an area of 1.6 m^2 with both configurations having a cell-to-cell gap of 2 mm. With irradiance sensors mounted on the module frame, a comparison of the energy conversion efficiency of the module could be done at

varying tilt angles with the real-time recording of irradiance and ground reflectance across a day.

The comparison of the different configurations was done on the same bifacial module with varying white reflective layers on the rear of the module. Shown in Table 4.2 was the Type 0 bifacial module mounted in this site with a front conversion efficiency of 15.8% and a higher bifacial ratio 91%, as compared to those in the California test site, which was n-PERT Type 0 of 17.7% and 85% bifacial ratio. To improve the bifacial ratio, the cell processing of n-PERT cells was altered to allow higher transmission of light from the rear, thus reducing the internal reflectance of the cell. The optimisation of cell or module for bifacial application reduces the front side efficiency as the increase of rear illumination transmission reduces internal reflectance of front illumination. This test site predominately tests the effect of module configuration on the optimal mounting angles.

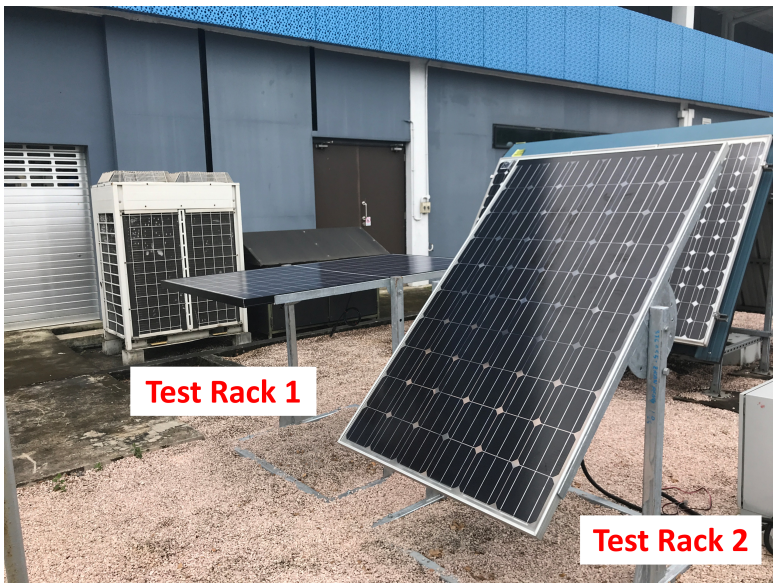

Figure 4.8: Outdoor site in Singapore with two variable tilting test racks with East-West configuration and 0.6m from gravel ground

Table 4.2: Indoor flash test results for Type 0 bifacial module used in Singapore site

Module Type	Bifacial Ratio	Side	P_{mpp} (W)	I_{sc} (A)	V_{oc} (V)	V_{mpp} (V)	I_{mpp} (A)	FF (%)
n-PERT Type 0	91%	Front	253.7	8.94	37.9	30.5	8.32	74.9
n-PERT Type 0	91%	Rear	226.9	8.18	37.6	31.4	7.24	73.7

4.5 Results And Discussion On Outdoor Tests

4.5.1 Zero-degree Tilt Mounting Configuration

Outdoor energy yield monitoring data of Type 0, Type 1, and monofacial modules mounted in California, America will be discussed in this section. A comparison of different bifacial module configurations at zero tilt angle enables the comparison between indoor STC flash test results from modules parallel to the illumination to actual outdoor energy yield performance when the modules are mounted on a tracker which keeps the module at zero tile angle to the sun.

The weekly energy yield of the p-type PERC Type 0 and 1 modules, the n-type PERT Type 0 and 1 modules, and the monofacial modules are plotted in Figure4.9. The performance of the bifacial modules across 18 weeks shows that p-type PERC Type 0 has a 1% higher energy yield on average, as compared to Type 1 modules. This additional energy yield is the result of the higher bifacial ratio of Type 0 modules, as compared to Type 1. Despite gaining 2.9% in current during the indoor STC flash test, the Type 1 module bifacial ratio was lower by 12% from the reflective inter-cell gap which negates the effect of front side current gain during outdoor energy yield.

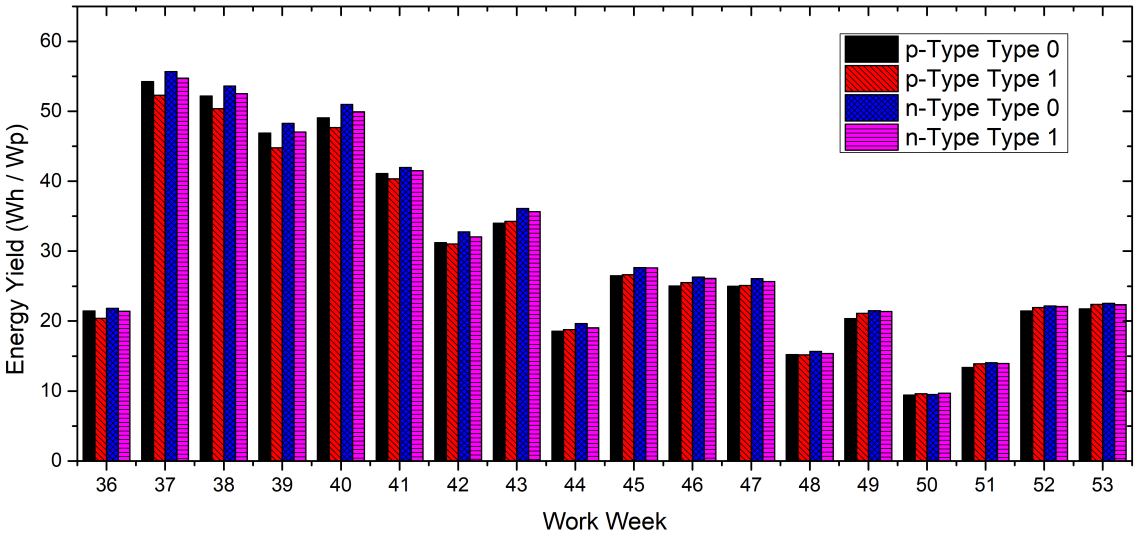

Figure 4.9: Weekly energy yield of four bifacial modules across the work weeks

With n-type PERT modules plotted in Figure 4.9, Type 0 bifacial modules of this cell type have an additional 1.5% energy yield across 18 weeks. Having both cell types of varying bifacial ratio demonstrating 1% to 2% additional energy yield in Type 0 modules, improvements to the bifacial ratio of modules would result in higher energy yield. Improvements to front-side rated power via a reflective coating, which complicates the manufacturing process alignment of cells

to the reflective layer at the inter-cell gaps, reduces the bifacial ratio of both cell types by 12% in bifacial ratio.

Subsequently, different cell types were compared for a similar bifacial module configuration. Type 0 bifacial modules with n-PERT cells have an additional 3.7% energy yield compared to p-PERC cells. This is due to the improved bifacial ratio of 85% of n-PERT, as compared to p-PERC of 67% injunction with better temperature coefficients for n-PERT modules. In Type 1 bifacial modules, the module with n-PERT cells has on average 3.2% higher energy yield, as compared to the module with p-PERC cells. As discussed above, the additional energy gain comes from the improvements in the bifacial ratio and temperature coefficient. The better temperature coefficient could be inferred from Table 4.1 of the higher Voc of n-PERT cells [38] indicating better quality cells, which are then encapsulated into modules that demonstrate better performance in both module configurations. From these comparisons, the bifacial modules' energy yield is a strong function of the cell bifacial ratio.

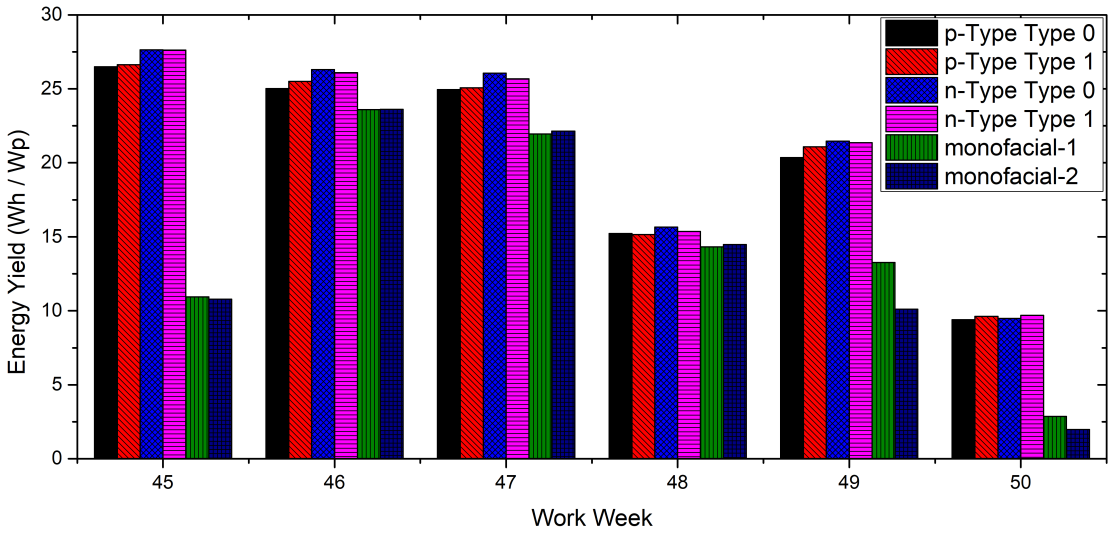

Figure 4.10: Bifacial energy yield comparison with monofacial module which was only inserted from work week 45 to 50

Monofacial modules were installed next to the bifacial modules for energy yield comparison. As shown in Figure 4.10, the energy yield of bifacial modules was 8% to 13% more than the monofacial modules. The gain in energy yield from bifacial modules as compared to monofacial modules, was more significant than the gain in having varying bifacial module configurations or cell types. This further supported the finding in the above discussion where the bifacial ratio was the dominant factor followed by its temperature coefficient in outdoor energy yield.

These outdoor energy yield monitoring data show the comparison of energy yield for bifacial modules with and without white coating. Type 1 bifacial modules were observed to have 1% to 2% lower energy yield, as compared to the Type 0 bifacial modules. This was discussed to be resulting from a 12% lower bifacial ratio for the Type 1 module, as compared to the Type 0 module. from the simulation results and the module power from the indoor STC flash test discussed above, the additional current gain was contributed by the reflective layer in the inter-cell gap. However, the contribution of this inter-cell gap reflective layer of 2.4% to 3.4% current gain was not transferred to outdoor energy yield.

4.5.2 Variable Tilt Mounting Configuration

The outdoor energy yield monitoring data of the Type 0 bifacial n-PERT module in Singapore, which was described in Table 4.2, will be discussed in this section. With irradiance sensors mounted on the module frame, a comparison could be done on tilt angle and the amount of irradiance or ground reflectance across a day that the module is receiving.

Figures 4.11, 4.12 and 4.13 illustrate the irradiance at the front and rear of the module at tilt angles of 0°, 45°, and 90° respectively. For 0° tilt angle, the rear irradiance (red dash line) is approximately 20% of front irradiance (black solid line), as shown in Figure 4.11. The ground reflectance of gravel sand was near 20% when measured with a handheld irradiance sensor. The dips in the irradiance resulted from cloud covers moving across the sky in the fourth quarter of the year in Singapore. A peak of 1000 W/m^2 is at solar noon when the sun is perpendicular to the module, which was around 13:00 hours in Singapore. The slight shading from neighbouring buildings could be seen in the drop of irradiance from 1500 hours till sunset from all tilt angles.

By tilting the modules to 45°, with an East-West facing direction the module would be of perpendicular to the sun at 1000 hours. This tilt resulted in the shift of peak front irradiance (black solid line) to earlier in the day and the drop of front irradiance at the original solar noon of 0° at 1300 hours, as shown in Figure 4.12. However, there is a slight increase in rear irradiance (red dash line) from 1300 hours to sunset from the increase in irradiance reflected from the ground into the rear of the module from the reduction in module self-shading. This ground reflectance increase would not be beneficial to monofacial modules.

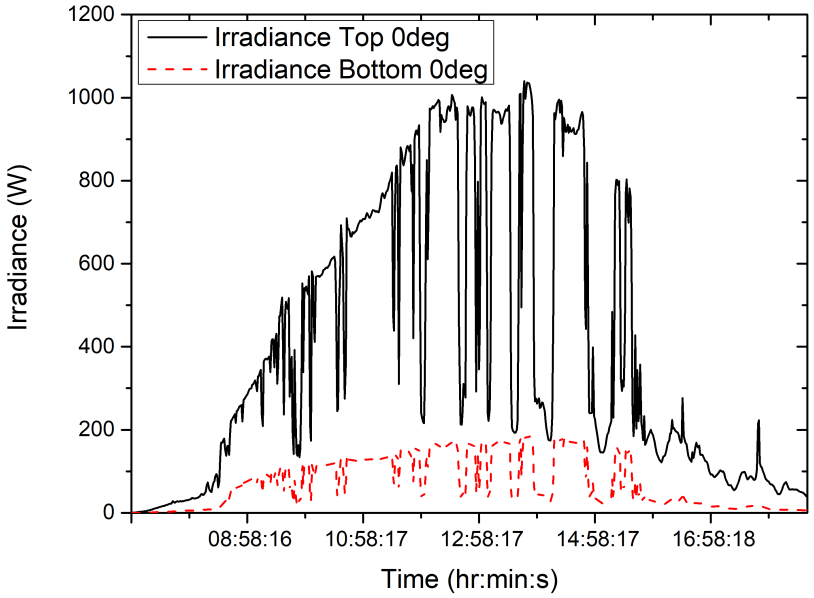

Figure 4.11: Irradiance sensors data 0° tilt angle for top and bottom

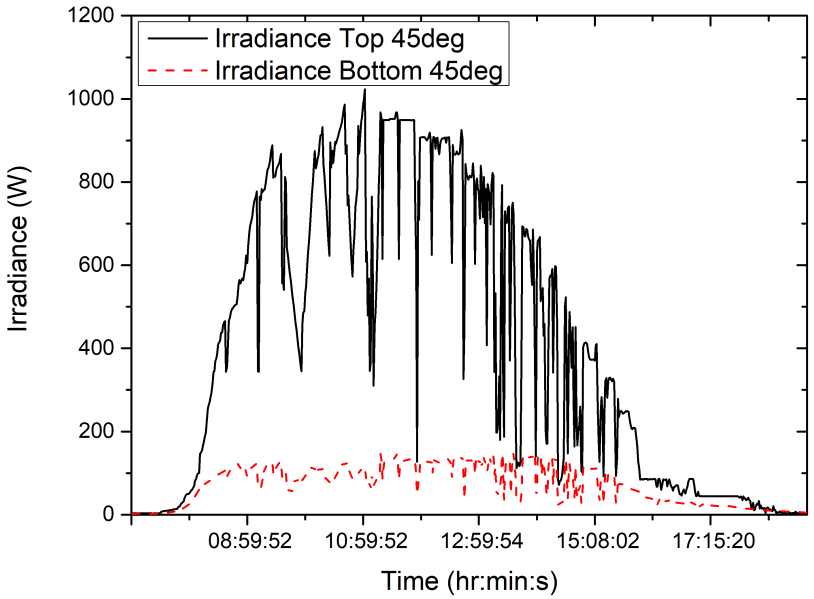

Figure 4.12: Irradiance sensors data 45° tilt angle for top and bottom

With a 90° vertical mounting, the module would be perpendicular to the sun twice a day. As plotted in Figure 4.13, the front irradiance peaks (black solid line) around 0930 hours and reduces till the original solar noon of 1300 hours when the front of the module no longer receives direct front irradiance. The rear irradiance (red dash line) increases from 1300 hours when direct irradiance received by the rear of the module starts to increase which peaks at 1600 hours before

sunsets.

The ability to manipulate energy yield profiles from different mounting configurations with bifacial modules allows the system designer to cater to different periods of peak energy usage from consumers [66]. The conversion efficiency of Type 0 and Type 1 bifacial module in 0°, 45° and 90° tilt angle was compared in Figure 4.14. The exact bifacial module was used for comparison between Type 0, Type 1, and monofacial by physically attaching a reflective backsheet at the rear of the Type 0 bifacial module. The calculation of conversion efficiency was done by taking the module output energy at the MPPT divided by the sum of energy input that was measured by the two mounted irradiance sensors. At 0° tilt angle, the Type 0 bifacial module outperforms the Type 1 bifacial module with reflective layers. This phenomenon was discussed in Section 4.5.1, where results from the first test site in America show Type 0 outperforming Type 1 bifacial modules. As discussed earlier, the Type 0 bifacial module would not see a rise in conversion efficiency when the tilt angle was increased to 45°, which is shown again in the experimental data. However, when mounted in full vertical 90° tilt angle, the conversion efficiency increased by 1.64% as compared to 0°. This shows the versatility of Type 0 bifacial modules in mounting conditions in the test site, where the mounting location is near the equator.

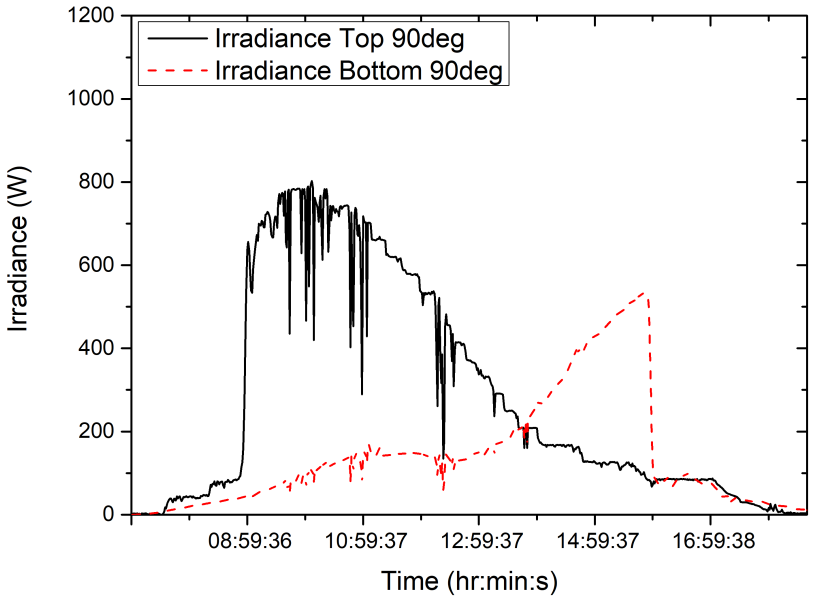

Figure 4.13: Irradiance sensors data 90° tilt angle for top and bottom

While the Type 1 bifacial module has shown an improvement in conversion efficiency when the tilt angle increased from 0° to 45°, it was significantly lesser as compared to the simulation model. Across all three different tilt angles, the Type 0 bifacial module has an average of 1.55% additional conversion efficiency, as compared to Type 1 bifacial modules with reflective layers. Although bifacial modules with reflective layer at the inter-cell gap have a significant current

gain from reported simulations and indoor flash test [7], [8], [86], which remove the transmission losses from Type 0 glass/glass bifacial modules as compared to monofacial modules, different mounting conditions and module design could result in varying performance during outdoor energy yield.

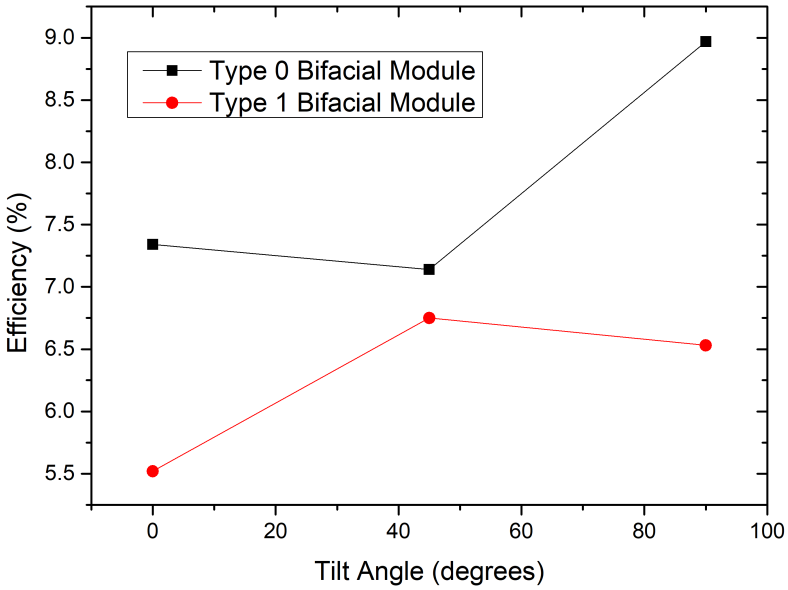

Figure 4.14: Module energy yield efficiency of Type 0 module

4.6 Summary

The internal ray tracing model for quantifying the contribution of internal reflection from the reflective layer in the bifacial module inter-cell gap during indoor flash test was further developed to estimate the bifacial module configurations' current gain with respect to the outdoor mounting configuration. The effect of tilt angle during indoor flash test shows that bifacial modules mounting configuration could be further optimised to collect additional solar irradiance, as compared to monofacial modules. While the module shows that Type 1 bifacial modules have the highest current gain at 3.4% in indoor front side illumination flash test, the best of the four bifacial modules configurations has a drop in current gain to 1.8% double side illumination flash test [86].

In this chapter, it has been shown that an increase in thickness of the front glass and an increase of tilt angle from 0° to 45° has a positive effect on the current gain. The increase of front glass thickness results in a larger angle of rays that could be reflected onto the cell and in conjunction with the increase of cell gap, there is potential to reach a 40% current gain at 20 mm

inter-cell gap with reflective material with 20 mm glass thickness. The simulation results show a current gain of 4.3% at a tilt angle of 45°, as compared to 2.4% in 0° mounting.

From the indoor STC flash test experiment, a 2% to 3% current gain was measured for Type 1, as compared to Type 0 module configuration. Comparing Type 0 bifacial and monofacial modules, the Type 0 bifacial module has a 3% lower current due to rear transmission losses. With reflective inter-cell gap (Type 1) in bifacial modules, transmission loss was reduced, and the current is comparable between monofacial and bifacial modules in indoor STC front side flash test. However, due to manufacturing tolerances, the rear side current has a 14% drop between the Type 1 to Type 0 modules, which could be attributed to the encroachment of reflective coating in the inter-cell gap during the fabrication of glass.

While the simulation results give an initial indication of the type of bifacial module configuration and mounting tilt angle to be used during the outdoor energy yield study, the outdoor mounting sites in the US and in Singapore show that energy yield from bifacial modules was 8% to 13% more than the monofacial modules. The gain in energy yield from bifacial module compared to monofacial modules was more significant than the gain in having varying bifacial module configuration at 1% to 2% or the gain by varying cell type at 3.7%. However, the contribution of the inter-cell gap reflective layer, which was simulated to provide 2.4% to 3.4% current gain, was not seen in the outdoor energy yield. The Type 1 bifacial module was observed to have 1% to 2% lower energy yield, as compared to the Type 0 bifacial modules. This was discussed to be the result of the 14% lower bifacial ratio for the Type 1 module. Also, in the Singapore site which conducted the variable tilt angle outdoor energy yield monitoring, the Type 0 module has comparable efficiency at 0° while Type 1 increases from 5.52% to 6.75% on average when tilted to 45° due to the increase of internal reflectance when tilted to 45°. The assumption of decreasing current gain beyond 45° was not observed during this experiment.

A further enhancement of the simulation model can include rays reflected from the ground and their interaction with the module inter-cell gap reflective layer. The effect from reflected irradiance from the ground around the module contributes more to the bifacial module energy yield as it is physically larger, as compared to the 2 mm inter-cell gap, which contributes to the bifacial module front side direct irradiance current gain. To simulate the effect of ground-reflected irradiance on a 1.6 square-meter module, a different method of ray tracing will have to be studied. This will be covered in Chapter 5.

Chapter 5

Investigation of effect of ground irradiance on bifacial modules of varying configurations

In this chapter, an enhanced numerical model in MATLAB based on the limitations discussed in Section 4.6 is developed for a real-world configuration, which describes the whole module as a plane that could be rotated along its X-Z axis, and the discrete reflected rays are described as vectors. The simulation results are presented for the rear irradiance gain from the ground reflectance under the module, irradiance gain with a variable array-to-array gap, and the bifacial gain between the Type 0 and 1 modules. Last but not least, additional factors to consider in outdoor energy yield, like the effect of tilt angle and module mounting height, will be discussed in detail.

5.1 Numerical model

The module mounting conditions are simulated to be of long side horizontal mounting with a 1m array-to-array gap on both sides measuring from the edge of the module across all tilt angles in MATLAB and the assumptions and input parameters into MATLAB model are a continuation of Section 3.2. The module is modelled as 10 cells by 6 cells, as shown in Figure 5.1. The monofacial and Type 1 module configurations were simulated with the reflected rays from the array-to-array gap. The Type 0 bifacial module configuration without inter-cell gap reflective coating has a transparent area in between the cell, thus, the front irradiance could be transmitted to the ground directly under the module. Additional ground reflectance areas were added at the inter-cell gap area directly under the module to take into account the transmitted front irradiance through the module. Field measurements were made on the transmission ratio of the module which shows minimal front irradiance absorption by the module glass. Hence, an assumption was made that the rays directly under the module and the rays from the array-to-array gap have

the same irradiance.

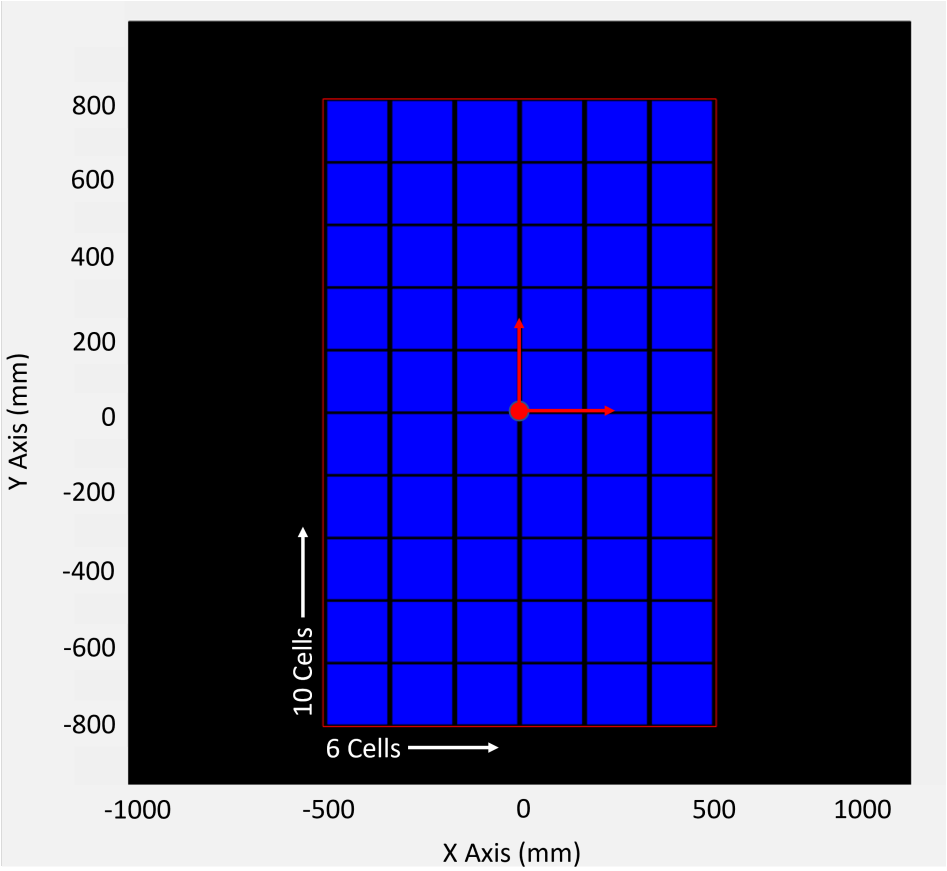

Figure 5.1: Top view of module layout modelled in MATLAB

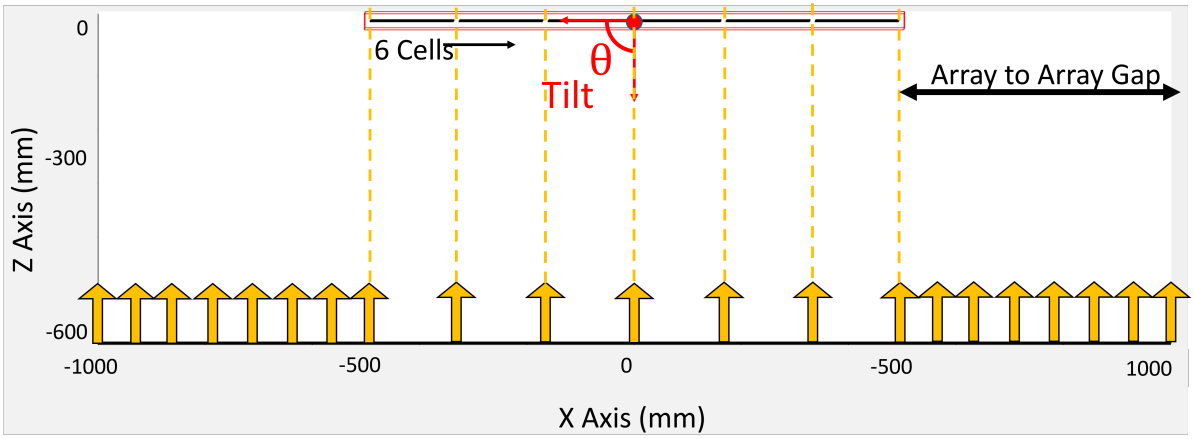

Figure 5.2: Ground reflected rays origin positions used for simulation

To verify if the rays' vectors intersect the main module plane and the sub-plane cells, a line-plane intersection algorithm was used [91] [92]. With the initial coordinates of each reflected ray cluster Cartesian coordinates being described by ($x = X_1$, $y = Y_1$, z = mounting height), as

plotted in Figure 5.2, the reflected rays are assumed to be uniformly scattered at intervals of 3° in the polar coordinates and at intervals of 6° in the azimuth coordinates. In the real world, the reflected rays are expected to propagate indefinitely till they are absorbed by a medium. To simplify the calculation for each ground-reflected ray vector, the maximum possible module height in the z plane z_{max} was first calculated using the geometrical properties of the module, with respect to the tilt angle, as illustrated in Figure 5.3. Rays vectors above the maximum module height z plane are assumed to be beyond the boundary condition of this simulation.

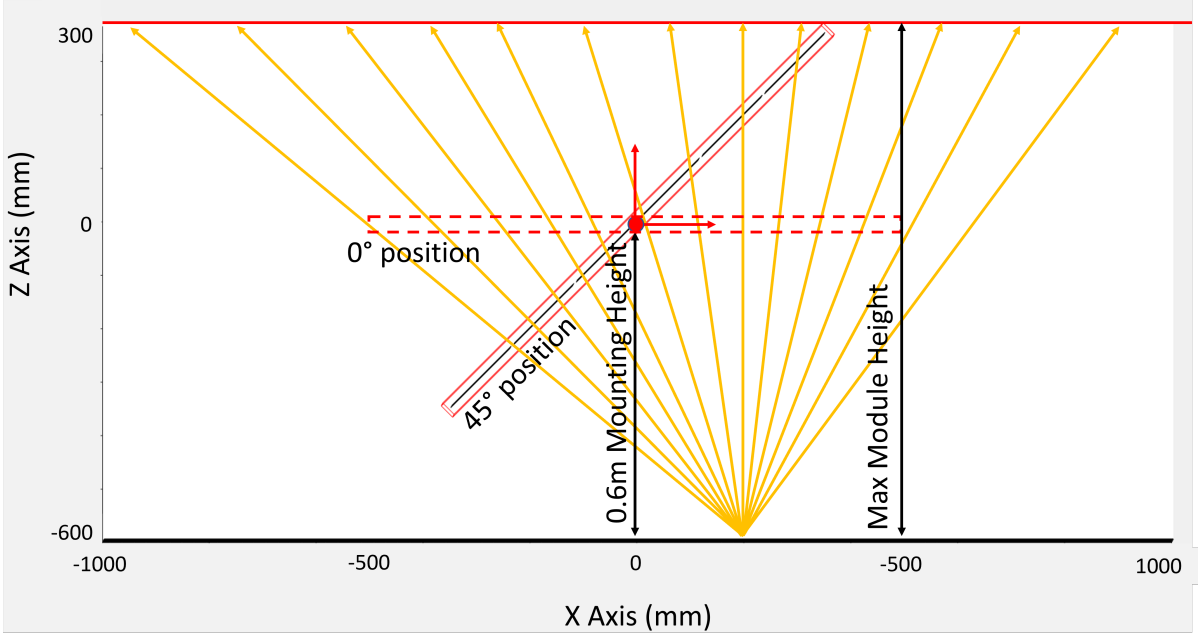

Figure 5.3: Scattered ground reflected rays scattering in polar axis and its intersection with the module

Equations (5.1), (5.2), and (5.3) were used to describe the initial and secondary positions of the ground-reflected scattered ray vector as it intersects the z plane at the maximum module height as follows.

$$x_2 = x_1 + z_{Max} \times \tan(\theta) \times \cos(\varphi), \tag{5.1}$$

$$y_2 = y_1 + z_{Max} \times \tan(\theta) \times \sin(\varphi), \tag{5.2}$$

$$z_2 = z_1 + z_{Max}, \tag{5.3}$$

where x_1, y_1, and z_1 being the initial coordinates and x_2, y_2, and z_2 being its final coordinates on the module and z_{Max} is the maximum module height, θ is the polar angle and φ is the azimuth angle.

To simulate variable mounting height and tilt angle, the module geometrical properties were assumed to be a fixed plane and rotated along its X-Z origin and or with a translation in the Z axis for variable module mounting height, as illustrated in Figure 5.3. The line vector of the ground reflected irradiance scattered ray could be described individually by Equation (5.4), where p_1 is the origin of the scattered ray, s is a variable number to describe the magnitude along the line and p_0 is the point where the ray intersects the maximum module height in the z-plane, which was calculated with Equations (5.1), (5.2), and (5.3).

Equation (5.4) could be simplified to Equation (5.5), where $p_0 - p_1$ is substituted with a vector $\boldsymbol{u}$. If the line is parallel to the module plane $\boldsymbol{v_0}$, the dot product with the module plane normal vector $\boldsymbol{n(a,b,c)}$ equals to zero. If the dot product is not zero, it intersects at a unique point and the dot product of the normal vector and the vector $\boldsymbol{w}$ from $\boldsymbol{v_0}$ to $\boldsymbol{p_0}$ equals to 0, as shown in Equation (5.6).

$$p(s) = p_1 + s \times (p_0 - p_1) \tag{5.4}$$

$$p(s) = p_1 + s \times \boldsymbol{u} \tag{5.5}$$

$$\boldsymbol{n} \cdot \boldsymbol{w} = 0 \tag{5.6}$$

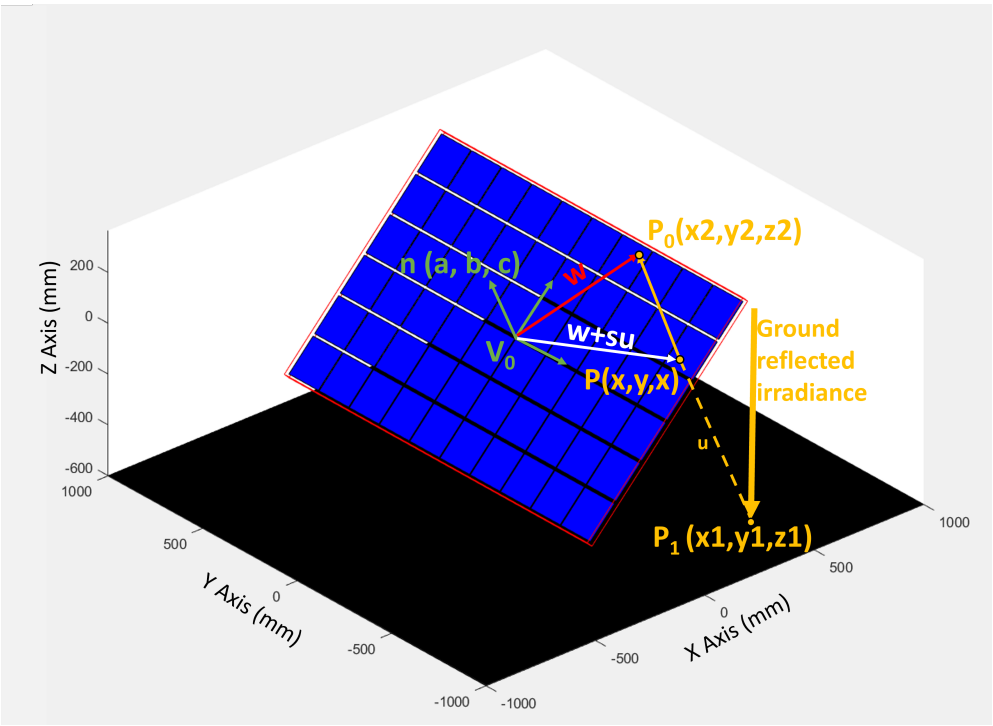

Figure 5.4: Visualisation of the Line-Plane intersection modelled in MATLAB

At the point of intersection, the vector could be described with Equation (5.7). If the dot product of its normal vector and the vector $\boldsymbol{w}+\boldsymbol{su}$ from $\boldsymbol{v_0}$ to $p(x,y,z)$ equals to 0, as shown in Equation (5.8), this can be solved in Equation (5.9) to obtain the intersection point $p(x,y,z)$ as follows [91].

$$p(x,y,z)-\boldsymbol{V_0}=\boldsymbol{w}+s\times\boldsymbol{u} \tag{5.7}$$

$$\boldsymbol{n}\cdot(\boldsymbol{w}-s\times\boldsymbol{u})=0 \tag{5.8}$$

$$p(x,y,z)=\frac{-\boldsymbol{n}\cdot\boldsymbol{w}}{\boldsymbol{n}\cdot\boldsymbol{u}}=\frac{\boldsymbol{n}\cdot(\boldsymbol{v_0}-\boldsymbol{p_0})}{\boldsymbol{n}\cdot(\boldsymbol{p_1}-\boldsymbol{p_0})}=\frac{-(ax+by+cz+d)}{\boldsymbol{n}\cdot\boldsymbol{u}} \tag{5.9}$$

With the known coordinates where the rays intersect the module plane, these positions were checked if they fall into any known subplanes of the cells with the test function, T_1 in Equation (5.10) before integrating the rays across the polar and azimuth angles, followed by the X and Y coordinates on the ground, for the sum of rays that contributes to the rear current.

$$P_{totalrear}=\int_{y_1}^{y_2}\int_{x_1}^{x_2}\int_{\varphi_1}^{\varphi_2}\int_{\theta_1}^{\theta_2}S(\theta)\times T1(cell_1,cell_2,cell_3,...,cell_{60})d\theta d\varphi dxdy \tag{5.10}$$

While most of the ground rays that are reflected to the rear of the module are absorbed by the rear of the cells, a small number of rays are reflected through the cell gap for Type 0 bifacial modules without the reflective white layer in the inter-cell gap. These can be reflected onto the front glass. This creates a secondary current contribution from the internal reflected rear rays that contributes to the total rear current. The internal reflectance rays have a few boundary conditions for internal reflectance contribution. Firstly, the rays must be reflected onto the module front glass with an incidence angle that is more than the critical angle of 41.8° [93] [86]. Secondly, only one bounce of the reflected rays is of significant irradiance level to contribute to the cell current generation. Lastly, the reflected rays are assumed to be fully specular as the module glass is planar on the encapsulated glass interface to improve transmission with the reflected angle, similar to its incoming incidence angle [68].

5.2 Simulation of Outdoor Bifacial Modules

In this section, the results from the updated model for Type 0 bifacial module rear irradiance gain in outdoor conditions will first be discussed. Second, s comparison of irradiance gains from the reflected ground irradiance for both monofacial and Type 0 bifacial modules will be carried out. Third, the irradiance gain for Type 0 and Type 1 bifacial modules will be discussed

and the influence of inter-cell gap white reflective area contribution will be compared to the internally reflected rays gain from the ground reflected irradiance. Last, a comparison of the updated model results to actual energy yield results will then be presented.

5.2.1 Rear Irradiance Gain From Ground Reflectance Under The Module

Figure 5.5 plots the rear irradiance across varying tilt angles at 1m and 0.8m module mounting heights. The simulated results are for Type 0 bifacial modules as it only considers the direct rays that were transmitted through the inter-cell gap of the module and reflected from the ground to the rear of the module. With an increased tilt angle from 0° to 75°, the resulting irradiance at 1m mounting height was reduced by 47%. Likewise, at 0.8m mounting height, the irradiance was reduced by 39% when the tilt angle increased from 0° to 75°. The rate of decrease of irradiance with an increased tilt angle is nearly similar for both 1m and 0.8m mounting heights. The percentage change in rear irradiance from an increase in mounting height of 0.8m to 1m, is reduced with an increase in tilt angle from 12% at 0° tilt angle to 24% at 75° tilt angle. This resulted in an average decrease of 17% across the range of tilt angles when the mounting height is increased from 0.8m to 1m.

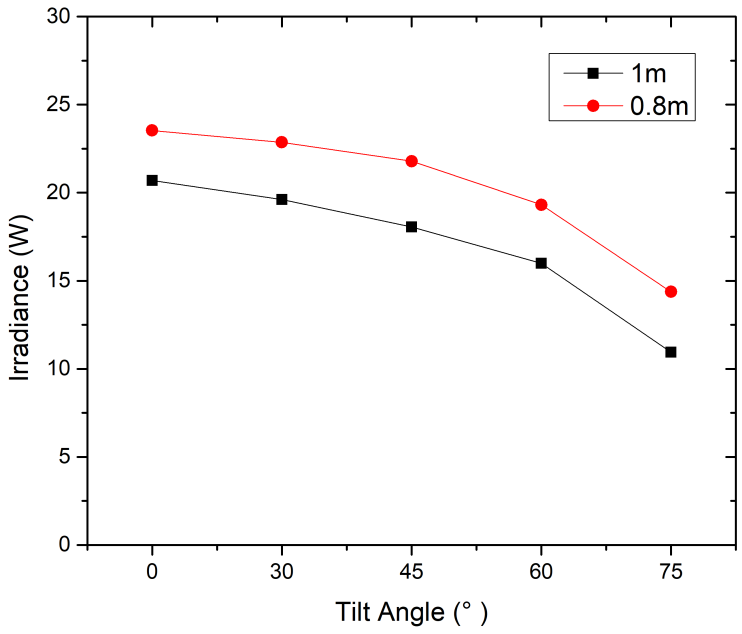

Figure 5.5: Rear irradiance per tilt angle with two mounting heights

The maximum current gain is seen for both mounting heights at 0° tilt angle, as shown in Figure 5.6 and Figure 5.7. The rear irradiance gain is plotted along the X-axis (ground) for both the 1m and 0.8m mounting heights. These graphs further explain that the main contribution to

rear irradiance gain comes from the rays directly under the centre of the module with reducing gain from rays that originate further away. The irradiance reflected from the edges of the module is significantly lesser than those originating in the middle of the module.

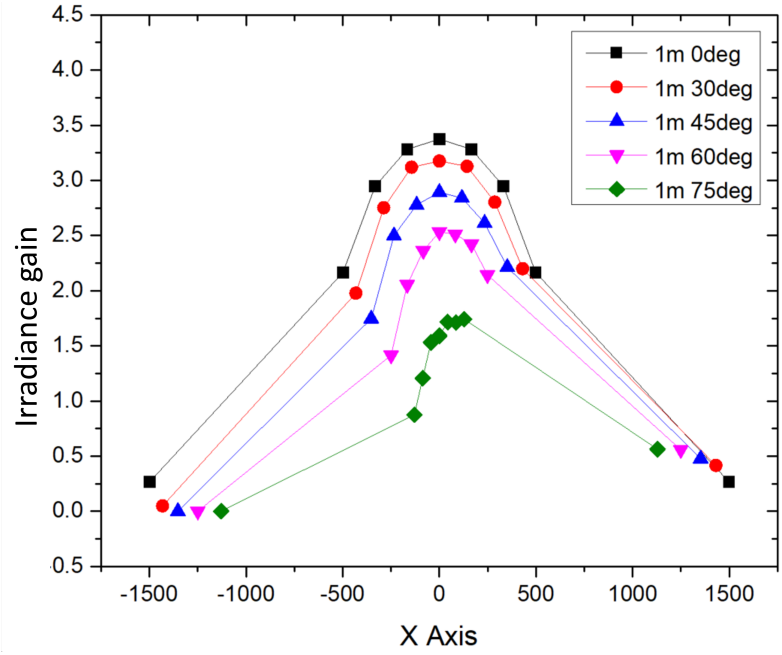

Figure 5.6: 1m height rear irradiance gain contribution from various origin along axis

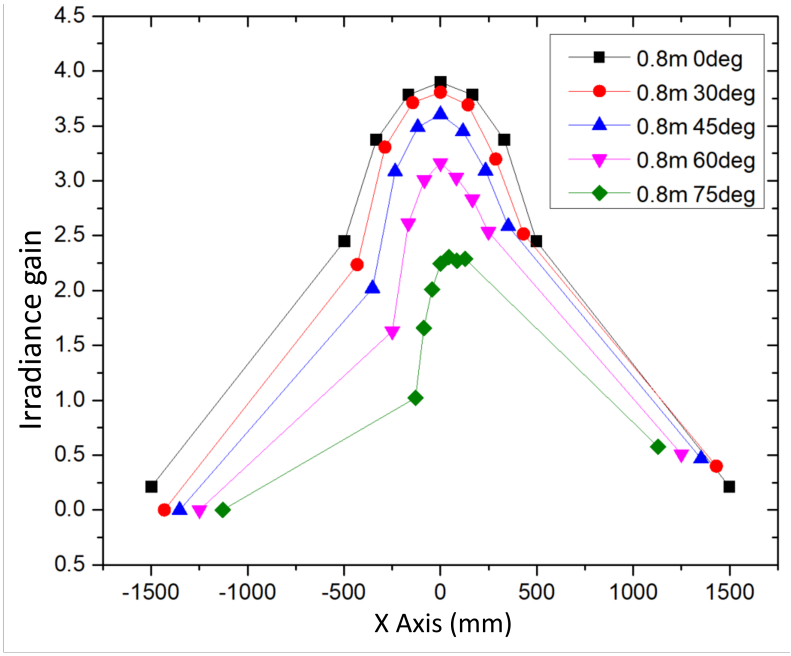

Figure 5.7: 0.8m height rear irradiance gain contribution from various origin along axis

Figure 5.8a, Figure 5.8b, and Figure 5.8c are the tilted module planes from 0°, 45° and 75° respectively, with the rays that are intersecting the rotated plane highlighted in yellow. Due to

the reduction in cross-section along the X-Z axis with increased tilt angle, the ground reflected rays are not collected by the rear of the module. At 0°, the module area is 1.6m in the Y axis and 1m in the X axis, resulting in a $1.6m^2$ collection surface. With the module tilted at 75°, the effective collection surface drops by 77% to $0.36m^2$.

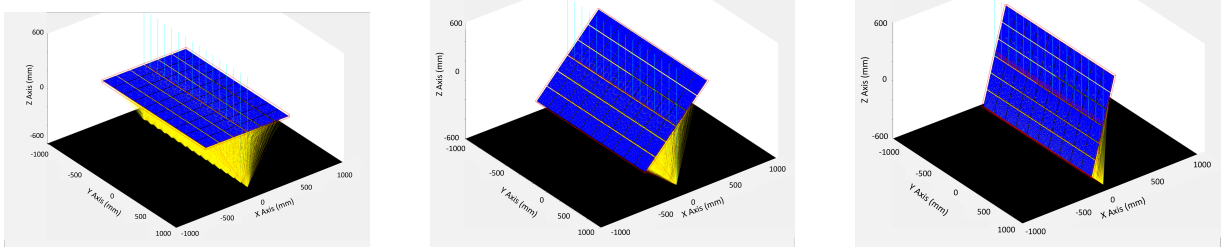

(a) 0° rear rays trace (b) 45° rear rays trace (c) 75° rear rays trace

Figure 5.8: Rear rays trace visualisation with tilt angle, x,y,z axis in mm

5.2.2 Irradiance Gain With Effect of Array To Array Gap

Ground reflected irradiance contributes strongly to the rear side irradiance gain at a low tilt angle. With an increase in tilt angle, the contributions are reduced. While only bifacial modules have rear side irradiance gain from ground reflected rays, those rays that were reflected to the front side of the module contribute to front side irradiance gain of both bifacial and monofacial modules. Hence in this section, a comparison of the irradiance gains on both the rear and front side from the ground reflected rays is discussed for monofacial and bifacial modules. As photovoltaic modules are mounted in an array, the ground reflected ray from the array to array gap of 1m on both sides of the module is taken into consideration.

In Figure 5.9, the simulated irradiance gain for bifacial Type 0 module and monofacial is plotted. At 90°, the bifacial module has twice the total irradiance gain as the monofacial module, as both sides of the module are absorbing the irradiance. As the module tilt angle reduces from 90° to 0°, the total irradiance gains for bifacial modules increase with the increasing rear irradiance gain while the front irradiance gain reduced for both bifacial and monofacial modules. When the tilt angle is less than 45°, there is zero irradiance gain from ground-reflected irradiance to the front side of the modules. Likewise, to the bifacial module with a lower mounting height of 0.8m from 1m at 90°, the monofacial module had a 30% increase in irradiance gain.

To further understand the effect of ground-reflected irradiance on the front of the module, each unit of ground-reflected rays was plotted in Figure 5.10 for modules mounted at a height of 1m. In Figure 5.11, the contribution of rear irradiance gain to the bifacial module was plotted. Similar to Figure 5.6 and Figure 5.7, the highest contribution to rear current at low tilt angle are those irradiances transmitted through the inter-cell gap and reflected directly under the module

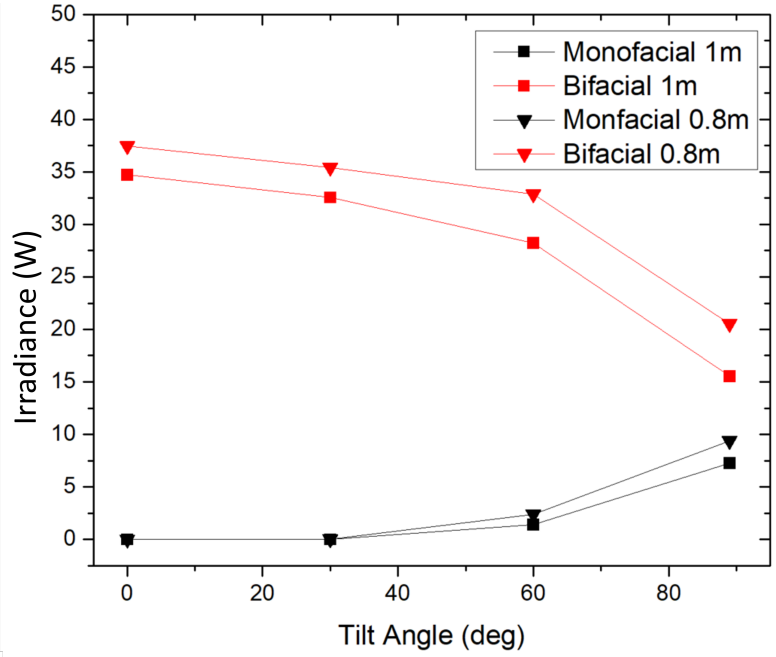

Figure 5.9: Irradiance gain of monofacial and bifacial modules at 1m and 0.8m mounting height with varying tilt angle

from point 12 to 16 along the X axis. As the tilt angle increases, contributions of rear irradiance gain from the ground directly under the module plotted as point 14 on the X axis reduces by 98% from 0° to 90°. The rear irradiance gain contribution from ground beyond the module increases by 121% at point 27. From Figure 5.7, the rear irradiance gain contribution from the edge most point is 92% lesser than the middle point directly under the module. This phenomenon resulted in the reduction in irradiance gain, as shown in Figure 5.9, with increasing tilt angle. While the decrease in irradiance gain from points directly under the module with increasing tilt angle is sizeable, there is a slight increase in front irradiance gain from ground-reflected irradiance with increasing tilt angle, which is plotted in Figure 5.10. Thus, the total irradiance gain for bifacial modules at increasing tilt angles is still reduced.

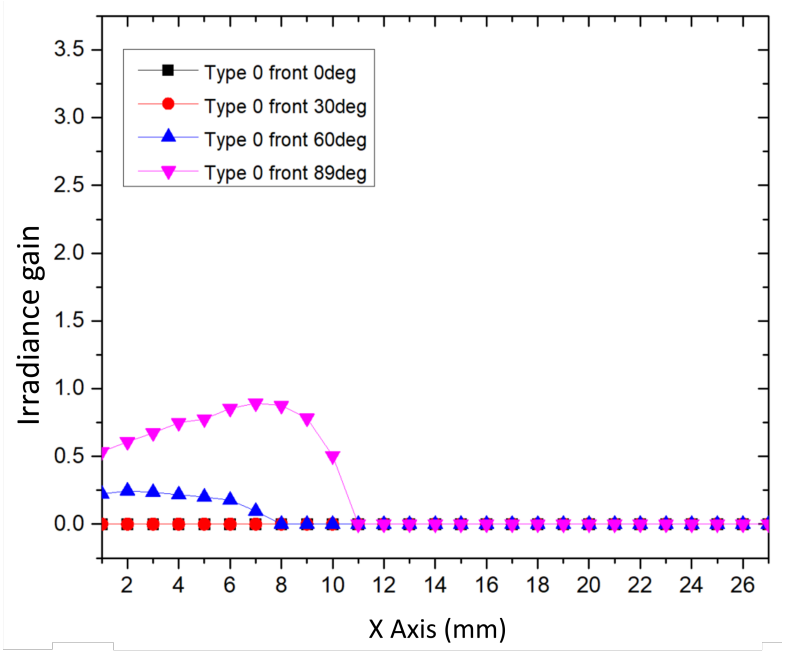

Figure 5.10: Front irradiance gain contribution from ground-reflected ray directly under the module with varying module tilt angle. This is illustrated for various origins along the X-axis.

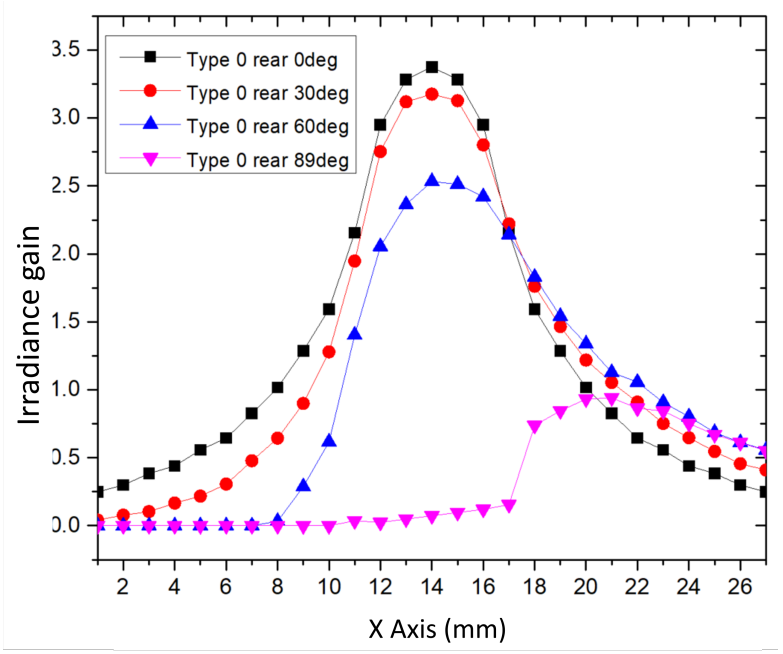

Figure 5.11: Rear irradiance gain from ground-reflected rays directly under the module with varying module tilt angle. This is illustrated for various origins along the X-axis

Across all tilt angles, the irradiance gain for bifacial modules are significantly higher than monofacial modules due to the additional irradiance gain from the rear, as seen in Figure 5.9. Like monofacial modules, bifacial modules could also absorb the additional irradiance gain from the front side of the module. Comparing the contribution from each unit of ground reflected ray

to the total irradiance gain for monofacial and bifacial modules in Figures 5.12 and 5.13, the main irradiance gain for bifacial modules are from the reflected rays directly under the module. This rear side gain is most significant at low modules tilt angle near 0°. Comparing additional ground-reflected irradiance gained with the front side direct irradiance on the module front, the net gain for Type 0 bifacial modules mounted at a tilt angle of 0° at 1m height with an array to array distance of 1m over monofacial modules is 27%. With the increase in tilt angle from 0° to 90°, the net gain increases sharply to 29%, 44%, and 688% at 30°, 60°, and 90° respectively due to the sharp reduction of the direct front side with increasing tilt angle.

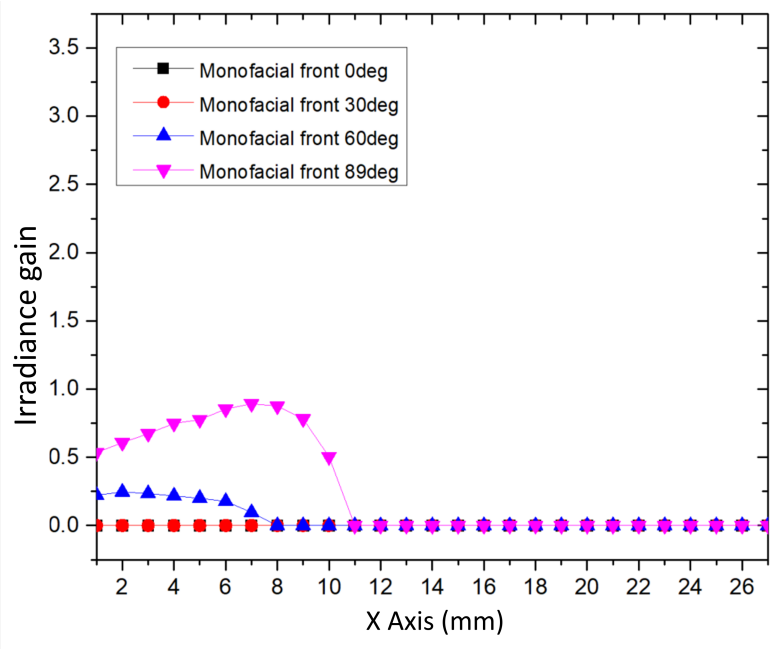

Figure 5.12: Monofacial total irradiance gain contribution from various origins along axis and varying module tilt angle

The comparison could be done between bifacial and monofacial modules mounted at the same varying tilt angles for technical understanding, but seldom are monofacial mounted at an angle as it is the most optimal mounted perpendicular to the direct irradiance at 0°. Therefore, if we compare the additional irradiance gain from ground reflected irradiance from a bifacial and a monofacial module with its mounting configuration optimised, the net gain for bifacial modules reduces from 27% at 0° to 25%, 22%, and 12% at 30°, 60°, and 90° respectively. From these simulations, the optimal tilt angle for both Type 0 bifacial and monofacial modules are both at 0°. Similar to the tilt angle, the module should be closer to the ground to capture the most ground-reflected irradiance. Considering the associated overheating risk with the lack of module ground clearance with loss in performance, and the minimal additional gain in reduced mounting height as compared to tilt angle, it would be prudent to optimise the Type 0 bifacial mount to 0° tilt angle with minimum manufacturer recommended ground clearance.

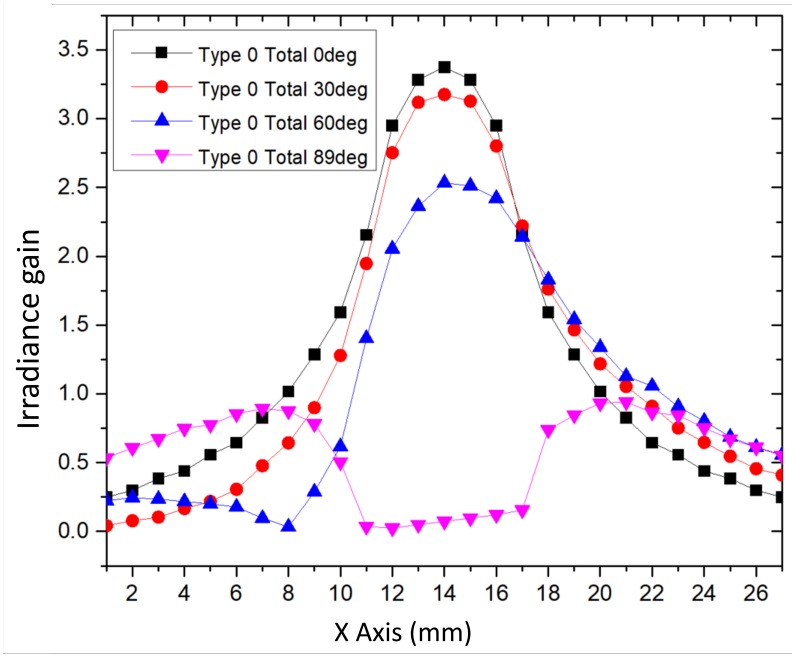

Figure 5.13: Bifacial total irradiance gain contribution from various origins along axis and varying module tilt angle

5.2.3 Irradiance Gain Comparison of Type 0 And Type 1 Module

Figure 5.14 plots the Type 0 and Type 1 bifacial module irradiance gain with varying tilt angles. There are significant differences between the irradiance gain of Type 0 and Type 1 bifacial modules across the tilt angle. The main difference between these two bifacial modules is the white reflective layer at the inter-cell gap. Without the white reflective layer that contributes to the front side current gain [52], the front direct irradiance could be transmitted through the module and to the ground directly below the module. This ground-reflected irradiance from transmitted irradiance was the main contributor to the irradiance gain when comparing Type 0 bifacial and monofacial modules in the previous section.

For Type 1 bifacial module, the total irradiance gain is 46% lesser, as compared to Type 0 bifacial modules at 0°. Like the Type 0 bifacial module, the irradiance gain from ground reflected irradiance decreases with increasing tilt angle for Type 1 bifacial modules. However, the decrease in irradiance gain from the increase of tilt angle from 0° to 90° is only 20% for Type 1, as compared to Type 0 of 55%. At 90°, both Type 0 and Type 1 bifacial modules have approximately the same irradiance gain. These two characteristics show that the reflected ground irradiance from directly under the module has little to no contribution to the module rear irradiance gain at 90° with a decreasing contribution when the tilt angle is increased. As both Type 0 and Type 1 bifacial modules have a similar design for the front side, they have similar front irradiance gain from ground-reflected irradiance.

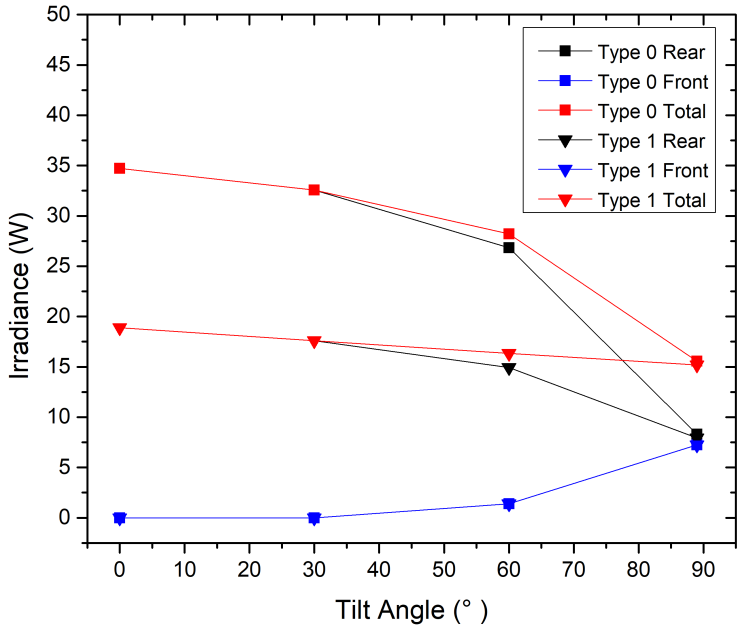

Figure 5.14: Type 0 and Type 1 bifacial module irradiance gain breaking down to rear, front, and total combining both

Likewise for the Type 1 bifacial module, each unit of ground-reflected rays' contribution to irradiance gain was plotted in Figure 5.15 and Figure 5.16. As expected from the Type 0 bifacial module, the lack of transmitted direct front irradiance through the module to be reflected by the ground results in no irradiance gain from reflected rays directly under the module between points 12 to 16. These results show that the contribution of rays from the array to array gap per meter square is half of those directly under the module.

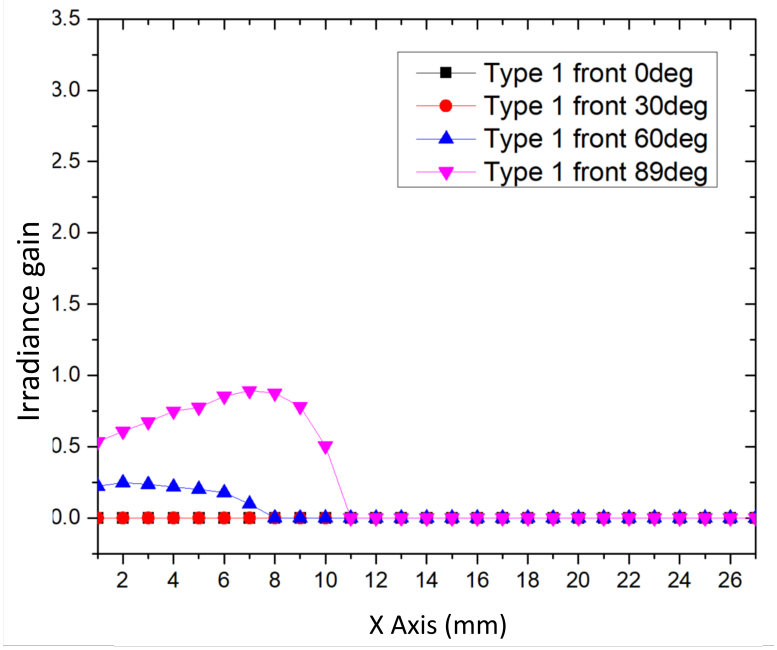

Figure 5.15: Type 1 front irradiance from ground-reflected rays directly under the module with varying module tilt angle. This is illustrated for various origins along the X-axis.

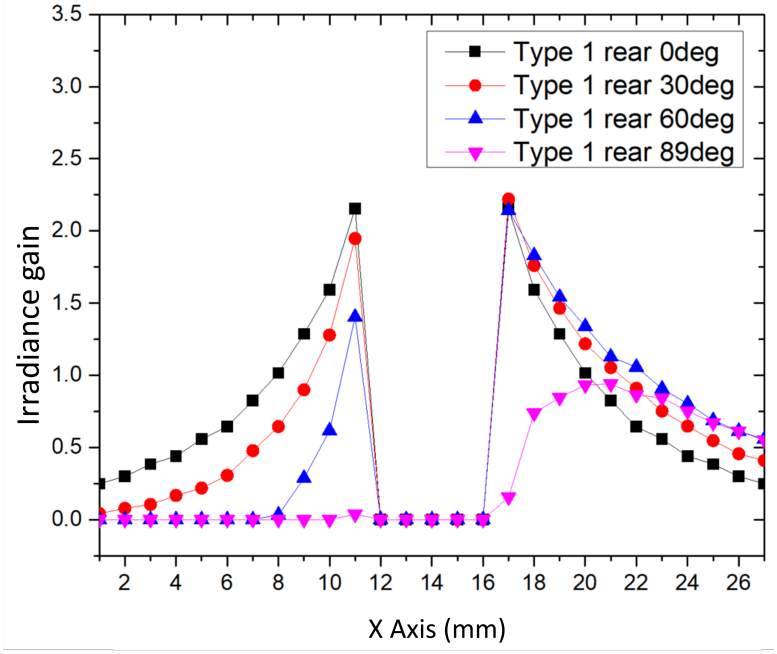

Figure 5.16: Type 1 rear irradiance from ground-reflected rays directly under the module with varying module tilt angle. This is illustrated for various origins along the X-axis.

Unlike Type 0 bifacial modules, the total ground reflected irradiance gain for Type 1 bifacial modules showed an expected drop similar to its drop in rear irradiance gain, as plotted in Figure 5.17. As these simulations are for ground-reflected irradiance, the additional contribution of the white reflective inter-cell gap for front internal reflection was not considered. As reported

previously in an indoor flash test, the Type 1 bifacial module has a 3.4% increase in generated current, as compared to Type 0 bifacial modules. The ground condition for these simulations was assuming a highly reflective roofing membrane of 80% weighted average reflectance, thus, Type 0 had a large 46% gain, as compared to Type 1 bifacial modules.

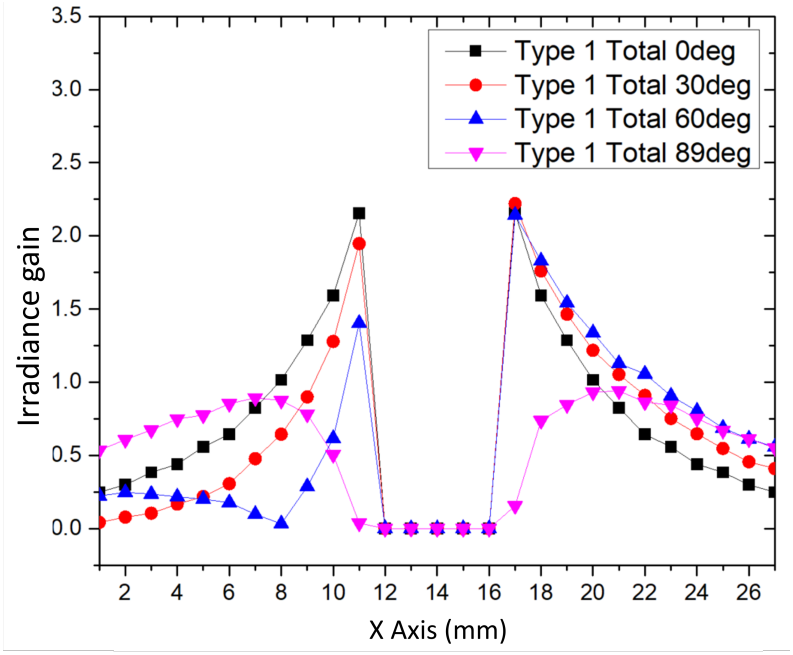

Figure 5.17: Type 1 total irradiance from ground-reflected rays directly under the module with varying module tilt angle. This is illustrated for various origins along the X-axis.

Figure 5.18 compares the effect of ground reflected irradiance to three different types of module configurations. Both bifacial modules have higher irradiance gain due to the intrinsic property of bifacial modules being able to absorb additional irradiance on their rear side. Type 0 bifacial modules have the highest irradiance gain at 0° mounting angle with Type 1 bifacial module at 46% drop, as compared to Type 0 bifacial module. The ground-reflected irradiance has little to no effect on monofacial modules till the module is tilted beyond 30° when ground-reflected rays from the array-to-array gap are reflected to the front of the modules. Like monofacial modules, bifacial modules do gain the same amount of front-side irradiance gain across all tilt angles. In a Type 0 bifacial module, the main contribution to its irradiance gain is from the ground-reflected rays that were transmitted through the transparent inter-cell gap. These reflected ray's contribution decreases with the increase of module tilt angle due to the decrease in the active area that is directly facing the ground. This phenomenon resulted in the coverage of irradiance gain for both Type 0 and Type 1 bifacial modules at 90° tilt angle.

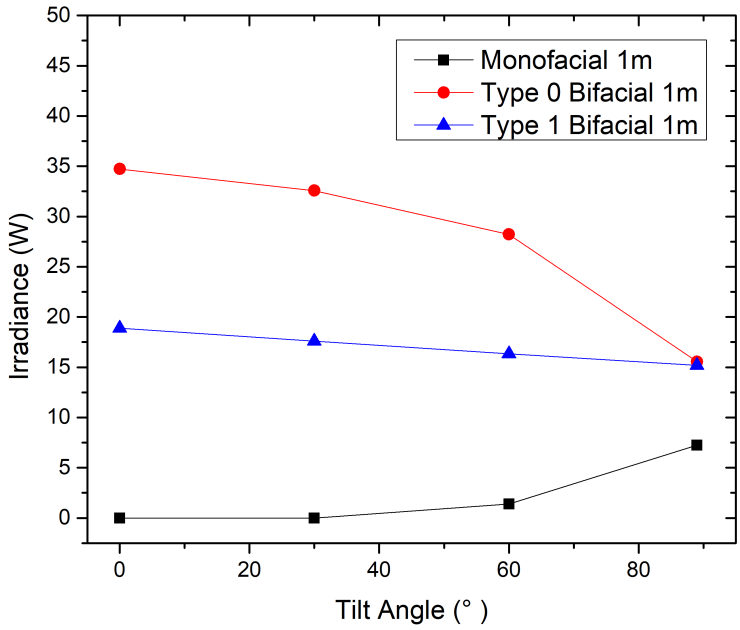

Figure 5.18: Ground reflected irradiance gain for monofacial and bifacial Type 0 and Type 1 modules

To compare the simulation results with the results from previously reported outdoor energy yield monitoring done in the US, the ground albedo was set at 60% as the ground cover at the mounting site mainly consists of soil. As those modules were mounted on a single-axis tracker, the module was always perpendicular to the direct irradiance. At 0° tilt angle, the total gain for Type 0 bifacial modules is at 16.1%, as compared to monofacial modules. The gain for Type 1 bifacial is at 8.8%, which is close to what was reported previously, where the energy yield from bifacial modules was 8% to 13% higher than the monofacial modules. The energy yield for the Type 0 bifacial module configuration was 1% to 2% higher, as compared to the Type 1 bifacial module. From the simulation shown in Table 5.1, the Type 0 bifacial module has about twice the irradiance gain from ground reflected irradiance, as compared to the Type 1 bifacial module. In this simulation, the transmission losses through the module glass and absorption loss in air were assumed to be minimal. This might lead to the overrating of reflected irradiance coming from directly under the module, thus giving the Type 0 module an inflated ground-reflected irradiance gain.

Table 5.1: Summary of gain from ground reflected irradiance when compared to the module initial front irradiance

Module Type	0° Tilt Angle Rear	0° Tilt Angle Front	0° Tilt Angle Total	90° Tilt Angle Rear	90° Tilt Angle Front	90° Tilt Angle Total
Monofacial	0%	0%	0%	0%	3.4%	3.4%
Bifacial Type 0	16.1%	0%	16.1%	3.8%	3.4%	7.2%
Bifacial Type 1	8.8%	0%	8.8%	3.6%	3.4%	7%

5.2.4 Additional Factors to Consider In Outdoor Energy Yield Scenario

Figure 5.19 illustrates the different pathways of irradiance interacting with the bifacial module. The first path is the direct front irradiance to the cells, which also directly contributes to the second path of internal reflectance from the white reflective layer at the inter-cell gap from front irradiance. The third path is when if the inter-cell gap is transparent, the transmitted rays contribute to the ground-reflected transmitted irradiance directly under the module. The last path is from the ground-reflected direct irradiance. While the reported model considers all these pathways, the absorption losses as irradiance travels through the module and air could be added to enhance the results from the model.

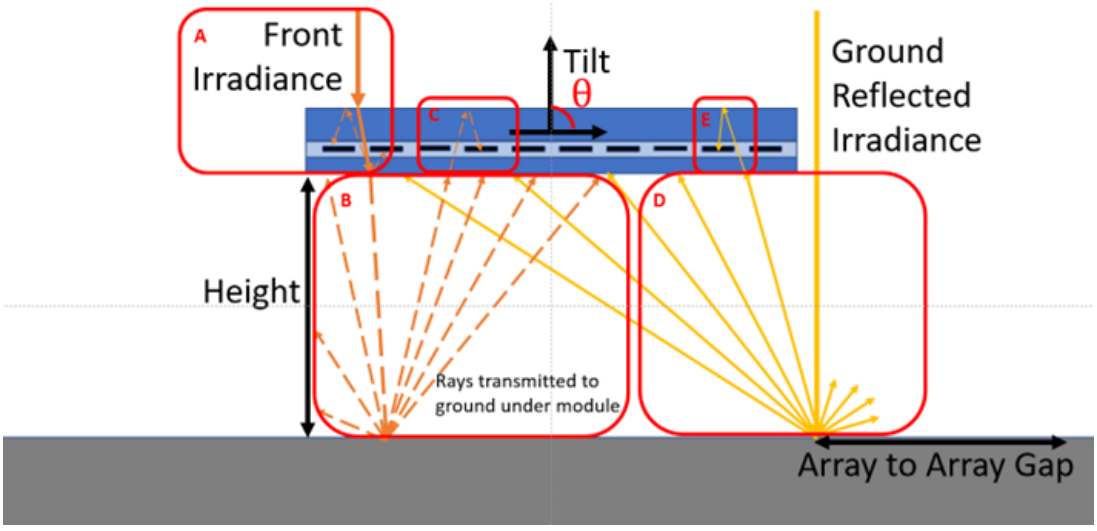

Figure 5.19: Bifacial module ray paths identified in an outdoor monitoring setup

5.3 Summary

In this chapter, an outdoor ray tracing model was further developed to simulate the current gain of outdoor bifacial modules, which can be used to provide guidance for optimal energy yield. The results of this simulation can be verified using outdoor performance monitoring data. From Chapter 3, it has been shown that the numerical ray tracing model agrees with the experimental results from the indoor flash test. Building upon the ray tracing module by including the interaction between the multiple cells in the module and the ground effect, the current gain of outdoor bifacial modules is simulated with the outdoor ray tracing model. Simulation results range from rear irradiance gain from ground reflectance under the module, irradiance gains with a variable array-to-array gap, and bifacial gain between Type 0 and Type 1 modules. The key results are as follows.

Firstly, from the simulation done on varying tilt angles for Type 0 bifacial modules, it was shown that the rear irradiance gain is a strong function of tilt angle. The main contributor of rear irradiance gain was identified to be reflected rays originating from directly under the module. Due to the reduction in cross-section along the X-Z axis with increased tilt angle, the ground reflected rays are not collected by the rear of the module. At 0° the module area is 1.6m in the Y axis and 1m in the X axis, resulting in a $1.6m^2$ collection surface. With the module tilted at 75°, the effective collection surface drops by 77% to $0.36m^2$.

Secondly, the irradiance gain for bifacial modules is significantly higher than monofacial modules across all tilt angles, due to the additional irradiance gain from the rear. Like monofacial modules, bifacial modules could also absorb the additional irradiance gain from the front side of the module. The net gain for Type 0 bifacial modules mounted at a tilt angle of 0° at 1m height with an array-to-array distance of 1m over monofacial modules is 27%. With the increase in tilt angle from 0° to 90°, the net gain increases sharply to 29%, 44%, and 688% at 30°, 60°, and 90° respectively due to the sharp reduction of the direct front side with increasing tilt angle. Seldom are monofacial mounted at an angle as it is the most optimal mounted perpendicular to the direct irradiance at 0°. Therefore, if we compare the bifacial module additional irradiance gain from ground reflected irradiance and a monofacial module with its mounting configuration optimised, the net gain for bifacial modules reduces from 27% at 0° to 25%, 22%, and 12% at 30°, 60°, and 90° respectively. From these simulations, the optimal tilt angle for both Type 0 bifacial and monofacial modules are both at 0°. Similar to the tilt angle, the module should be closer to the ground to capture the most ground-reflected irradiance.

Thirdly, for Type 1 bifacial module, the total irradiance gain is 46% lesser, as compared to Type 0 bifacial modules at 0°. Like the Type 0 bifacial module, the Type 1 bifacial module's irradiance gain from ground reflected irradiance decreases with increasing tilt angle. However,

the decrease in irradiance gain from the increase of tilt angle from 0° to 90° is only 20% for Type 1, as compared to Type 0 of 55%. At 90°, both Type 0 and Type 1 bifacial module has approximately the same irradiance gain.

Lastly, a comparison was done with the simulation results of irradiance gain from ground-reflected irradiance and the results from outdoor energy yield monitoring done in the US, which was discussed in Chapter 4. Type 0 bifacial modules that were previously fabricated for the outdoor experiments in the past reports were transferred to a mounting rack that is both height and tilt angle adjustable. Outdoor monitoring energy yield was conducted on these Type 0 modules and compared with the results from the outdoor ray tracing model for fixed height and 0 tilt angle. As those modules were mounted on a single-axis tracker, the module is always perpendicular to the direct irradiance at 0° tilt angle. The total gain for the Type 0 and Type 1 bifacial modules is 16.1% and 8.8%, as compared to monofacial module. It was reported that the energy yield from bifacial modules was 8% for Type 1 and 13% for Type 0 higher than the monofacial modules. However, in the simulation, the Type 0 bifacial module has about twice the irradiance gain from ground-reflected irradiance, as compared to the Type 1 bifacial module. Further enhancement of the simulation model would include the transmission losses through the module glass and absorption losses in the air.

Chapter 6

Conclusion and Future Works

6.1 Conclusion

This thesis contributes to the modelling and characterisation of industrial bifacial solar cells for higher efficiency modules in the following areas;

- In Chapter 3, three new bifacial module configurations with reflective layer coated at different positions are proposed and studied in detail, namely Configuration 1: Glass / EVA / Bifacial Solar Cell / EVA / Glass / Reflective Layer, Configuration 2: Glass / EVA / Bifacial Solar Cell / EVA / Reflective Layer / Glass, and Configuration 3: Glass / EVA / Reflective Layer / Bifacial Solar Cell / EVA / Glass designs. To the best of our knowledge, these additional designs for bifacial modules with white reflective coating have not been reported in any existing literature.

- In Chapter 3, an optical ray trace model for each of the three configurations was created with inputs from test measurements. The simulation of the three configurations considered the absorption loss in the simulation of the current gain from each configuration with varying inter-cell gap distances. The corresponding performance gain was evaluated for models with and without absorption loss. The simulation demonstrated that illumination conditions would change the optimal reflective coating design with Configuration 1 having the highest current gain of 3.4% with front-side illumination. But with rear illumination, Configuration 1 had no additional gain as the reflective layer reflects the rays out of the module. With rear-side illumination, Configuration 2 had the highest current gain of 2.2% gain, and Configuration 3 provided 1.8% current gain, whereas Configuration 1 produced the least gain of 1.7%. These findings reported in Chapter 3 are in line with the published results from other researchers and are the main push for industrial bifacial modules to mostly incorporate white reflective coating for STC performance gain.

- In Chapter 4, material optimisation and analysis were carried out with the identification of an optimal tilt for Type 1 bifacial module configuration. A range of varying tilt angles was simulated to identify the optimal material thickness and tilt for maximum current gain bifacial modules with a white reflective coating at the cell gap. A tilt angle of 45° was proposed and validated to be beneficial for modules with white coating due to the additional rays being captured and reduced self-shading.

- In Chapter 4, monofacial and bifacial modules with different white reflective coating configurations were fabricated for indoor flash tests and outdoor monitoring energy yield. Reported gains of 2% to 3% current gain were measured for bifacial modules with the different white reflective coating configurations to further validate the findings from the simulation model for STC performance. Performance gain during the indoor STC flash test from reflective layer coating in the cell gap of bifacial did not result in better outdoor performance during our outdoor energy yield monitoring. These conflicting results reported in Chapter 4 substantiated the conflicting acceptance of bifacial module designs between the utilities and residential PV market due to their differing needs.

- In Chapter 5, the effect of ground reflected irradiance on three different types of bifacial modules configurations: (i) Monofacial, (ii) Bifacial, and (iii) Bifacial with white reflective coating were modelled with ray tracing. The main contribution to bifacial module irradiance gain is from the ground reflected rays that were transmitted through the transparent inter-cell gap of bifacial modules which is absent in bifacial modules with white reflective coating. These reflected ray's contribution also decreased with the increase of module tilt angle due to the decrease in the active area that is directly facing the ground. These results reported in Chapter 5 contribute to the optimal mounting conditions for bifacial modules.

- In conclusion, the optimal modules design proposed for STC indoor front illumination flash test is Configuration 1: Glass / EVA / Bifacial Solar Cell / EVA / Glass / Reflective Layer giving a 3.4% gain. For indoor front and rear illumination flash test, Configuration 2: Glass / EVA / Bifacial Solar Cell / EVA / Reflective Layer / Glass gives a 2.2% gain. For outdoor performance on a tracker that keeps the module at 0° to the sun at all times, a bifacial module without a white reflective layer would give the highest gain for utility PV applications. For a fixed installation in commercial and residential PV, the optimal module would be Configuration 1: Glass / EVA / Bifacial Solar Cell / EVA / Glass / Reflective Layer at a 45° tilt. This identification of the various optimal modules and their mounting conditions would enable a reduction of LCOE for solar energy.

6.2 Suggestion For Future Works

This thesis has reported on the design ideas of modelling and characterisation for higher efficiency bifacial modules but more areas of the research gap were identified in the field of bifacial modules which will be discussed in this section for potential future work to enhance the research field.

6.2.1 Combined Bifacial Module Model and Verification

Most researchers worked on either the module internal ray tracing model whose end goal is to predict the module indoor flash test results and optimise the module design or an external ray tracing model from a ground-up approach, as discussed in Chapter 2 for an energy yield optimisation. To the best of our knowledge, there are only a few reported works, which considered a combined model, which combines the contents of Chapter 3, 4, and 5 in this thesis. This combined model would enable researchers to design and quantify the improvements done in the bifacial module internally to relate its impact to the energy yield. This segmented research, which splits the PV industry squarely between optimising module designs for indoor-rated flash tests and optimising mounting conditions for outdoor energy yield, is slowly eroding as more solar module manufacturers are going downstream into energy generation with self-consumption of their PV modules and energy generation companies are moving upstream to manufacture their own modules rather than buying off the shelf. With this consolidation, the importance of having a combined model which addresses bifacial module design optimisation and energy yield would serve the entire solar food chain.

Different kinds of PV modules have been and would be installed across the globe, but few sites were designed to compare between variable mounting height and tilt of bifacial modules as most sites' primary goal is energy generation. Thus, the expansion of our test bed in Singapore to verify the simulation results from reflected ground irradiance with varying mounting height and tilt would be beneficial to substantiate the findings in Chapter 5 and the future combined bifacial model. The tilt angle could be adjusted from 0° to 90° with variable height.

6.2.2 Effect of Bifacial Cells Efficiency Mismatch In Module With Reflective Layer

For optimal PV module power during indoor flash tests and outdoor energy yield, the modules must be built with PV cells of the same current-voltage characteristic. For a monofacial cell, an 8% difference in front current for one of the 60 cells in a module from sorting discrepancy would result in 1% power loss during indoor flash test [94]. This power loss from cell mismatch would be twice as severe in bifacial cells due to it having front and rear currents. The colour of the PV cell seen visually could correlate with the cell current as both are determined by the

refractive index and thickness of the anti-reflection coating [95]. Thus, the cells are presently colour-sorted with a visual inspection camera before being measured in an indoor flash test. The sorting done on bifacial cells does not consider the rear side colour or current. Hence, this results in the PV cells in the modules fabricated to have a tight and uniform control of colour on the front but a mismatch in colour for the rear.

Studies reported for Type 0 bifacial modules show that a maximum of 2-Watt gain could be achieved with additional rear sorting and it has a strong influence on module power class distribution in mass production [96]. The reflective layers at the inter-cell gap contribute to the current gain in Type 1 bifacial modules. This current gain would exacerbate the rear current mismatch in the Type 1 bifacial module. Hence, alongside the characterisation and optimisation of modules with reflective layers, an investigation on the effect of bifacial cells efficiency mismatch for modules with a reflective layer on module performance should be conducted. As solar cells are manufactured in a high volume and fast moving industry, with this additional function being incorporated into the model, the manufacturers will be able to develop control measures which do not increase complexity or cost. The effect of mismatch can also be logged and reported to allow greater accuracy in the reporting of module performance in this field.

6.2.3 Effect of Module Interconnection of Bifacial Modules

The basic design of bifacial modules discussed in this thesis was on bifacial modules with a white reflective layer in the inter-cell gap as solar cells were connected together with a slight gap in between the cells where the coating could be applied. However, recent developments have enabled a new method of connecting the solar cells together in a module via overlaying and stacking the solar cells together creating a shingling module similar to a shingled roof where roof tiles are overlaid and stacked together, as shown in Figure 6.1. The advantage of this method is a large increase in rated power in indoor flash test due to the higher quantity of solar cells that were squeezed into each module. This will also provide a better outdoor performance, as compared to the conventional modules [97].

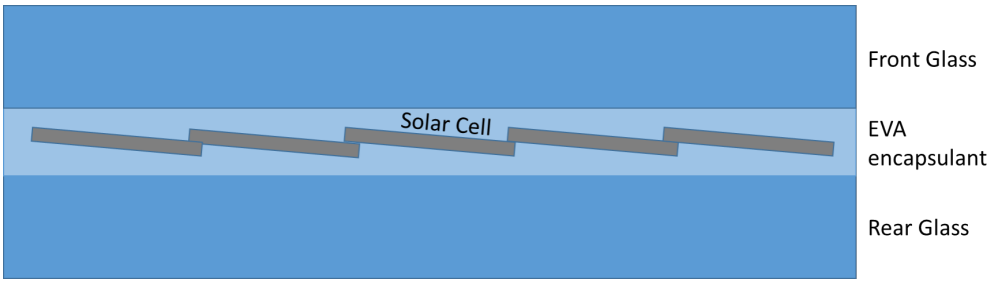

Figure 6.1: Cross-section of a shingling bifacial solar module with overlapping cell and without cell gaps

While many works on shingling module designs have been reported by researchers,it was the continuous decrease in manufacturing cost and increase in the volume of solar cells being

manufactured that has made this type of module interconnection favorable to manufacturers [98]. This new method of module interconnection removed the inter-cell gap and hence the drop in recently reported work on bifacial modules with a white reflective coating. However, we believe that the modelling and characterisation methods and results from the work done in this thesis could also include the various novel module interconnection to enable researchers to analyze the merit of their designs.

Bibliography

[1] International Renewable Energy Agency (IRENA), “World Energy Transitions Outlook 2023: 1.5°C Pathway” Annual Report, 2023.

[2] REN21, “Renewables 2023 Global Status Report” Annual Report, 2023.

[3] Wood Mackenzie, “Renewables 2022 Global Status Report” Annual Report, Dec 2021.

[4] Ballif, C., Haug, FJ., Boccard, M. et al., "Status and perspectives of crystalline silicon photovoltaics in research and industry.", Nat Rev Mater 7, 2022.

[5] R. Kopecek and J. Libal, “Bifacial Photovoltaics 2021: Status, Opportunities and Challenges,” Energies, vol. 14, no. 8, p. 2076, 2021.

[6] Kopecek, R., Libal, J. "Towards large-scale deployment of bifacial photovoltaics". Nat Energy 3, 443–446, 2018.

[7] J. A. M. van Roosmalen, S. L. Luxembourg, J. Liu, L. A. G. Okel, and B. B. Van Aken, "White Bifacial Modules – Improved STC Performance Combined with Bifacial Energy Yield,” 32nd European Photovoltaic Solar Energy Conference and Exhibition, pp. 42–47, 2016.

[8] J. P. Singh, S. Guo, I. M. Peters, A. G. Aberle, and T. M. Walsh, “Comparison of Glass/Glass and Glass/ Backsheet PV Modules Using Bifacial Silicon Solar Cells,” IEEE Journal of Photovoltaics, vol. 5, no. 3, pp. 783–791, 2015.

[9] Energy Market Authority (EMA) Singapore, "Singapore Energy Statistics 2022” Annual Report, 2022.

[10] S. Guo et al., “Investigation of the short-circuit current increase for PV modules using halved silicon wafer solar cells,” Solar Energy Materials and Solar Cells, vol. 133, pp. 240–247, 2015.

[11] A. G. Aberle, T. M. Walsh, and J. P. Singh, “Performance Investigation of Bifacial PV Modules in the Tropics,” 27th European Photovoltaic Solar Energy Conference and Exhibition, pp. 3263–3266, 2012.

[12] S. Wang et al., “Bifacial Photovoltaic Systems Energy Yield Modelling,” Energy Procedia, vol. 77, pp. 428–433, 2015.

[13] U. A. Yusufoglu et al., “Simulation of Energy Production by Bifacial Modules with Revision of Ground Reflection,” Energy Procedia, vol. 55, pp. 389–395, 2014.

[14] E. Sng, A. Sahadevan, S. Channabasappa Devihosur, S. Rohini, K. Malar, S. Roy, I.L.H. Lim, “Optimisation of Bifacial Photovoltics Module with Reflective Layer in Outdoor Performance,” 36th European Photovoltaic Solar Energy Conference and Exhibition, pp. 1007–1011, 2019.

[15] Berrian, D., Libal, J., Klenk, M., Nussbaumer, H. and Kopecek, R., "Performance of Bifacial PV Arrays With Fixed Tilt and Horizontal Single-Axis Tracking: Comparison of Simulated and Measured Data," IEEE Journal of Photovoltaics, 9(6), pp.1583-1589, 2019.

[16] Liliana, E. P. Yoewono and R. Intan, "Transparency modeling for mesh object using ray tracing," 2016 International Electronics Symposium (IES), Denpasar, pp. 385-388., 2016.

[17] C. W. Hansen et al., "A Detailed Model of Rear-Side Irradiance for Bifacial PV Modules," IEEE 44th Photovoltaic Specialist Conference (PVSC), Washington, DC, pp. 1543-1548., 2017.

[18] C. W. Hansen et al., "Analysis of irradiance models for bifacial PV modules," IEEE 43rd Photovoltaic Specialists Conference (PVSC), Portland, OR, pp. 0138-0143, 2016.

[19] Guo, S., Schneider, J., Lu, F., Hanifi, H., Turek, M., Dyrba, M. and Peters,I., "Investigation of the short-circuit current increase for PV modules using halved silicon wafer solar cells," Solar Energy Materials and Solar Cells, 133, pp.240-247, 2015.

[20] A. Luque, A. Cuevas, and J. M. Ruiz, “Double-sided n+-p-n+ solar cell for bifacial concentration,” Solar Cells, vol. 2, no. 2, pp. 151–166, 1980.

[21] A. Cuevas, A. Luque, J. Eguren, and J. del Alamo, “50 Per cent more output power from an albedo-collecting flat panel using bifacial solar cells,” Solar Energy, vol. 29, no. 5, pp. 419–420, 1982.

[22] Y. Schiele, N. H. Brinkmann, G. Hahn, and B. Terheiden, “Comparison of bifacial and monofacial large-area n-type Si solar cells from 100 um thin wire-sawn wafers,” 31st European Photovoltaic Solar Energy Conference and Exhibition, pp. 399–403, 2015

[23] M. A. Green and M. J. Keevers, “Optical properties of intrinsic silicon at 300K,” Progress in Photovoltaics: Research and Applications, vol. 3, no. 3, pp. 189–192, 1995.

[24] Chih-Tang Sah, K. A. Yamakawa, and R. Lutwack, "Effect of thickness on silicon solar cell efficiency," IEEE Transactions on Electron Devices, vol. 29, no. 5, pp. 903–908, 1982.

[25] O. von Roos, "A simple theory of back surface field (BSF) solar cells," Journal of Applied Physics, vol. 49, no. 6, pp. 3503–3511, 1978.

[26] A. Kranzl, R. Kopecek, K. Peter, and P. Fath, "Bifacial Solar Cells on Multi-Crystalline Silicon with Boron BSF and Open Rear Contact," IEEE 4th World Conference on Photovoltaic Energy Conference, 2006.

[27] J. Acker, T. Koschwitz, B. Meinel, R. Heinemann, and C. Blocks, "HF/HNO3 Etching of the Saw Damage," Energy Procedia, vol. 38, pp. 223–233, 2013.

[28] H. Park, S. Kwon, J. S. Lee, H. J. Lim, S. Yoon, and D. Kim, "Improvement on surface texturing of single crystalline silicon for solar cells by saw-damage etching using an acidic solution," Solar Energy Materials and Solar Cells, vol. 93, no. 10, pp. 1773–1778, 2009.

[29] S. Yang, P. Ge, and L. Zhang, "The effects of different parameters of pyramidal textured silicon surface on the optical reflectance," Solar Energy, vol. 134, pp. 392–398, 2016.

[30] H. Wagner et al., "Optimizing phosphorus diffusion for photovoltaic applications: Peak doping, inactive phosphorus, gettering, and contact formation," Journal of Applied Physics, vol. 119, no. 18, 2016.

[31] S. Duttagupta, B. Hoex, and A. G. Aberle, "Progress with surface passivation of heavily doped n+ silicon by industrial PECVD SiNx films," IEEE 42nd Photovoltaic Specialist Conference (PVSC), 2015.

[32] M. Rauer, C. Schmiga, J. Krause, R. Woehl, M. Hermle, and S. W. Glunz, "Further analysis of aluminum alloying for the formation of p+ regions in silicon solar cells," Energy Procedia, vol. 8, pp. 200–206, 2011.

[33] T. Fellmeth et al., "20.1% Efficient Silicon Solar Cell With Aluminum Back Surface Field," IEEE Electron Device Letters, vol. 32, no. 8, pp. 1101–1103, 2011.

[34] Y. Chen, H. Shen, and P. P. Altermatt, "Analysis of recombination losses in screen-printed aluminum-alloyed back surface fields of silicon solar cells by numerical device simulation," Solar Energy Materials and Solar Cells, vol. 120, pp. 356–362, 2014.

[35] T. Dullweber and J. Schmidt, "Industrial Silicon Solar Cells Applying the Passivated Emitter and Rear Cell (PERC) Concept—A Review," IEEE Journal of Photovoltaics, vol. 6, no. 5, pp. 1366–1381, 2016.

[36] Y. Lee, C. Park, N. Balaji, Y.-J. Lee, and V. A. Dao, “High-efficiency Silicon Solar Cells: A Review,” Isreal Journal of Chemistry, vol. 55, no. 10, pp. 1050–1063, 2015.

[37] C. Schwab et al., “Passivation of Inline Wet Chemically Polished Surfaces for Industrial PERC Devices,” Energy Procedia, vol. 27, pp. 573–579, 2012.

[38] A. G. Aberle, “Surface passivation of crystalline silicon solar cells: a review,” Progress in Photovoltaics: Research and Applications, vol. 8, no. 5, pp. 473–487, 2000.

[39] R. S. Bonilla, B. Hoex, P. Hamer, and P. R. Wilshaw, “Dielectric surface passivation for silicon solar cells: A review,” Physica status solidi(a), vol. 214, no. 7, p. 1700293, 2017.

[40] S. Riegel, F. Mutter, T. Lauermann, B. Terheiden, and G. Hahn, “Review on screen printed metallization on p-type silicon,” Energy Procedia, vol. 21, pp. 14–23, 2012.

[41] M. A. Green, “The Passivated Emitter and Rear Cell (PERC): From conception to mass production,” Solar Energy Materials and Solar Cells, vol. 143, 2015.

[42] J. E. Cotter, J. H. Guo, P. J. Cousins, M. D. Abbott, F. W. Chen, and K. C. Fisher, “P-Type Versus n-Type Silicon Wafers: Prospects for High-Efficiency Commercial Silicon Solar Cells,” IEEE Transactions on Electron Devices, vol. 53, no. 8, pp. 1893–1901, 2006.

[43] J. Greulich et al., “Optical Simulation and Analysis of Iso-textured Silicon Solar Cells and Modules Including Light Trapping,” Energy Procedia, vol. 77, pp. 69–74, 2015.

[44] V. D. Mihailetchi, H. Chu, G. Galbiati, C. Comparroto, A. Halm, and R. Kopecek, “A Comparison Study of n-type PERT and IBC Cell Concepts with Screen Printed Contacts,” Energy Procedia, vol. 77, pp. 534–539, 2015.

[45] A. Lanterne, J. Le Perchec, S. Gall, M. Coig, A. Tauzin, and Y. Veschetti, “20.5% Efficiency on Large Area N-type PERT Cells by Ion Implantation,” Energy Procedia, vol. 55, pp. 437–443, 2014.

[46] C.-C. Chen et al., “High Efficiency on Boron Emitter n-type Cz Silicon Bifacial Cells with Industrial Process,” Energy Procedia, vol. 38, pp. 416–422, 2013.

[47] Gautam Raina, Sunanda Sinha, "A holistic review approach of design considerations, modelling, challenges and future applications for bifacial photovoltaics", Energy Conversion and Management, Volume 271, 2022.

[48] “Measurement of Solar Cell Efficiency | PVEducation.” [Online]. Available: http://pveducation.org/pvcdrom/characterisation/measurement-of-solar-cell-efficiency. [Accessed: 22-Apr-2022].

[49] C. Duran, H. Deuser, R. Harney, and T. Buck, “Approaches to an Improved IV and QE Characterization of Bifacial Silicon Solar Cells and the Prediction of their Module Performance,” Energy Procedia, vol. 8, pp. 88–93, 2011.

[50] W. Warta and J. Hohl-Ebinger, “Bifacial Solar Cells in STC Measurement,” 25th European Photovoltaic Solar Energy Conference and Exhibition / 5th World Conference on Photovoltaic Energy Conversion, 6-10 Sept. 2010, Valencia, Spain, pp. 1358–1362, 2010.

[51] R. Guerrero-Lemus, R. Vega, T. Kim, A. Kimm, and L. E. Shephard, “Bifacial solar photovoltaics – A technology review,” Renewable and Sustainable Energy Reviews, vol. 60, pp. 1533–1549, 2016.

[52] J. P. Singh, T. M. Walsh, and A. G. Aberle, “A new method to characterize bifacial solar cells,” Progress in Photovoltaics: Research and Applications, vol. 22, no. 8, pp. 903–909, 2014.

[53] G. Razongles et al., “Bifacial Photovoltaic Modules: Measurement Challenges,” Energy Procedia, 2016.

[54] J. P. Singh, A. G. Aberle, and T. M. Walsh, “Electrical characterization method for bifacial photovoltaic modules,” Solar Energy Materials and Solar Cells, vol. 127, pp. 136–142, 2014.

[55] Y. Zhang, Q. Gao, Y. Yu, and Z. Liu, “Comparison of Double-Side and Equivalent Single-Side Illumination Methods for Measuring the I–V Characteristics of Bifacial Photovoltaic Devices,” IEEE Journal of Photovoltaics, vol. 8, no. 2, pp. 397–403, 2018.

[56] Preeti Kumari Sahu, J.N. Roy, C. Chakraborty, "Performance assessment of a bifacial PV system using a new energy estimation model", Solar Energy, Volume 262, 2023.

[57] K. R. McIntosh, R. M. Swanson, and J. E. Cotter, “A simple ray tracer to compute the optical concentration of photovoltaic modules,” Progress in Photovoltaics: Research and Applications, vol. 14, no. 2, pp. 167–177, Mar. 2006.

[58] K. R. McIntosh, J. N. Cotsell, J. S. Cumpston, A. W. Norris, N. E. Powell, and B. M. Ketola, “An optical comparison of silicone and EVA encapsulants for conventional silicon PV modules: A ray-tracing study,” IEEE Photovoltaic Specialists Conference (PVSC), 2009.

[59] W.-S. Su et al., “Optimization of the output power by effect of backsheet reflectance and spacing between cell strings,” 37th IEEE Photovoltaic Specialists Conference, 2011.

[60] J. Jang, A. Pfreundt, M. Mittag, and K. Lee, “Performance Analysis of Bifacial PV Modules with Transparent Mesh Backsheet,” Energies, vol. 14, no. 5, p. 1399, 2021.

[61] H.P. Yin, Y.F. Zhou, S.L. Sun, W.S. Tang, W. Shan, X.M. Huang, X.D. Shen, “Optical enhanced effects on the electrical performance and energy yield of bifacial PV modules”, Solar Energy, Volume 217, 2021.

[62] R. Witteck, M. Siebert, T. Wietler, M. Köntges, P. Laurikenas and J. Denafas, "Improved STC and energy yield performance of bifacial modules with white-grid rear reflectors," 2022 IEEE 49th Photovoltaics Specialists Conference (PVSC), Philadelphia, PA, USA, 2022.

[63] C. Deline, S. Macalpine, B. Marion, F. Toor, A. Asgharzadeh, and J. S. Stein, “Assessment of Bifacial Photovoltaic Module Power Rating Methodologies-Inside and Out,” IEEE Journal of Photovoltaics, 2017.

[64] S. Obara, N. Ishikawa, and K. Sugibuchi, “Bifacial-PV Power Output Gain in the Field Test Using High Bifaciality Solar Cells,” 28th European Photovoltaic Solar Energy Conference and Exhibition, pp. 4312–4317, 2013.

[65] G. J. M. Janssen, B. B. Van Aken, A. J. Carr, and A. A. Mewe, “Outdoor Performance of Bifacial Modules by Measurements and Modelling,” Energy Procedia, vol. 77, pp. 364–373, 2015.

[66] S. Guo, T. M. Walsh, and M. Peters, “Vertically mounted bifacial photovoltaic modules: A global analysis,” Energy, vol. 61, pp. 447–454, 2013.

[67] Gautam Raina, Sunanda Sinha, "A comprehensive assessment of electrical performance and mismatch losses in bifacial PV module under different front and rear side shading scenarios", Energy Conversion and Management, Volume 261, 2022.

[68] Tian Shen Liang, Pravettoni Mauro, Deline Chris, Stein Joshua, Kopecek Radovan, Singh Jai Prakash, Luo Wei Wang Yan, Aberle Armin, Khoo Yong Sheng. "A review of crystalline silicon bifacial photovoltaic performance characterisation and simulation". Energy and Environmental Science, 2019.

[69] S. Pal, A. Reinders and R. Saive, "Simulation of Bifacial and Monofacial Silicon Solar Cell Short-Circuit Current Density Under Measured Spectro-Angular Solar Irradiance," in IEEE Journal of Photovoltaics, vol. 10, no. 6, pp. 1803-1815, 2020.

[70] S. Pal and R. Saive, "Output Enhancement of Bifacial Solar Modules Under Diffuse and Specular Albedo," 2021 IEEE 48th Photovoltaic Specialists Conference (PVSC), 2021.

[71] K. Ganesan, D. Prince Winston, S. Sugumar, S. Jegan, “Performance analysis of n-type PERT bifacial solar PV module under diverse albedo conditions”, Solar Energy, Volume 252, 2023.

[72] Muthu, V., and Ramadas, G. "A Comprehensive 4E Study on the Performance of Bifacial Solar Module Installed on Different Ground Surface Colors: An Experimental Study on a Specific Site." ASME. J. Sol, 2023.

[73] Durusoy, B., Ozden, T., Akinoglu, B. G. "Solar irradiation on the rear surface of bifacial solar modules: a modeling approach." Scientific Reports, 2020.

[74] Wenbo Gu, Tao Ma, Salman Ahmed, Yijie Zhang, Jinqing Peng, "A comprehensive review and outlook of bifacial photovoltaic (bPV) technology", Energy Conversion and Management, Volume 223, 2020.

[75] Eduardo Lorenzo, "On the historical origins of bifacial PV modelling", Solar Energy, Volume 218, 2021.

[76] Yunkun Tao, Jianbo Bai, Rupendra Kumar Pachauri, Yue Wang, Jian Li, Harouna Kerzika Attaher, "Parameterizing mismatch loss in bifacial photovoltaic modules with global deployment: A comprehensive study", Applied Energy, Volume 303, 2021.

[77] C. F. Abe, J. Batista Dias, G. Notton, G. -A. Faggianelli, G. Pigelet and D. Ouvrard, "Estimation of the Effective Irradiance and Bifacial Gain for PV Arrays Using the Maximum Power Current," in IEEE Journal of Photovoltaics, vol. 13, 2023.

[78] E. M. Ahmed, M. Aly, M. Mostafa, H. Rezk, H. Alnuman, and W. Alhosaini, “An Accurate Model for Bifacial Photovoltaic Panels,” Sustainability, vol. 15, no. 1, p. 509, 2022.

[79] Bo Sun, Lin Lu, Yanping Yuan, Paweł Ocłoń, "Development and validation of a concise and anisotropic irradiance model for bifacial photovoltaic modules", Renewable Energy, Volume 209, 2023.

[80] Marzia Alam, Mehreen Saleem Gul, Tariq Muneer, "Performance analysis and comparison between bifacial and monofacial solar photovoltaic at various ground albedo conditions", Renewable Energy Focus, Volume 44, 2023.

[81] Tihomir Betti, Ivan Bevanda, Ivan Marasović, Ivana Zulim, "A new approach to comparing photovoltaic simulation software", Energy Sources, Part A: Recovery, Utilization, and Environmental Effects, 45:2, 6290-6304, 2023.

[82] S. P. Aly, J. J. John, G. Mathiak, O. Albadwawi, L. Pomares and V. Alberts, "A thermal model for bifacial PV panels," 2022 IEEE 49th Photovoltaics Specialists Conference (PVSC), Philadelphia, PA, USA, 2022.

[83] M. B. Koentopp, M. Schu?tze, D. Buss, and R. Seguin, “Optimized Module Design: A Study of Encapsulation Losses and the Influence of Design Parameters on Module Performance,” IEEE Journal of Photovoltaics, vol. 3, no. 1, pp. 138–142, 2013.

[84] I. M. Peters, Y. S. Khoo, and T. M. Walsh, "Detailed Current Loss Analysis for a PV Module Made With Textured Multicrystalline Silicon Wafer Solar Cells," IEEE Journal of Photovoltaics, vol. 4, no. 2, pp. 585–593, 2014.

[85] Y. S. Khoo, T. M. Walsh, F. Lu, and A. G. Aberle, "Method for quantifying optical parasitic absorptance loss of glass and encapsulant materials of silicon wafer based photovoltaic modules," Solar Energy Materials and Solar Cells, vol. 102, pp. 153–158, 2012.

[86] E. Sng, C. X. Ang, and I. L. H. Lim, "Investigation and Analysis of Bifacial Photovoltaics Modules with Reflective Layer," 35th European Photovoltaic Solar Energy Conference and Exhibition, pp. 1260–1264, 2018.

[87] U. A. Yusufoglu, T. M. Pletzer, L. J. Koduvelikulathu, C. Comparotto, R. Kopecek, and H. Kurz, "Analysis of the Annual Performance of Bifacial Modules and Optimization Methods," IEEE Journal of Photovoltaics, vol. 5, no. 1, pp. 320–328, 2015.

[88] C. Monokroussos, R. Gottschalg, A. N. Tiwari, G. Friesen, D. Chianese, and S. Mau, "The Effects of Solar Cell Capacitance on Calibration Accuracy When using a Flash Simulator," IEEE 4th World Conference on Photovoltaic Energy Conference, 2006.

[89] A. Edler, M. Schlemmer, J. Ranzmeyer, and R. Harney, "Understanding and Overcoming the Influence of Capacitance Effects on the Measurement of High Efficiency Silicon Solar Cells," Energy Procedia, vol. 27, pp. 267–272, 2012.

[90] A. Virtuani, G. Rigamonti, G. Friesen, D. Chianese, and P. Beljean, "Fast and accurate methods for the performance testing of highly-efficient c-Si photovoltaic modules using a 10 ms single-pulse solar simulator and customized voltage profiles," Measurement Science and Technology, vol. 23, no. 11, p. 115604, 2012.

[91] J. O'Rourke Computational Geometry in C 2nd ed. Cambridge: Cambridge University Press, 1998.

[92] Nyeinga Karidewa, Banda Eldad, Nydal Ole. Ray tracer for analysis of solar concentrating systems. 30th ISES Biennial Solar World Congress 2011, 2011.

[93] M. H. Saw, Y. S. Khoo, J. P. Singh, and Y. Wang Enhancing optical performance of bifacial PV modules 7th International Conference on Silicon Photovoltaics, 2017.

[94] K. Wilson, D. Ceuster, and R. Sinton, "Measuring the Effect of Cell Mismatch on Module Output," in 2006 IEEE 4th World Conference on Photovoltaic Energy Conference, 2006.

[95] M. Li, L. Zeng, Y. Chen, L. Zhuang, X. Wang, and H. Shen, "Realization of Colored Multicrystalline Silicon Solar Cells with SiO_2 /SiN_x:H Double Layer Antireflection Coatings," International Journal of Photoenergy, vol. 2013, pp. 1–8, 2013.

[96] A. A. Sabater, N. Wöhrle, J. M. Greulich, S. Rein, and K. Ramspeck, “Impact of bifacial illumination and sorting criteria of bifacial solar cells on module power,” in AIP Conference Proceedings, 2018.

[97] Oliver Kunz, Rhett J. Evans, Mattias K. Juhl, Thorsten Trupke, "Understanding partial shading effects in shingled PV modules", Solar Energy, Volume 202, 2020.

[98] Klasen, Nils and Mondon, Andrew and Kraft, Achim and Eitner, Ulrich, "Shingled Cell Interconnection: A New Generation of Bifacial PV-Modules.", 7th Workshop on Metallization and Interconnection for Crystalline Silicon Solar Cells, 2017.